Phase estimation for Differential Interference Contrast microscopy

Lola Xiomara Bautista Rozo

UNIVERSITY CÔTE D'AZUR

DOCTORAL SCHOOL STIC

SCIENCES ET TECHNOLOGIES DE L'INFORMATION ET DE LA COMMUNICATION

P H D T H E S I S

to obtain the title of

PhD of Science

of the University Côte d'Azur

Specialty : Digital Image and Signal Processing

Defended by

Lola Xiomara BAUTISTA ROZO

Phase Estimation for Differential Interference Contrast Microscopy

Thesis Advisor: Laure Blanc-Féraud

prepared at I3S Laboratory, Morpheme Team

defended on June 30, 2017

Jury :

Reviewers :	Alain Dieterlen	-	Université de Haute-Alsace, Mulhouse
	Christine De Mol	-	Université Libre de Bruxelles
Advisor :	Laure Blanc-Féraud	-	I3S,UCA,CNRS
President :	Vicente Zarzoso	-	I3S,UCA,CNRS
Examinators :	Arturo Plata	-	Universidad Industrial de Santander
	Caroline Chaux	-	Aix-Marseille Université
	Marco Prato	-	University of Modena and Reggio Emilia
Invited :	Audric Drogoul	-	Thales Alenia Space

Preface

This thesis was financially supported by the *Universidad Industrial de Santander* (UIS) from Colombia, as part of the plan of graduated educational development for teaching staff, in order to strengthen the undergraduated and graduated programs of the university, in this case specifically for the School of Computer Engineering and Informatics to which I belong since 2011.

The UIS counts with a unit of technological transfer to fulfill the needs of the region in terms of innovation, research and development. This unit has the laboratory of microscopy, which provides analytical tools for medicine, biology, geology and the oil industry, among others. This laboratory counts with different systems such as scanning electron microscopy, atomic force microscopy, wide-field microscopy, and differential interference contrast (DIC) microscopy, being the later the object of interest for this thesis.

The DIC system at the laboratory is a Carl Zeiss Axio Imager Z1 microscope, which has been mainly used for metrology and characterization of nanoparticles, on which the changes in the topography of the object are in the order of a wavelength. In a previous work done by a master student in Physics at UIS[1], they used a phase shifting interferometry algorithm to retrieve the phase gradients caused by the topography of the object, however, this method is sensitive to noise and requires several image acquisitions.

In order to improve our knowledge on better algorithms for phase reconstruction, this research topic was proposed for the present PhD thesis under the direction of Dr. Laure Blanc-Féraud at the I3S laboratory in Sophia Antipolis, France and advising of Dr. Arturo Plata at UIS in Colombia. As a consequence of this binational collaboration, we obtained the ECOS-Nord grant C15M01 which allowed us bilateral mobility for three years (2015-2017).

In the course of this work, and because of the complexity of the problem, we counted as well with the support of Dr. Luca Zanni, Dr. Marco Prato and PhD student Simone Rebegoldi, from the department of Physics, Computer Science and Mathematics of the University of Modena and Reggio Emilia in Italy, who contributed with efficient numerical methods for accurate phase reconstruction. Products of this collaboration are the following works:

- L. Bautista, L. Blanc-Féraud, S. Rebegoldi, A. Plata. *"Gradient-Based Phase Estimation in Differential Interference Contrast (DIC) Microscopy"*. Assemblée générale "Interférences d'Ondes". Lyon 19-21 Octobre 2015.

[1] C. Chacón and A. Plata. *Reconstrucción tridimiensional por microscopía de contraste diferencial con polarización circular*. Master thesis in Physics. Universidad Industrial de Santander, Bucaramanga, Colombia. 2013. Available at `http://tangara.uis.edu.co/biblioweb/tesis/2013/149493.pdf`

- L. Bautista, L. Blanc-Féraud, S. Rebegoldi, M. Prato, L. Zanni, A. Plata. *"Phase estimation in differential-interference-contrast (DIC) microscopy"*. 2016 IEEE 13th International Symposium on Biomedical Imaging (ISBI). Prague April 2016.
- S. Rebegoldi, L. Bautista, L. Blanc-Féraud, M. Prato, L. Zanni, A. Plata. *"An efficient gradient-based method for differential interference contrast microscopy"* NUMTA 2016, Calabria, Italy, 19-25 June. 2016.
- S. Rebegoldi, L. Bautista, L. Blanc-Féraud, M. Prato, L. Zanni, A. Plata. *"Accelerated gradient-based methods for phase estimation in differential-interference-contrast microscopy"*.SIMAI 2016, Milan, Italy, 13-16 September. 2016.
- S. Rebegoldi, L. Bautista, L. Blanc-Féraud, M. Prato, L. Zanni, A. Plata. *"Optimization methods for phase estimation in differential-interference-contrast (DIC) microscopy"*. Workshop on Optimization Techniques for Inverse Problems III, Modena, Italy, 19-21 September. 2016.
- S. Rebegoldi, L. Bautista, L. Blanc-Féraud, M. Prato, L. Zanni, A. Plata. *"A comparison of edge-preserving approaches for differential interference contrast microscopy"*, accepted to the Inverse Problems Journal (article reference IP-101183.R3).

I am grateful to Dr. Laure Blanc-Féraud for her admirable dedication and guidance. To Dr. Arturo Plata for his availability in the understanding of the physical model and experimentation on the microscope. To the italian team for their hard work. I also would like to thank all the members of Morpheme Team, Xavier, Grégoire, Eric, Jane, Agus, Emma, Marine and Anca for their continuous support and for allowing me to share this process with them. To my family who encouraged me at every moment in spite of the distance. To my colleagues Carlos Jaime, Gabriel, Elberto and Ceci at UIS for their unconditional help.

This experience is rich in the quality of people I had the opportunity to meet along this 3 years and a half. Retaking contact with my special friends Karla, Xiomara, Samuel, Hernán and Marthica, as well as their families in Spain showed me the strength of our ties. Michel, Patricia, Carlos, Margarita, Jacobo, Diego, Claudia, Helena, Emilia, Alejandro and Veronika, Melissa and Miguel who were the extension of my family in Nice. My roomates James, Sebastian, Martina, Bertha, Pauline and Beata. Froso, Alexis, Manu, Cédric (also known as Arnaud) and Yasmine for sharing many adventures and good moments that will be always in our memories. Gaëlou, thanks for your patience, good humor, originality, friendship and love.

What follows on this document is the result of a great professional and personal challenge which I'm proud of. Hope you enjoy the reading and looking forward to comments and feedback.

Nice, 2017-06-09
Lola Bautista

Abstract

In this dissertation we address the problem of estimating the phase from color images acquired with differential–interference–contrast (DIC) microscopy. This technique has been widely recognized for producing high contrast images at high lateral resolution. One of its disadvantages is that the observed images cannot be easily used for topographical and morphological interpretation, because the changes in phase of the light, produced by variations in the refractive index of the object, are hidden in the intensity image. We present an image formation model for polychromatic light, along with a detailed description of the point spread function (PSF). As for the phase recovery problem, we followed the inverse problem approach by means of minimizing a non-linear least–squares (LS)–like discrepancy term with an edge–preserving regularizing term, given by either the hypersurface (HS) potential or the total variation (TV) one. We investigate the analytical properties of the resulting objective non-convex functions, prove the existence of minimizers and propose a compact formulation of the gradient allowing fast computations. Then we use recent effective optimization tools able to obtain in both the smooth and the non-smooth cases accurate reconstructions with a reduced computational demand. We performed different numerical tests on synthetic realistic images and we compared the proposed methods with both the original conjugate gradient method proposed in the literature, exploiting a gradient–free linesearch for the computation of the steplength parameter, and other standard conjugate gradient approaches. The results we obtained in this approach show that the performances of the limited memory gradient method used for minimizing the LS+HS functional are much better than those of the CG approaches in terms of number of function/gradient evaluations and, therefore, computational time. Then we also consider another formulation of the phase retrieval problem by means of minimization with respect to a complex variable under constraint of modulus one. However, standard projected gradient descent algorithms appear to be inefficient and sensitive to initialization. We conclude by proposing in this case a reformulation by optimization on low-rank matrices.

Keywords: DIC microscopy, phase estimation, nonlinear optimization methods

Résumé

Dans cette thèse, nous nous intéressons à la microscopie DIC (Differential interference contrast) en couleur. L'imagerie DIC est reconnue pour produire des images à haut contraste et à haute résolution latérale. L'un de ses inconvénients est que les images observées ne peuvent pas être utilisées directement pour l'interprétation topographique et morphologique, car les changements de phase de la lumière, produits par les variations de l'indice de réfraction de l'objet, sont cachés dans l'image d'intensité. Il s'agit donc d'un problème de reconstruction de phase. Nous présentons un modèle de formation d'image pour la lumière polychromatique, et décrivons de manière détaillée la réponse impulsionnelle du système. Le problème de la reconstruction de phase est abordé sous l'angle d'un problème inverse par minimisation d'un terme d'erreur des moindres carrés (LS) non linéaire avec un terme de régularisation préservant les discontinuités, soit par le potentiel hypersurface (HS), soit par la variation totale (TV). Nous étudions les propriétés des fonctions objectives non convexes résultantes, prouvons l'existence de minimisateurs et proposons une formulation compacte du gradient permettant un calcul rapide. Ensuite, nous proposons des outils d'optimisation efficaces récents permettant d'obtenir à la fois des reconstructions précises pour les deux régularisations lisse (HS) et non lisse (TV) et des temps de calculs réduits. Nous avons effectué différents tests numériques sur des images réalistes et nous avons comparé les méthodes proposées à la méthode de gradient conjugué originalement proposée dans la littérature DIC, exploitant une recherche linéaire sans gradient pour le calcul du pas de descente, ainsi qu'à d'autres approches standards de gradient conjugué. Les résultats que nous avons obtenus dans cette approche montrent que la méthode proposée pour la minimisation de la fonctionnalité LS + HS est plus performante que celles des approches CG en termes de nombre d'évaluations de la fonction et de son gradient et, par conséquent, en termes de temps de calcul. Ensuite, nous considérons une autre formulation du problème de reconstruction de phase par minimisation par rapport à une variable complexe avec une contrainte de module un. Cependant, les algorithmes standard de minimisation avec projection semblent être peu efficaces et sensibles à l'initialisation. Nous terminons en proposant dans ce cas une refomulation par optimisation sur des matrices de rang faibles.

Mots clés: Microscopie DIC, estimation de phase, méthodes d'optimization non-linéaires

Contents

List of Figures

List of Tables

List of Symbols and Acronyms

Symbols

λ	illumination wavelength
$\overrightarrow{\mathbf{E}}$	electric vector
$\overrightarrow{\mathbf{B}}$	magnetic vector
n_o	refractive index for Ordinary ray
n_e	refractive index for Extraordinary ray
$2\Delta x$	shear distance between Ordinary and Extraordinary ray in the Nomarski prism
$2\Delta\theta$	bias retardation. Shift in the phase of Ordinary and Extraordinary ray by translation of the Nomarski prism
τ	shear angle with respect to the horizontal axis of the microscope
χ	spatial indexing set
MP	size of the discrete image with M rows and P columns
λ_ℓ	illumination wavelength for $\ell = 1, 2, 3$, the index of one of the three RGB channels
$o_{k,\lambda_\ell} \in \mathbb{R}^{MP}$	the $\ell-$th color component of the $k-$th discrete observed image at shear angle τ_k
$\phi \in \mathbb{R}^{MP}$	the unknown phase vector
$h_{k,\lambda_\ell} \in \mathbb{C}^{MP}$	the $\ell-$th color component of the discrete DIC point spread function (PSF) at shear angle τ_k
$p_{\lambda_\ell} \in \mathbb{R}^{MP}$	the coherent PSF of the microscope's objective lens for the wavelength λ_ℓ
$P_{\lambda_\ell} \in \mathbb{C}^{MP}$	disk support function of amplitude 1 in Fourier domain
$\eta_{k,\lambda_\ell} \in \mathbb{R}^{MP}$	Gaussian random noise
f_c	cutoff frecuency
f_s	sampling Nyquist frecuency
R_k	rotation matrix according to shear angle τ_k
$h_1 \otimes h_2$	2D convolution between images h_1, h_2
$h_1 . * h_2$	component-wise product between the two images h_1, h_2
$(\tilde{h})_j = (h)_{-j}$	matrix transpose by columns and rows
$Tr(A)$	trace of matrix A
∇f	gradient of function f
$\nabla^2 f$	Hessian of function f
$z = z_r + iz_i$	complex number with real component z_r and imaginary component z_i
$\bar{z}$	complex conjugate of z
z^*	complex conjugate transpose
$\frac{\partial_W f(z)}{\partial z}, \frac{\partial_W f(z)}{\partial \bar{z}}$	Wirtinger derivatives
$\check{\phi} \in \mathbb{R}^{MP}$	true phase function
$\hat{\phi} \in \mathbb{R}^{MP}$	estimated phase function
$\check{u} \in \mathbb{C}^{MP}$	true specimen function
$\hat{u} \in \mathbb{C}^{MP}$	estimated specimen function

Acronyms

BB	Barzilai-Borwein rules
CG	Conjugate Gradient
DIC	Differential Interference Contrast
EM	ElectroMagnetic wave
FFT	Fast Fourier Transform
FR	Fletcher-Reeves
FR-PA	Fletcher-Reeves with Polynomial Approximation
FR-PR	Polak-Ribière constrained by Fletcher-Reeves values
HS	Hypersurface potential
IFFT	Inverse Fast Fourier Transform
ILA	Inexact Linesearch Algorithm
KL	Kurdyka–Łojasiewicz property
LMSD	Limited Memory Steepest Descent
NA	Numerical Aperture of objective lens
PR	Polak-Ribière
PR^+	Polak-Ribière with nonnegative values
PR-PA	Polak-Ribière with Polynomial Approximation
PSF	Point Spread Function
SNR	Signal–to–Noise Ratio
SW	Strong Wolfe conditions
TV	Total Variation
VMILA	Variable Metric Inexact Linesearch Algorithm

Chapter 1

Introduction

The area of microscopy imaging has gained great relevance since the invention of the microscope, as a tool for studying the microscopic and nanoscopic world. Medicine, biology and live-cell imaging benefit from the many imaging techniques that provide different types of information from the same scene. Among the most popular techniques are dark-field, bright-field, polarizing, confocal, fluorescence, phase contrast and differential interference contrast (DIC) microscopy. Confocal and fluorescence microscopy are among the most used for real time live-cell imaging, but that does not mean that the others are not useful at all.

The observation of biological structures is a challenging task, especially in live-cell imaging. In fact, optical microscopes are limited by the diffraction of light, and imaging is affected by the optical properties of the object, such as spatial variations in refractive index which introduce aberrations as the light traverses the object [18]. Consequently, since most of the cell components are transparent to visible light [38] and because of the high content of water, traditional light microscopy may suffer from a lack of contrast, reason why staining is often used to produce contrast by light absorption [80]. Unfortunately, such a process can deteriorate the living cells. An alternative solution consists in reducing the condenser numerical aperture, which however worsens dramatically the resolution of the image.

1.1 Motivation

The technique of our interest is DIC microscopy, designed by Allen, David and Nomarski [4] to overcome the inability to image unstained transparent biological specimens, which is typical of bright–field microscopes, while avoiding at the same time the halo artifacts of other techniques designed for the same purpose, such as phase contrast. DIC microscopes are able to provide contrast to images by exploiting the phase shifts in light induced by the transparent specimens (also called phase objects) while passing through them. This phenomenon is not detected by the human eye, neither by an automatic visual system, and occurs because of the interaction of light with different refractive indexes of both the specimen and its surrounding medium. In DIC microscopy, such phase shifts are converted into artificial black and white shadows in the image, which correspond to changes in the spatial gradient of the specimen's optical path length. Furthermore, this technique has been widely recognized for its possibility to use full numerical apertures in the objective, which results in high contrast images at high lateral resolution of approximately 240 nm in the range of visible light (400–700 nm) and around 30 nm in the range of x-ray radiation (0.01–10 nm) [12]. One disadvantage of DIC microscopy is that the observed images cannot be easily used for topographical and morphological

interpretation, because the changes in phase of the light are hidden in the intensity image. It is then of vital importance to recover the specimen's phase function from the observed DIC images.

The problem of phase estimation in optical imaging has been widely studied, as shown in the review made in [78]. Previous work for reconstructing the DIC phase function has been done by Munster et al [64], who retrieve the phase information by deconvolution with a Wiener filter; line integration of DIC images is proposed by Kam in [48], supposing that the line integration along the shear angle yields a positive definite image, which is not always the case since the intensity image is a nonlinear relation between the transmission function of the specimen and the point spread function of the microscope. Kou et al [52] introduced the use of transport of intensity equation to retrieve the phase function; Bostan et al [19] also used this approach, including a total variation regularization term to preserve the phase transitions. Finally, in the work of Preza [74, 75, 72, 73], the phase estimation in DIC microscopy has been addressed by considering the minimization of a Tikhonov regularized discrepancy term, which is performed by means of a modified nonlinear conjugate gradient (CG) method.

1.2 Goal

The goal of the work included in this dissertation is to provide efficient methods for the nonlinear, non-convex inverse problem of phase estimation in Differential Interference Contrast (DIC) microscopy. To accomplish this we have chosen to solve the minimization of a functional formed by a least-squares discrepancy term and a regularization term, by the following two approaches:

- *Unconstrained approximation*, on which we consider two different regularization terms, the first one being the total variation (TV) functional which is suitable for piecewise constant images, while the second is the hypersurface (HS) potential [25], which is a smooth generalization of the TV able to reconstruct both sharp and smooth variations of the unknown phase. Since the latter choice leads to the minimization of a smooth functional, we consider a limited memory gradient method, in which suitable adaptive steplength parameters are chosen to improve the convergence rate of the algorithm. As concerns the TV–based model, we address the minimization problem by means of a recently proposed linesearch–based forward–backward method able to handle the nonsmoothness of the TV functional [17].
- *Constrained approximation*, on which we do a change of variable into the complex set $\mathbb{C}$, and introducing a constraint of variables of module 1 by means of a projection operator. We implemented two algorithms, one based on Gradient Descent with projection and another one using Conjugate Gradient with projection. We implemented the computation of the gradient using Wirtinger derivatives [21].

1.3 Contributions

The major contributions in this dissertation are:

1. Extension of the original imaging formation model to polychromatic light, under partially coherent illumination.

2. A novel compact formulation of the gradient allowing fast computation in the Fourier domain for the phase estimation functional.

3. A phase retrieval method by minimizing a discrepancy term with Total Variation (smoothed and nonsmoothed) regularization term, along with a study of the functional regarding to the existence of minimizers.

4. Implementation and evaluation of minimization algorithms with phantom objects and synthetic realistic images, and comparison with state–of–the–art gradient methods, as well as a phase retrieval method by minimizing a functional depending on complex variable with modulus constraint.

1.4 Organization of the dissertation

The organization of this dissertation is as follows. In Chapter 2 we start with a brief review of physical-optical concepts related to the nature of light and the elements of the microscope, necessary to understand the way the DIC system works for transmitted coherent light. It also includes a literature review of previous imaging models for DIC microscopy. It is also described the polychromatic image formation model and a detailed analysis of the DIC point spread function under this model.

Chapter 3 is devoted to the unconstrained approximation of the DIC phase estimation problem. It contains a literature review of related work on phase estimation; the statement and corresponding proofs of the analytical properties of the nonlinear inverse problem, such as the existence of minimum points; the iterative optimization algorithms designed to address the phase reconstruction problem, as well as the numerical simulations on synthetic images are presented in order to evaluate efficiency and robustness of the considered approaches.

The constrained approximation approach is presented in Chapter 4, in which is described the reformulation of the inverse problem in terms of the complex variable, and the use of the Wirtinger derivatives to that end. It also includes the numerical tests on synthetic data for comparing the performance with the unconstrained approach.

Finally, general conclusions and perspectives of future work are presented in Chapter 5.

Chapter 2

Differential Interference Contrast (DIC) Microscopy

Since their invention, microscopes have been a powerful tool in different disciplines such as biology, medicine and the study of materials. In medicine, the acquisition of images of microorganisms has given birth to new subjects as bacteriology, immunology, virology, cell pathology, and others [26]. On those cases as well as in biology and live-cell imaging, the emergent challenge is the observation of cell components which are transparent to visible light [38]. Cells have high content of water and show low contrast, reason for which dyes are used to stain different cell structures to produce contrast as the visible light absorbs the dye [80]. In other cases, like in fluorescence microscopy, fluorochrome stains are used to label specific tissue components. This produces fluorescing areas to shine brightly against a dark background with sufficient contrast to permit detection[1]. However, this procedures can damage the cells and specimen can be lost. Microscopists then, choose to use light microscopes with special optical configurations that avoid the fixing or freezing of the cells [46]. Microscopy is also a category of characterization techniques in materials science to analyze the surface and subsurface structure of a material [20].

Another challenge faced by optical microscopy is the limitation by diffraction of light, which directly affects the spatial resolution to properly observe and image the specimen. The quality of resolution is determined by the objective numerical aperture and by the wavelength of light used to illuminate the specimen.

One of the most used techniques for imaging transparent unstained biological specimens is Differential Interference Contrast (DIC) microscopy. This technique appeared in the decade of 1950s as an alternative to overcome the limitation of bright-field microscopes to image this type of specimens, and to obtain images free of the halo artifact introduced by phase contrast microscopes. DIC has been widely recognized by its possibility to use full numerical apertures in the objective, which results in high contrast images at high lateral resolution of approximately 240 nm[2]. However, one disadvantage is that the observed images cannot be easily used for topographical and morphological interpretation.

The purpose of this chapter is to introduce the reader to optical principles such as polarization, birefringence and interference, as well as acquisition details and optical configuration

[1] Abramowitz M. and Davidson M. *"Introduction to Fluorescence"*.`http://www.olympusmicro.com/primer/lightandcolor/fluorointroduction.html`

[2] Using Rayleigh criterion where resolving power is given by $R = 0.61\lambda/\text{NA}$, if $\lambda = 550$ nm and NA=1.4, then $R = 240$ nm. Specifications of this type of objective lens are found in `https://www.micro-shop.zeiss.com/?p=us&f=o&a=v&m=s&id=440762-9904-000`

used by DIC microscopy. For the reader interested only in the image formation model can go directly to section 2.3.

2.1 Optical microscopy

To present the functional principles of DIC microscopes it is important to mention first that, according to their observation method, they belong to the family of optical (light) microscopes (Figure 2.1), and depending on their lighting method they can be of two types: transmission (the light passes through transparent objects) and reflection (the light source illuminates non-transparent objects, and the reflected light is collected by the objective lens) [26].

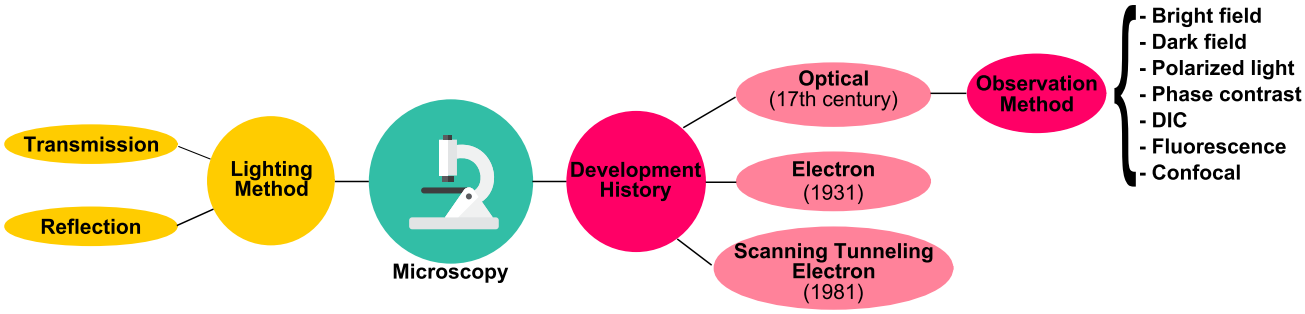

Figure 2.1: Types of microscopes

A light microscope is an optical instrument that uses visible light to produce a magnified image of an object (or specimen) that is projected onto the retina of the eye or onto an imaging device. The two main components in forming the image are: the **objective lens**, which collects light diffracted by the specimen and forms a magnified real image at the real intermediate image plane near the eyepieces or oculars, and the **condenser lens**, which focuses light from the illuminator onto a small area of the specimen [65].

Optical microscopes are limited by the diffraction of light[3], and imaging is affected by the optical properties of the object, such as spatial variations in refractive index which introduces aberrations as the light traverses the object [18]. If light passes through an object but does not become absorbed or diffracted, it remains invisible. Diffraction also limits the optical resolution of the microscope as it is explained in more detail in section 2.3. Table 2.1 shows a brief comparison of the advantages and disadvantages of different optical microscopy techniques according to the interaction of light with the observed specimen. Because of this interaction, objects (specimens) in optical microscopy can be divided into two groups: amplitude objects and phase objects. *Amplitude objects* produce amplitude differences in the image that are detected by the eye as differences in the intensity. *Phase objects* cause a phase shift (advanced or retarded) in the rays of light passing through them [65]. In Figure 2.2 there is an example of the change of behavior of light waves passing through an amplitude (stained) specimen and a phase (unstained) specimen.

[3] ***Diffraction.*** It refers to the spreading of light that occurs when a beam of light interacts with an object.

Technique	Application	Pros	Cons
Brigth field	Viewing live or stained cells	Simple setup with very little preparation required	Biological samples are often low contrast with little natural pigmentation, so samples usually need to be stained. Staining may destroy or introduce artifacts
Dark field	Viewing live, unstained samples	Simple setup. Provides contrast to unstained tissues so living cells can be observed	The tissue needs to be strongly illuminated, which may damage delicate samples
Phase contrast	Most useful for observing transparent, unstained, live cells	Superior to bright-field optics. Fine details which are invisible under bright-field optics show up in high contrast	Not ideal for thick samples that may appear distorted Halo effects or 'phase artifacts' may be present distorting details around the perimeter of the sample
DIC	Similar to phase contrast, it provides contrast to transparent, unstained live cells	Free of the artifacts sometimes seen with phase-contrast Produces quasi-3D images	Not suitable for thick samples
Fluorescence	Used to visualize the location or pattern of fluorescence in cells or tissues that have been stained with fluorescent molecules	Has numerous applications, including: Biological molecules can be fluorescently stained. Immunofluorescence. Cells can be genetically modified so that a protein of interest carries a fluorescent reporter molecule. The location of a protein can then be traced via the fluorescent signal in a living organism	The fluorescence is not permanent. As the samples are viewed photobleaching occurs and the fluorescence fades. Antibody-labeled samples need to be chemically fixed and often the cells also need treatment with detergents to permeabilize cell membranes. Both procedures can introduce artifacts

Table 2.1: Comparison of optical microscopy techniques (taken from [85] `http://www.nature.com/nprot/journal/v7/n9/fig_tab/nprot.2012.096_T1.html`)

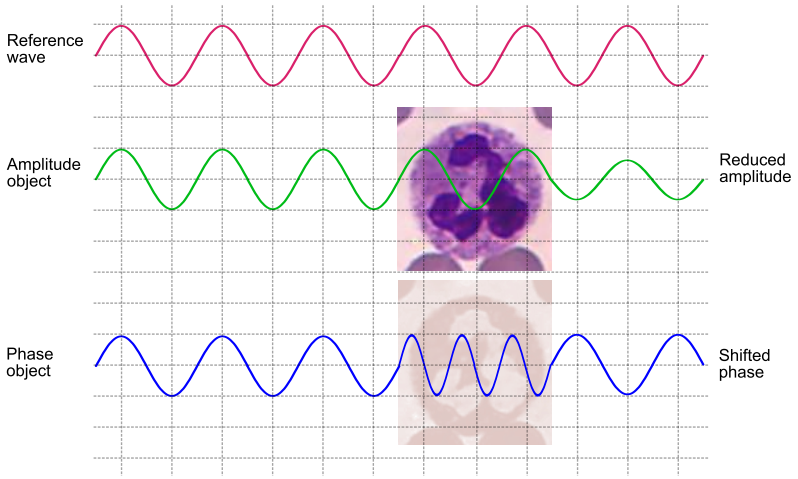

Figure 2.2: Amplitude and phase objects. Middle: amplitude object. Bottom: phase object.

In addition to the specimen characteristics, it is also considered the type of medium through which light propagates. It can be of three types: **transparent** if it readily transmits light, **translucent** if it transmits part of light and scatters most of it, and **opaque** if not transmit it at all. When light travels through any medium its velocity reduces. This dependence of light on the medium is characterized by the **refractive index** of the optical medium[4], defined as

$$n = \frac{\text{velocity of ligth in vacuum}}{\text{velocity of light in the medium}} = \frac{c}{v}$$

From this definition we can say that an optical medium is **homogeneous** if its refractive index does not vary from point to point or **unhomogeneous** if it varies. This medium is also said to be **isotropic** if it exhibits the same values of physical properties in all directions (like glass, water, air), and if not, it is **anisotropic** (like calcite and quartz) [6].

Related to these phenomena is the capability of the objective lens to collect more light and to produce brighter images [69]. For this, the cone of rays diffracted by the specimen should be as large as possible. Such angular aperture is defined in terms of the **numerical aperture (NA)** as

$$\text{NA} = n\ \sin\alpha$$

where n is the refractive index of the medium between the lens and the specimen, and α is the half angle of the cone of specimen light accepted by the objective lens (see Figure 2.3). This also applies for the condenser lens.

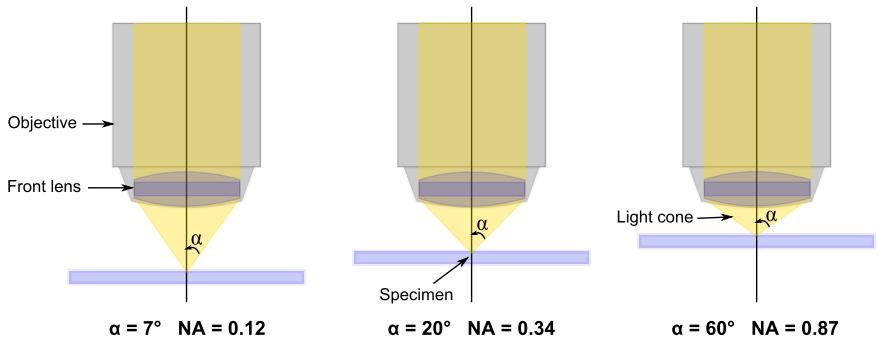

Figure 2.3: Objective lens numerical aperture for $n = 1$ (air)

The numerical apertures of both objective and condenser are related to the effective spatial resolution given by the microscope. As it is explained by Murphy [65], in Figure 2.4 can be seen the role of the condenser diaphragm in determining the effective numerical aperture. Closing the front aperture diaphragm of the condenser from position b to a limits the angle α of the illumination cone reaching the objective, and thus the effective numerical aperture.

[4] $c = 3 \times 10^8$ m/s in vacuum

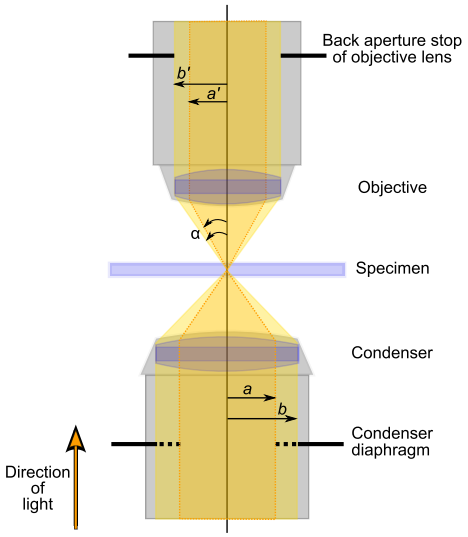

Figure 2.4: Objective and condenser numerical aperture (taken from [65])

Having recalled some of the basic principles of optical microscopy, now we describe the wave nature of light, which is the fundamental concept to explain how polarized light is generated, as well as the property of birefringence of some optical materials. After this we will revisit the phenomenon of interference[5].

2.1.1 The wave nature of light

A **wave** is any repeating and periodic disturbance which propagates energy through a medium. The propagation can be harmonic, which means that the particles in the medium will be in different states of oscillation at different times. Therefore, the displacement of a particle in the medium is a function of space coordinates and time, denoted as $\boldsymbol{y = f(x,t)}$, where y is the displacement.

Consider the displacement as a function of time, at a fixed position $x = 0$. Since the oscillations are sinusoidal, this can be denoted as

$$y = A\ \sin(\omega t + \varphi) = A\ \sin(2\pi\nu t + \varphi) \tag{2.1}$$

where A is the amplitude or maximum displacement of a waveform, ω is the angular frequency measured in radians per unit time and ν is the ordinary frequency measured in Hertz, such that $\nu = \frac{\omega}{2\pi}$ or $\nu = \frac{1}{T}$, where T is the period of the oscillation. The angle $(\omega t + \varphi)$ is called the *phase* of the oscillation; φ indicates a shift in the phase at any given time. Phase represents the state of the oscillation of the particles in the medium by specifying the position and direction of the motion. It is useful when comparing the motion of two particles.

Each time the source of disturbance vibrates once, the wave moves forward a distance λ (known as wavelength). If there are ν vibrations in one second, the wave moves forward a

[5]The review of concepts for section 2.1.1 was based on the textbook of Avadhanulu and Kshirsagar [6]

distance of $\nu\lambda$. Then, the velocity of the wave is denoted as $\upsilon = \nu\lambda$. If the wave travels with velocity υ, after time t, the wave has moved $x = \upsilon t$. The displacement at x is calculated as

$$y = f(x - \upsilon t) \tag{2.2}$$

since $\upsilon = \nu\lambda$, and $\upsilon = \frac{x}{t}$, therefore, $\nu = \frac{x}{\lambda t}$. Using this relation, equation 2.1 is rewritten as

$$y = A \sin\left(2\pi\frac{x}{\lambda} + \varphi\right) \tag{2.3}$$

and this describes the displacement in terms of space.

Using equations 2.1 and 2.3, we can describe the displacement of any point on a harmonic wave in both terms of space and time as

$$y = A \sin\left[\frac{2\pi}{\lambda}(x - \upsilon t) + \varphi\right] \tag{2.4}$$

which can be rewritten as

$$y = A \sin(kx - \omega t + \varphi) \tag{2.5}$$

where $k = \frac{2\pi}{\lambda}$, known as the *propagation constant* or *wave number*. Equation 2.5 can be made independent of the coordinate system by converting it into vector form. Let vector $\mathbf{k}$ have a magnitude equal to the wave number k, and a direction parallel to the positive direction of x-axis. We can replace x by any arbitrary direction r and write

$$y = A \sin(\mathbf{k} \cdot \mathbf{r} - \omega t + \varphi) \tag{2.6}$$

Before proceeding to describe the phenomena of polarization and interference, it is important to define the **coherence of light**, when the phase of a wave field varies identically in time and in space, that is, there exist two types of coherence:

- **Spatial coherence:** when phase varies in identical fashion at two points in space.
- **Temporal coherence:** when phase varies in identical fashion at two points in time.

Laser light is an example of totally coherent light, while white light is an example of incoherent light. However, since coherence is required for producing diffraction and interference, incoherent light sources (like incandescent filament lamps) are *partially coherent*; this is because *"the wave bundle comprising each minute ray emanating from a point on the filament vibrate in phase with each other"* [65].

There exist a classification of waves related to the source that generates them, in which appear the **electromagnetic (EM) waves**, such as visible light, radio waves and x-rays. EM waves consist of electric ($\overrightarrow{\mathbf{E}}$) and magnetic ($\overrightarrow{\mathbf{B}}$) fields (see Figure 2.5) which oscillate in mutually perpendicular planes, also perpendicular to the direction of propagation, and do not require material medium for their propagation. They all travel in free space with the same speed c.

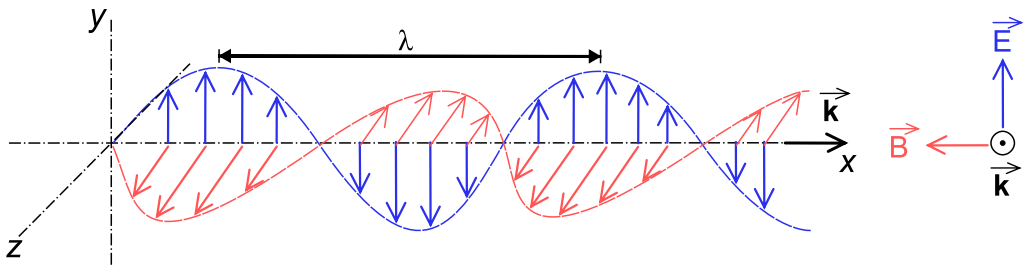

Figure 2.5: Electromagnetic wave

In optics convention, EM waves are described in terms of the electric vector variations in space [77], as seen in the top part of Figure 2.6. Recalling equation 2.6, the wave equation for light can be written as

$$E_y = E_0 \sin(kx - \omega t + \varphi) \tag{2.7}$$

this equation has a constant amplitude E_0, therefore is called a *planar wave*, which means that the field vector $\vec{\mathbf{E}}$ lies confined in a plane at each point in space, and the planes at any two different points are parallel to each other, as shown at the bottom part of Figure 2.6. From this we observe that light waves vibrate in a preferential direction normal to the wave propagation. This preference of direction leads to the phenomenon called **polarization**.

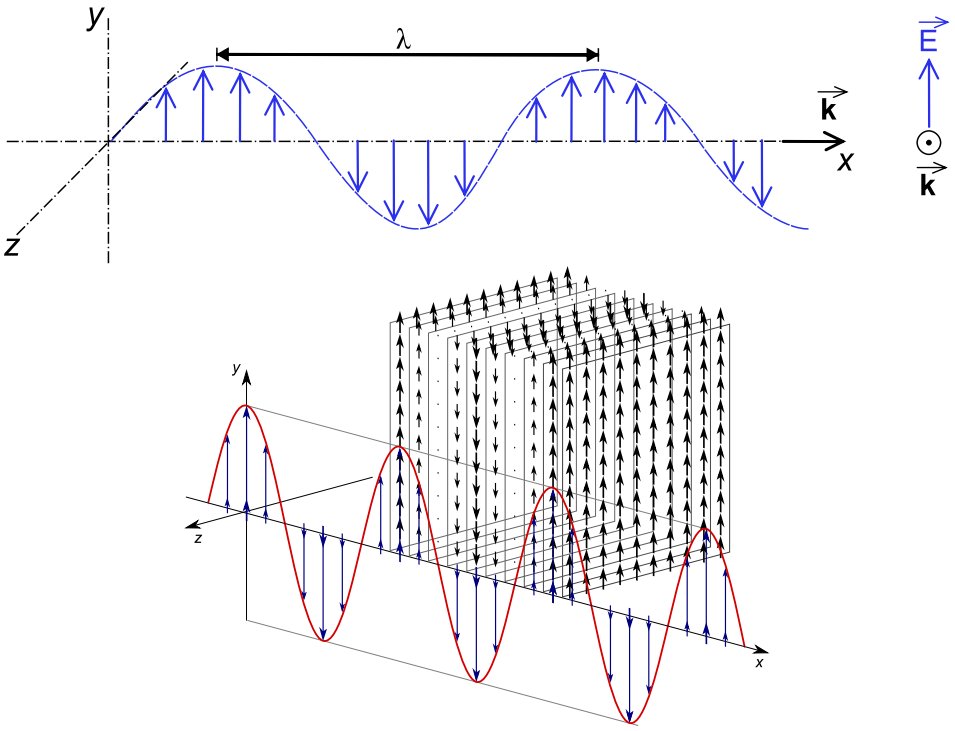

Figure 2.6: Electric vector of light and planar wave[6]

[6] Modified from `https://en.wikipedia.org/wiki/Polarizer#Circular_polarizers`

Polarization

The polarization[7] of an EM wave refers to the orientation of its electric field vector $\overrightarrow{\mathbf{E}}$. The direction of oscillation of the electric field vector in an ordinary light beam occurs in all the possible planes perpendicular to the beam direction. A light wave in which $\overrightarrow{\mathbf{E}}$-vector oscillates in more than one plane, is referred to as **unpolarized light**, while **polarized light** is the light that contains waves that only fluctuates in one specific plane.

We can distinguish three types of polarization:

i) **Plane polarized light.** The oscillations of the $\overrightarrow{\mathbf{E}}$ vector occur in a single plane perpendicular to the direction of propagation. As the direction of the field vector at some point in space and time lies along a line in a plane perpendicular to the direction of wave propagation, a plane-polarized light is also known as a **linearly-polarized** wave.

With linear polarization, the orientation of the $\overrightarrow{\mathbf{E}}$-vector stays constant at a point in space, that is, the direction of $\overrightarrow{\mathbf{E}}$ does not vary with time, but its magnitude varies sinusoidally with time. If the field is either pointing up or down, it is called **vertical polarization**, and if it is pointing either left or right, it is called **horizontal polarization**. Electric fields are not restricted to pointing exactly along vertical or horizontal axes, but can be at any arbitrary angle to those axes. This can be regarded as a linear combination of horizontally and vertically polarized light, with appropriate amplitude, and which are oscillating in phase, or 180° out of phase (see Figure 2.7).

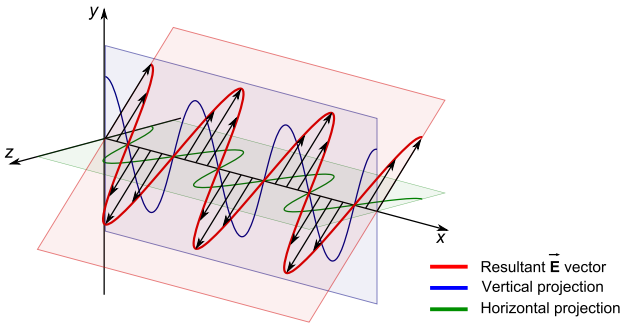

Figure 2.7: Linearly polarized light[6]

ii) **Circularly polarized light.** It is due to the superposition of two coherent linearly polarized waves of *equal* amplitude, oscillating in mutually perpendicular planes, and are out of phase by 90°. If we stand at one point in space, and look at the direction of the wave, we observe that the $\overrightarrow{\mathbf{E}}$-vector sweeps a circle in space, and the oscillations of the resultant $\overrightarrow{\mathbf{E}}$-vector do not take place in a single plane (see Figure 2.8).

iii) **Ellipticaly polarized light.** It is due to the superposition of two coherent linearly polarized waves of *different* amplitude, oscillating in mutually perpendicular planes, and

[7]For a deep study on the polarization ellipse, please refer to [42], Chapter 4,pages 48-59.

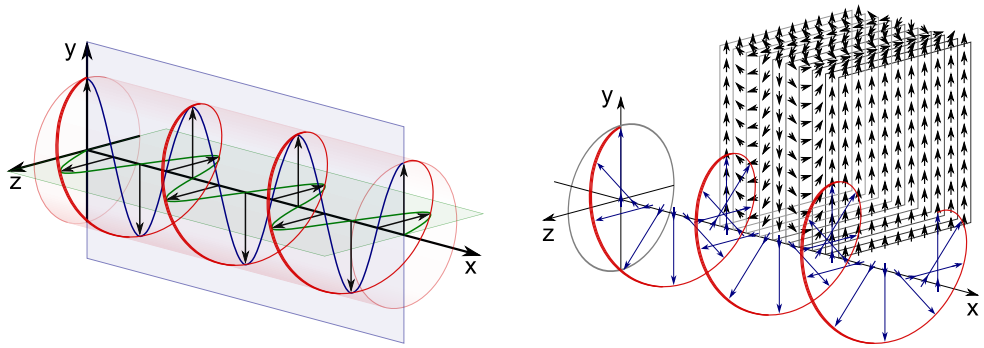

Figure 2.8: Circularly polarized light[6]

are out of phase by an arbitrary angle $\Delta\phi$. The magnitude of the resultant E-vector varies at each point in space and the overall rotation has the appearance of a flattened helix. Figure 2.9 is an overview of the three types of light polarization.

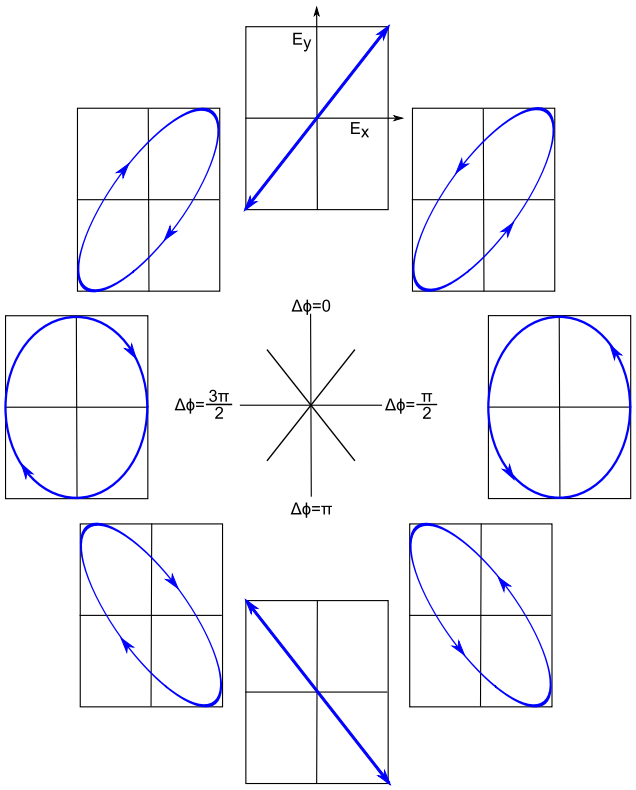

Figure 2.9: Types of polarized light

A special optical filter—called either a polarizer or an analyzer depending on how it's used—transmits only the light wave vibrations of the $\vec{\mathbf{E}}$ vector that are lined up with the filter's transmission axis. The combined action of a polarizer and an analyzer are shown in Figure 2.10. Unpolarized light, represented by the multiple arrows, is incident on a polarizer whose transmission axis (TA) is vertical. As a result, only vertically polarized light emerges from the polarizer. The vertically polarized light is then incident on an analyzer whose transmission axis is horizontal, at 90° to the direction of the vertically polarized light. As a result, no light is transmitted [70].

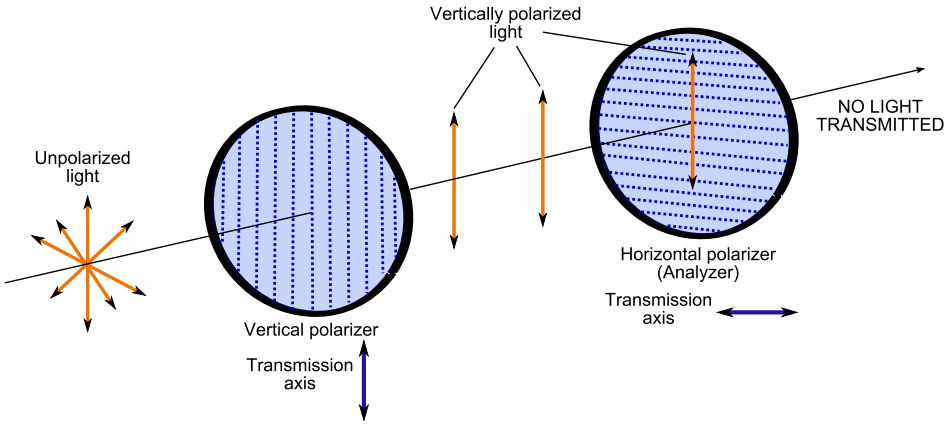

Figure 2.10: Polarizer and Analyzer with crossed transmission axes

Birefringence

Many samples are *optically anisotropic*, that is the refractive index, and hence the wavelength of light in the material, are a function of the direction of propagation. This property is known as double refraction or birefringence. Transparent crystals and minerals such as quartz, calcite rutile, tourmaline, as well as biological materials as collagen, muscle fibers, keratin, amino acids and others are birefringent [20]. Here we are going to describe the optical characteristics of calcite (Figure 2.11). It is bounded by six faces, each of which is a parallelogram with angles equal to 102° and 78°. It has only two corners (A and G) where all the face angles are obtuse (102°). These two corners appear as the unsharpened corners of the crystal (Figure 2.11(a)).

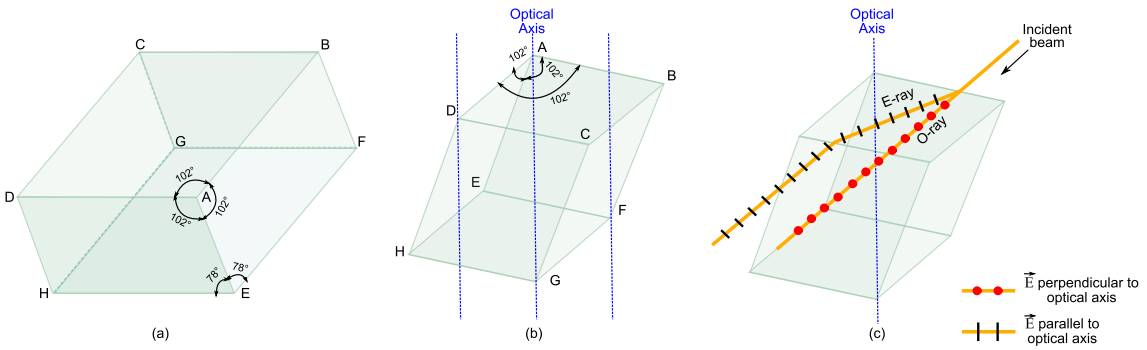

Figure 2.11: Geometry and optical characteristics of calcite

Its **optical axis**[8] is the line bisecting any one of the unsharpened corners (A or G) and making equal angles with each of the three angles meeting there. Any line parallel to this line is also an optic axis (Figure 2.11(b)). It is actually the axis of symmetry of the crystal. A ray of light propagating along this line does not suffer double refraction and neither will all parallel rays. If the light beam is not parallel to the optic axis, then the beam is split into two rays (the Ordinary and Extraordinary) when passing through the crystal (Figure 2.11(c)). The O-ray and E-ray are linearly polarized in mutually perpendicular planes. The $\overrightarrow{\mathbf{E}}$ vector

[8]The optical axis is an imaginary line that defines the path along which light propagates through the system. For a system composed of simple lenses and mirrors, the axis passes through the center of curvature of each surface, and coincides with the axis of rotational symmetry [68].

of E-ray vibrates *parallel* to the optical axis whereas the vibrations of the $\overrightarrow{\mathbf{E}}$ vector of O-ray are *perpendicular* to the optical axis. As the opposite faces of the crystal are parallel, the rays emerge out parallel to the incident ray.

The O-ray travels through the crystal without deviation while the E-ray is refracted at some angle. This means that the velocity of propagation of O-ray is the same in all directions, while that of e-ray changes with direction. Therefore, the refractive index corresponding to O-ray is a constant and is designed by n_o, while the one of E-ray varies and is designed by n_e. If $n_e > n_o$, the birefringence is said to be positive (like in quartz). Conversely, if $n_e < n_o$, the birefringence is said to be negative (like in calcite) [83].

The are three scenarios of the behavior of incident light on an anisotropic crystal [65]:

1. When light is incident at *an angle* to the optical axis, it splits into O- and E-rays, which travel in *different directions* with *different velocities*.
2. When light is incident at a direction *perpendicular* to the optical axis, O- and E-ray propagate in the *same direction* but with *different velocities*.
3. When light is incident at a direction *parallel* to the optical axis, it does not split into O- and E-rays.

The distinction of O- and E-ray exists only within the crystal. Once they emerge from the crystal, they travel with the same velocity. The rays outside the crystal differ only in their direction of travel and plane of polarization.

When any wave advances in space, its phase changes continuously. At a fixed time, the points at x_1 and x_2 on the wave differ in phase by an amount

$$\Delta\phi = \phi_2 - \phi_1$$

where $\phi_1 = (kx_1 - \omega t)$ and $\phi_2 = (kx_2 - \omega t)$, are the respective wave phases at points x_1 and x_2 as established in equation 2.5. Then, the difference in phase is

$$\Delta\phi = k(x_2 - x_1) = \frac{2\pi}{\lambda}L$$

where $L = x_2 - x_1$ is the **geometric path** between points x_1 and x_2. It implies that a displacement by one complete wavelength ($L = \lambda$) leaves the waveform unchanged.

If a ray of light travels a geometric path L in a medium of refractive index n in a certain interval of time, then it would travel a greater distance Δ in air during the same interval of time, therefore

$$\frac{\Delta}{L} = \frac{ct}{\upsilon t} = n$$

this means that the **optical path length** Δ is defined as the product of refractive index and the geometric path length ($\Delta = nL$).

Path differences between two waves may arise if they propagate in a medium along two different paths. Their relationship is defined with the help of their phase difference, which may be expressed in terms of the path difference as follows

$$\Delta\phi = \frac{2\pi}{\lambda} nL = \frac{2\pi}{\lambda}\Delta$$

For a material (like an anisotropic crystal) with two refractive indexes n_e and n_o, the **optical path difference** is

$$D = (n_o - n_e)L$$

This quantity is also known as **relative retardation** since O-ray and E-ray are retarded relative to each other, because of the difference in velocities produced by the different refractive indexes. Retardation can also be expressed as the mutual **phase shift** between the two waves,

$$\Delta\phi = \frac{2\pi}{\lambda}(n_o - n_e)L = \frac{2\pi}{\lambda}D$$

In order to understand how this quantities relate to each other, we are going to refer to an example given by R. Wayne in [84] (Chapter 7, page 144). Imagine putting a positively birefringent specimen, such that $n_e = 1.4805$, $n_o = 1.4555$, thickness $L = 5000$ nm, on a rotating stage in a microscope whose optic axis is +45° (NE-SW) relative to the azimuth of maximal transmission of the polarizer (0°, E-W). Illuminate the specimen with linearly polarized light with a wavelength of $\lambda = 500$ nm. The birefringent specimen resolves the incident linearly polarized light into two orthogonal linearly polarized waves, the O- and E-waves. The E-wave vibrates linearly along the NE-SW axis, and the O-wave vibrates linearly along the SE-NW axis. Then,

$$D = (1.4805 - 1.4555) \cdot 5000 \text{ nm} = 125 \text{ nm}$$

This means the O-wave will be ahead of the E-wave by 125 nm, and the E-wave will be retarded relative to the O-wave by 125 nm. This is equivalent to the extraordinary wave being retarded by

$$\Delta\phi = 125 \text{ nm} \cdot \frac{2\pi}{500 \text{ nm}} = \frac{\pi}{2} \text{ radians}$$

Wollaston and Nomarski prisms

DIC microscopes use an special birefringent prism, called the Wollaston prism, made of two wedge-shaped slabs of birefringent material (generally calcite) cemented along their hypotenuses. The optical axes of the prisms are orthogonal. The Wollaston prism mode of operation can be understood considering the trajectory of a ray which falls on the prism at normal incidence. As shown in Figure 2.12(a), this ray is split by the birefringence of the material. In the first prism both O- and E-rays travel in the same direction, since for normal incidence no change in the ray direction is produced, but have different phase velocities and polarizations, as was already described in subsection 2.1.1.

In the second element of the prism this ray becomes extraordinary. Just to be clear in the

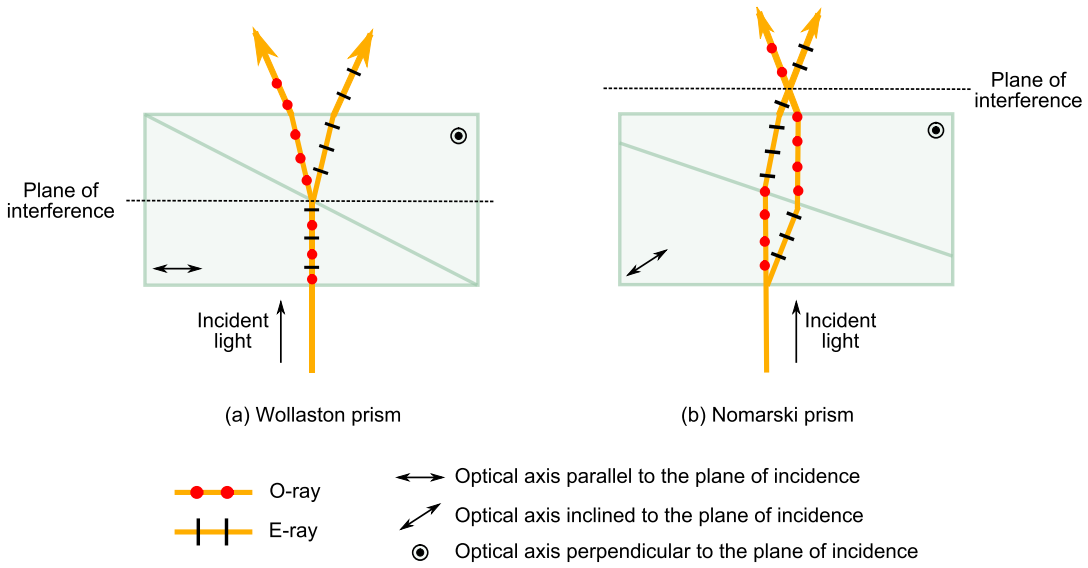

Figure 2.12: Wollaston and Nomarski prisms

notation, we call ordinary rays those which are ordinary in the first prism, and extraordinary those which are extraordinary also in the first prism. After splitting, O- and E-rays are separated by a *shear distance* denoted as $2\Delta x$, which is the same for all O- and E-ray pairs across the face of the prism. We consider that the direction of shear can be in angle with respect to the x-axis, denoted as the *shear angle* τ.

The Nomarski prism is a modified Wollaston prism. One of the wedges is identical to a conventional Wollaston wedge and has the optical axis oriented parallel to the surface of the prism (Figure 2.12(b)). The second wedge of the prism is modified by cutting the crystal in such a manner that the optical axis is oriented obliquely with respect to the flat surface of the prism. The Nomarski modification causes the light rays to come to a focal point outside the body of the prism, and allows greater flexibility so that when setting up the microscope the prism can be actively focused[9] (see Figure 2.12).

Interference of light waves

The phenomenon needed from the wave nature of light to actually generate a contrast image is **interference**. It is an important consequence of the principle of superposition of waves which states that, if two or more waves are propagating through the space, the resultant is given by the sum of wave functions of the individual waves. Thus, if $y_1(x,t)$ and $y_2(x,t)$ are the wave functions characterizing two waves traveling in space, the resultant is given by

$$y(x,t) = y_1(x,t) + y_2(x,t)$$

When harmonic waves of identical frequency propagating in a medium meet each other, they produce the phenomenon of *interference*. Assume two sinusoidal waves of the same frequency

[9]The Nomarski prism (`https://en.wikipedia.org/wiki/Nomarski_prism`)

propagate through different paths and meet in a point P. Let the waves be represented as

$$E_A = E_1 \sin(\omega t - kx_1 + \phi_1)$$
$$E_B = E_2 \sin(\omega t - kx_2 + \phi_2)$$

such that the phase difference $\Delta\phi$ is calculated as

$$\begin{aligned}\Delta\phi &= (-kx_1 + \phi_1) - (-kx_2 + \phi_2) = k(x_2 - x_1) + (\phi_1 - \phi_2) \\ &= \frac{2\pi}{\lambda} nL + (\phi_1 - \phi_2) \\ &= \frac{2\pi}{\lambda}\Delta + (\phi_1 - \phi_2)\end{aligned} \tag{2.8}$$

Following the development done in [6] (chapter 5, page 155), the resultant electric field is given by

$$E^2 = E_1^2 + E_2^2 + \underbrace{2E_1E_2 \cos(\Delta\phi)}_{\text{interference term}} \tag{2.9}$$

The intensity of a wave of light is proportional to the square of its amplitude, $I \propto E^2$, which means that from equation 2.9 we obtain

$$\begin{aligned}I &= I_1 + I_2 + 2\sqrt{I_1 I_2} cos(\Delta\phi) \\ I &= I_1 + I_2 + 2\sqrt{I_1 I_2} \cos\left(\frac{2\pi}{\lambda}\Delta + (\phi_1 - \phi_2)\right)\end{aligned} \tag{2.10}$$

Assuming that the pair of waves are in phase, $\phi_1 = \phi_2$, and that have the same amplitude, $I_1 = I_2$,

$$I = 4I_1 \cos^2\left(\frac{\pi}{\lambda}\Delta\right) \tag{2.11}$$

If $\cos^2\left(\frac{\pi}{\lambda}\Delta\right) = 1$, implies that $I = 4I_1 = I_{max}$, which is called **constructive interference**, and this happens when $\Delta = 0, \lambda, 2\lambda, \cdots, m\lambda$. Otherwise, if $\cos^2\left(\frac{\pi}{\lambda}\Delta\right) = 0$, implies that $I = 0$, which is called **destructive interference**, and this happens when $\Delta = \frac{\lambda}{2}, 3\frac{\lambda}{2}, \cdots, (2m+1)\lambda$, where $m = 0, 1, 2, \cdots$.

Interference under polarized light and birefringence

As will be presented in section 2.2, DIC imaging is accomplished from the interference of two polarized waves that have a lateral differential displacement (shear) and are phase shifted relative one to each other [9]. The displacement and phase shifting is operated by the birefringent Nomarski prism. In section 2.1.1 was explained that the O- and E-rays coming out the prism vibrate in mutually perpendicular planes, because of that they cannot interfere to produce a resultant wave with an altered amplitude but, if the prism is positioned between two crossed polarizers (polarizer and analyzer as in Figure 2.10), it is possible to observe the

interference of the O- and E-rays.

In fact, only the components of the $\overrightarrow{\mathbf{E}}$ vector of both O- and E-rays that vibrate parallel to the transmission axis of the analyzer will emerge. Therefore, after passing the analyzer there is either constructive or destructive interference of coplanar components that are phase shifted. Depending on the amplitude of the resulting wave and its phase differences, the resultant wave will be either linearly, circularly or elliptically polarized (see section 2.1.1 and Figure 2.9).

2.2 DIC microscopy under transmitted light

In the last section we presented the fundamental concepts of polarization, birefringence and interference, which are important to continue with a detailed explanation of the optical components of a DIC microscope, and how the alignment of these components, along their interaction with light, permits to produce a high contrast image of transparent specimens.

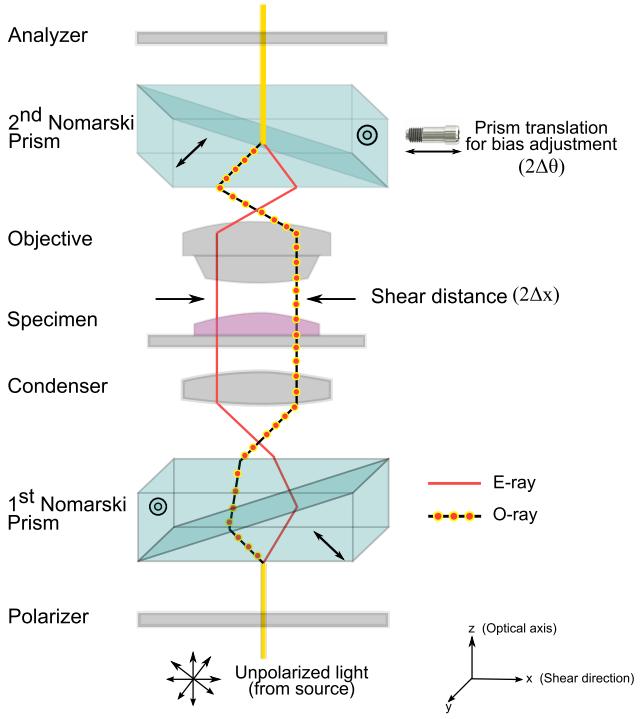

Figure 2.13: Transmitted-light Nomarski DIC microscope

The DIC design is based on the principle of dual-beam interference of polarized light, which transforms local gradients in optical path length in an object into regions of contrast in the object image [65]. We are going to describe the technique using ray tracing of the trajectory of light across all components of Figure 2.13. Coherent unpolarized light coming from a source passes through a linear polarizer lens. Every incident ray of polarized light is passed through a Nomarski prism placed at the front focal plane of the condenser, which acts as a beamsplitter as seen in the previous section. Every point in the specimen is sampled by pairs of beams that

provide dual-beam interference in the image plane [65].

Figure 2.14 presents four possible paths that light can follow across the specimen. For this we use an example presented in [84] (Chapter 9, page 192). Consider four pairs of waves (labeled A, B, C, D) produced by the first Nomarski prism. The prism is placed in such a way with respect to the condenser that O- and E-rays exit as in-phase beams (phase shift $\Delta\phi = 0$). As they are approaching the specimen it can be seen that pair A and pair C experience no optical path differences, whereas for pair B the E-ray experience an optical path difference relative to the the O-ray, and for pair D happens the contrary. Suppose that the specimen introduces a phase retardation of $\pi/2$ radians, and that the second Nomarski prism also introduces $\pi/2$ radians of phase retardation (O-ray is retarded relative to E-ray). Here we describe three scenarios:

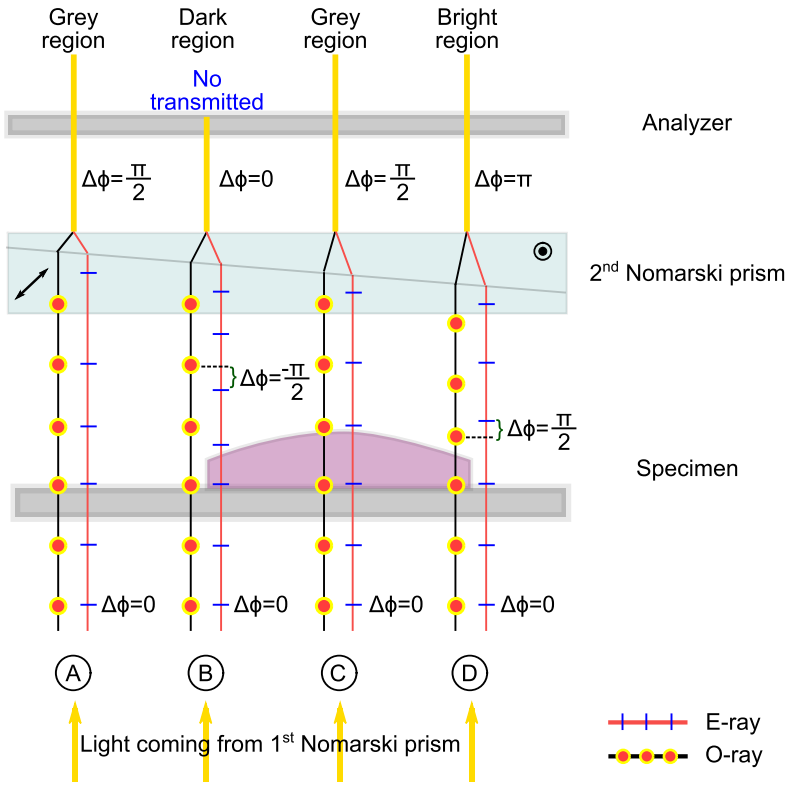

Figure 2.14: Light path across the specimen

(i) Pair A (both O- and E-ray go through the surround), and pair C (both O- and E-ray pass through regions where there are no differences in the optical path length) will be $\pi/2$ radians out-of-phase after they are recombined by the second prism. The resultant wave will be circularly polarized and these regions will appear gray in the image.

(ii) Pair B (E-ray experiences a phase shift as it passes through the specimen) will be 0 radians out-of-phase after being recombined by the second prism. The resultant wave will be linearly polarized *parallel* to the transmission axis of the *polarizer* and this region will be dark.

(iii) Pair D (O-ray experiences a phase shift as it passes through the specimen) will be π radians out-of-phase after being recombined by the second prism. The resultant wave will

be linearly polarized *parallel* to the transmission axis of the *analyzer* and this region in the image will be bright.

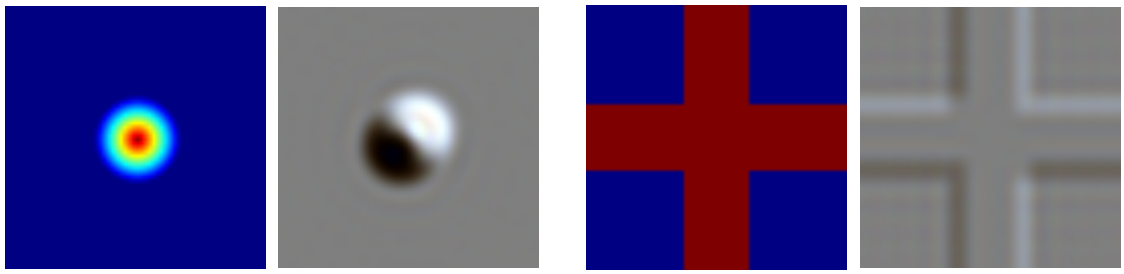

Figure 2.15: Phase functions of two phantom specimens and corresponding noiseless DIC color images: (a) phase function of the "cone" object, (b) DIC image of the cone, (c) phase function of the "cross" object, (d) DIC image of the cross.

On some microscopes **bias retardation** (noted as $2\Delta\theta$) is introduced by advancing or retracting the second Nomarski prism in the light path by turning a positioning screw on the prism holder. Introducing bias retardation makes objects much easier to see, because phase gradients in the specimen are now represented by bright and dark patterns on a gray background. The resultant image exhibits a shadow-cast, 3D, or relief-like appearance that is the distinguished feature of DIC images (see Figure 2.15). It is important to note that the shadows and highlights indicate the signs and slope of phase gradients in the specimen, and not necessarily indicate high or low spots, and the only way of changing the shear direction relative to the specimen is to rotate the specimen itself [4].

2.3 Image Formation Model

For any imaging system, image formation occurs when a sensor registers radiation that has interacted with a physical object [7]. In section 2.2 this was explained from the radiometric (ray tracing) point of view, which was firstly introduced by Walter Lang between 1968 and 1969 for Carl Zeiss Inc. [55]. In this section we are going to present the mathematical model that formally describes the process of encoding the changes in the gradient of the phase of the beams of light illuminating the specimen, to obtain the observed intensity image. Although DIC microscopy is a widely used technique in biology and chemestry (see [49, 3, 50, 81, 82]), not much has been written regarding to its imaging model and eventual design of computational methods for image and phase reconstruction. In order to give some background to the model we have used, we first present a review of the related work in chronological order for the computational model as follows.

2.3.1 Related work of DIC imaging models

Most of the literature references in DIC microscopy coincide to mention that the first computational simulation was proposed by Galbraith and David in 1976 [39]. Taking as point

of departure the references of Allen, Nomarski [4] and Lang [55], they suggested that it was necessary to produce a simulation that could support the experimental work of microscopists who were starting to use the DIC microscope, and probably misunderstanding its utilities and giving wrong interpretations of the observed images. This was an educational tool and it was not based on any mathematical ground, reason for which their demonstrations were not accurate.

Several years after appeared another approach combining signal processing and Fourier optics, proposed by Holmes and David in [45] and [44]. In their model, the pair of beams splitted by the Wollaston prism were represented as signals, which were affected by the objective lens that was modeled as a low-pass filter, whose kernel is a linear space-invariant system defined by the pupil function of the objective, and cut-off frequency equal to the relation $\frac{NA}{\lambda}$. The model was used to simulate synthetic data but it was not verified with observed data. From this model they proposed a method for phase reconstruction following the Gerchberg-Saxton [40] iterative algorithm, obtaining promising results.

DIC microscopy has been recognized for high lateral resolution as a consequence of acquisitions at high numerical apertures; recently it has been also improved axial resolution of less than 20 nm by adjusting the amount of photons in the illumination source [67]. Even though, it has a drawback when imaging thick specimens. For this reason, Cogswell and Sheppard [29] designed a confocal DIC microscope. Their goal was to take advantage of convential DIC microscopy to capture phase information at high lateral resolution, while improving its axial resolution through a confocal microscope. They stated that convential DIC works under partially coherent illumination, while the confocal DIC case is purely coherent, which provides easier and fast computations. However, the use of confocal DIC had not been spread because of the difficulty to align the DIC optical components into a confocal configuration as it was corroborated by Cody et al in [27].

Following another method, Kagalwala and Kanade [47] proposed a vectorial representation for the image formation in DIC microscopy. This approach is based on polarization ray-tracing, on which Jones vectors and Jones matrices are used to represent the interaction of light with each one of the optical components of the microscope. In this work they modeled the specimen as a 3-D grid of voxels, and the interaction of rays at multiple surface boundaries.

One characteristic that plays an important role in DIC microscopy, is that the image formation is dependent on the orientation of shear in order to detect properly the changes on the gradients of the phase, as well as to improve contrast. C. Preza et al. [75], [72], presented the *Rotational Diversity Model* that have become the most important reference in DIC microscopy; for this reason it was taken as the starting point for the purposes of the present thesis. In the following subsection are presented the details of this model.

As is going to be explained later, the intensity image of DIC microscope is originated from a nonlinear relation between the point-spread function of the microscope and the phase function

of light. This nonlinearity makes computations not simple, reason why Arnison et al. [58] proposed to combine different techniques in order to transform the model as a linear one. They proposed to acquire images at two shear directions (as proposed by Preza in [72]) and then use phase shifting algorithm with four different bias orientations to extract the gradient of the phase function for each of the shear directions. From there, it is possible to apply Fourier space integration and its inverse to obtain an estimation of the phase function.

In order to overcome the shear orientation dependence of DIC images, Shribak and Inoué [79] designed a new model to compute the magnitude and azimuth of the optical path gradients. For this they did calculations using three different configurations: i) Four images at different shear orientations (steps of 90°) with fixed bias and 2 images without bias; ii) Four images at different shear orientations (steps of 90°) with fixed bias; iii) Two images at different shear orientations (steps of 90°) with fixed bias and 2 images without specimen. At each of these configurations they combined the different measurements of magnitude and azimuth of the gradient of the phase, to finally deduce a more general analytical expression that does not depend on the shear orientation. They found a drawback when using only 2 images.

All of these models had been developed assuming coherent light under Köhler illumination. However, later in 2008, Mehta and Sheppard [62] developed another model considering the case of partially coherent light and not perfect Köhler illumination. They also proposed a methodology for callibrating the acquisition paramaters of the DIC microscope in [63]. Later, Mehta and Oldenbourg [61] developed a library called *Microlith*, for biological imaging simulation, considering different optical microscopy techniques, included DIC, and introducing optical and chromatic aberrations.

After this review we have determined to follow the inverse problems approach to recover the phase from DIC images. In order to do so, we have chosen the model proposed by Preza et al. in [72], as the forward model to generate the phantom objects and synthetic data.

2.3.2 Polychromatic DIC model

According to what was explained in section 2.2, the most important parameters to produce a DIC image are: the shear direction, the shear distance ($2\Delta x$) and the bias retardation ($2\Delta\theta$). The shear direction is crucial for detecting the directional derivatives of the specimen. The shear distance is determined by the optical characteristics of the prism, and it is desirable to be less than the resolution of the microscope. The quality of the contrast of the image is adjusted by the lateral displacement of the second prism which is called the bias retardation.

In the model presented by Preza in [72], called the "Rotational diversity" model, in order to retrieve the optical path length of the specimen, it is necessary to simulate the acquisition of at least two images with a shear angle difference of $\pi/2$, which in practical terms means the mechanical rotation of the specimen stage. For the purpose of mathematical modeling, *"the specimen rotation can be modeled as a rotation of the point spread function by an angle, τ_k,*

defined as the angle that the shear direction makes with the horizontal axis". Hence, this model assumes that K ($K \geq 2$) images are acquired by rotating the specimen K times with respect to the shear axis, which results in K rotations of the amplitude point spread function (PSF). This model was developed for monochromatic illumination as is shown in equations 2 and 4 in [72] that we recall here

$$i(x,y) = a_1 \left| h_k(x,y) \otimes e^{-i\phi(x,y)} \right|^2 \tag{2.12}$$

$$h_k(x,y) = \frac{1}{2}\left[e^{-i\Delta\theta} k(x-\Delta x, y) - e^{i\Delta\theta} k(x+\Delta x, y) \right] \tag{2.13}$$

Since recent technology of DIC microscopes are equipped to acquire images under white illumination, here we have extended the rotational diversity model to polychromatic illumination (RGB color model), which we have called the "Polychromatic Rotational-Diversity" model, already presented in [9]. In this configuration, the relation between the acquired images and the unknown true phase ϕ is given by

$$(o_{k,\lambda_\ell})_j = a_1 \left| (h_{k,\lambda_\ell} \otimes e^{-i\phi/\lambda_\ell})_j \right|^2 + (\eta_{k,\lambda_\ell})_j, \tag{2.14}$$

for $k = 1, \ldots, K$, $\ell = 1, 2, 3$, $j \in \chi$, where

- k is the index of the angles τ_k that the shear direction makes with the horizontal axis [72], ℓ is the index denoting one of the three RGB channels and $j = (j_1, j_2)$ is a 2D–index varying in the set $\chi = \{1, \ldots, M\} \times \{1, \ldots, P\}$, M and P meaning the size of the acquired image, which is determined by the resolution of the CCD detector of the microscope, with typical value of 1388×1040 pixels.

- λ_ℓ is the ℓ–th illumination wavelength. The object is illuminated with white light, whose wavelengths range from 400 nm to 700 nm. The digital acquisition system of the microscope comprises a color bandpass filter which isolates the RGB wavelengths, acquired separately by the CCD detector [65]. Since it is selected a narrow band for each color, we use the mean wavelength at each band. Since it is selected a narrow band for each color, we use the mean wavelength $\lambda_e ll$ at each band.

- $o_{k,\lambda_\ell} \in \mathbb{R}^{MP}$ is the $\ell-$th color component of the $k-$th discrete observed image $o_k = (o_{k,\lambda_1}, o_{k,\lambda_2}, o_{k,\lambda_3}) \in \mathbb{R}^{MP\times 3}$;

- $\phi \in \mathbb{R}^{MP}$ is the unknown phase vector and $e^{-i\phi/\lambda_\ell} \in \mathbb{C}^{MP}$ stands for the vector defined by $(e^{-i\phi/\lambda_\ell})_j = e^{-i\phi_j/\lambda_\ell}$;

- $h_{k,\lambda_\ell} \in \mathbb{C}^{MP}$ is the discretization of the continuous DIC point spread function [75, 43] corresponding to the illumination wavelength λ_ℓ and rotated by the angle τ_k , i.e.,

$$h_{k,\lambda_\ell}(x,y) = \frac{1}{2}\left[e^{-i\frac{\Delta\theta}{\lambda_\ell}} p_{\lambda_\ell}\left(R_k \cdot (x-\Delta x, y)^T\right) - e^{i\frac{\Delta\theta}{\lambda_\ell}} p_{\lambda_\ell}\left(R_k \cdot (x+\Delta x, y)^T\right)\right], \tag{2.15}$$

  where $p_{\lambda_\ell}(x,y)$ is the coherent PSF of the microscope's objective lens for the wavelength λ_ℓ, which is given by the inverse Fourier transform of the disk support function $P_{\lambda_\ell}(m,n)$

of amplitude 1 and radius equal to the cutoff frequency $f_c = \text{NA}/\lambda_\ell$ [75], being NA the numerical aperture of the objective lens, $2\Delta\theta$ is the DIC bias retardation, $2\Delta x$ is the shear distance and R_k is the rotation matrix which rotates the coordinates according to the shear angle τ_k. In the frequency domain it is defined as

$$H_{k,\lambda_\ell}(m,n) = -i \sin\left(2\pi R_k \cdot m\Delta x + \frac{\Delta\theta}{\lambda_\ell}\right) P_{\lambda_\ell}(m,n) \tag{2.16}$$

where m, n are the frequency axes with limits in the interval $\left[-\frac{f_s}{2}, \frac{f_s}{2}\right]$, with f_s being the sampling Nyquist frequency, such that $f_s > 2f_c$.

- $h_1 \otimes h_2$ denotes the 2D convolution between the two $M \times P$ images h_1, h_2, extended with periodic boundary conditions;
- $\eta_{k,\lambda_\ell} \in \mathbb{R}^{MP}$ is the noise corrupting the data, which is assumed to be a realization of a Gaussian random vector with mean $\mathbf{0} \in \mathbb{R}^{MP}$ and covariance matrix $\sigma^2 I_{(MP)^2}$, where $I_{(MP)^2}$ is the identity matrix of size $(MP)^2$;
- $a_1 \in \mathbb{R}$ is a constant which corresponds to closing the condenser aperture down to a single point.

We already mentioned that DIC microscopy is diffraction limited by the action of the pupil function of the system, as can be verified in equation (2.15). In the following subsection we present a detailed analysis of the point spread function $h_{k,\lambda_\ell}(x,y)$, since it models the sheared phase-shifted beams that go through the specimen, and the additional retardation they suffer because of the bias introduced by the Nomarski prism before arriving to the image plane of the microscope.

2.3.3 Point spread function for DIC microscopy

Here we want to state the main characteristics of the polychromatic PSF defined in equations (2.15) and (2.16). The parameters for simulations are:

$\text{NA} = 0.3$	$\tau_1 = -\pi/4$	$\lambda_1 = 0.65\ \mu\text{m}$
$2\Delta x = 0.68\ \mu\text{m}$	$\tau_2 = \pi/4$	$\lambda_2 = 0.55\ \mu\text{m}$
$2\Delta\theta_1 = 0$	$2\Delta\theta_2 = \pi/2$	$\lambda_3 = 0.45\ \mu\text{m}$

Figure 2.16 shows the real (Real{}) and imaginary (Imag{}) parts of the PSF, each one calculated for shear angles τ_1 and τ_2, and a fixed bias retardation $2\Delta\theta_1 = 0$. Figure 2.17 shows the corresponding to bias retardation $2\Delta\theta_2 = \pi/2$. In all plots is observed the diffraction effect of each pupil function, which increases from the largest to the shortest wavelength. The two bright spots on the imaginary parts represent the two sheared and phase-shifted beams. The dark band in the middle of the two spots is the shear distance $2\Delta x$ established by the Nomarski prism. Although the real parts seem to be quite similar for both bias retardation values, it is more evident the difference by observing the imaginary parts.

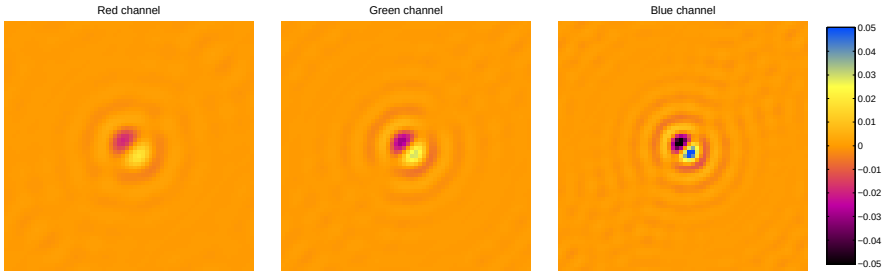

(a) Real$\{h_{1,\lambda_\ell}(x,y)\}$; $\tau_1 = -\pi/4$

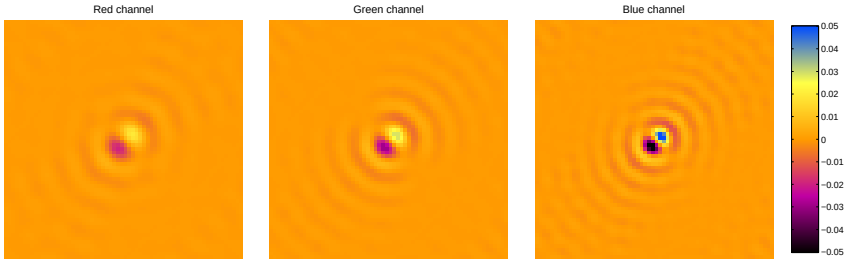

(b) Real$\{h_{2,\lambda_\ell}(x,y)\}$; $\tau_2 = \pi/4$

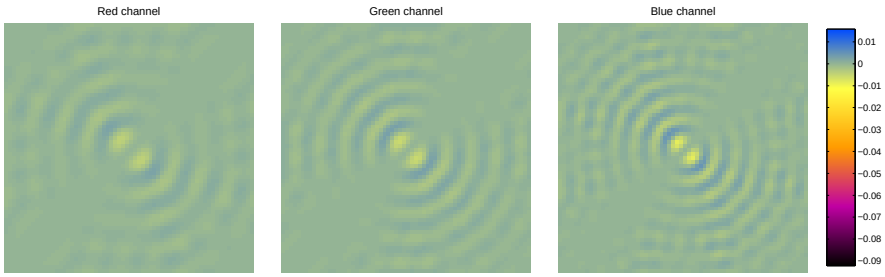

(c) Imag$\{h_{1,\lambda_\ell}(x,y)\}$; $\tau_1 = -\pi/4$

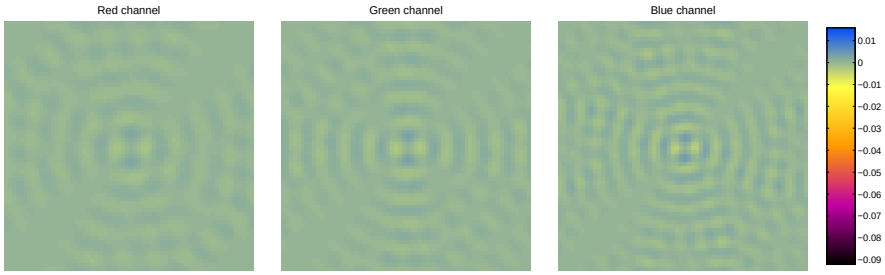

(d) Imag$\{h_{2,\lambda_\ell}(x,y)\}$; $\tau_2 = \pi/4$

Figure 2.16: Effect of shear angle, bias retardation and wavelength values on polychromatic PSF. Case 1: $2\Delta\theta_1 = 0$

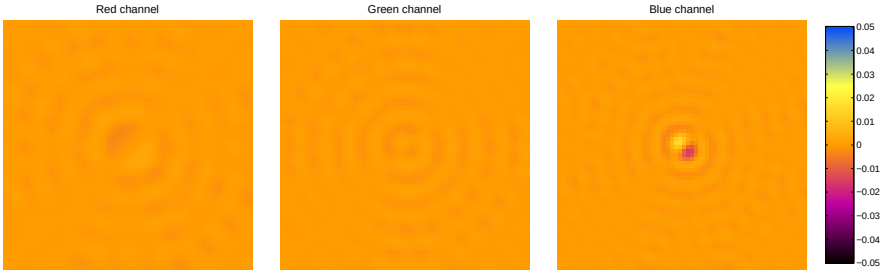

(a) Real$\{h_{1,\lambda_\ell}(x,y)\}$; $\tau_1 = -\pi/4$

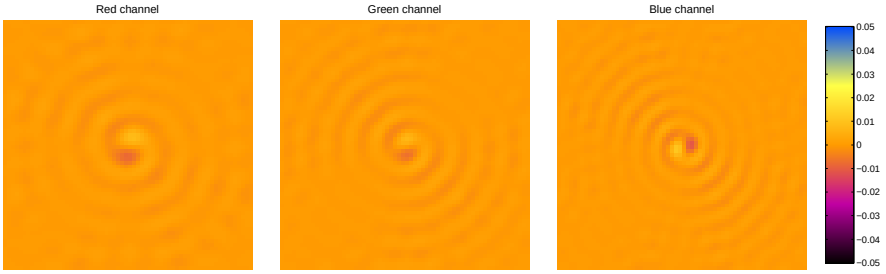

(b) Real$\{h_{2,\lambda_\ell}(x,y)\}$; $\tau_2 = \pi/4$

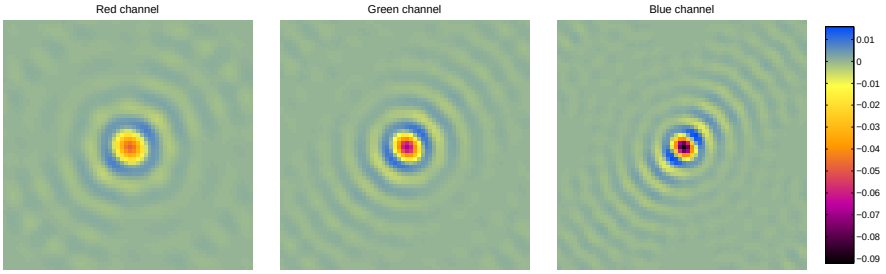

(c) Imag$\{h_{1,\lambda_\ell}(x,y)\}$; $\tau_1 = -\pi/4$

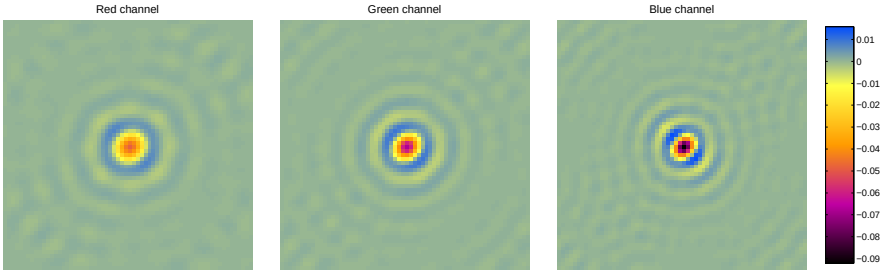

(d) Imag$\{h_{2,\lambda_\ell}(x,y)\}$; $\tau_2 = \pi/4$

Figure 2.17: Effect of shear angle, bias retardation and wavelength values on polychromatic PSF. Case 1: $2\Delta\theta_2 = \pi/2$

In the Fourier domain it is more clear how all parameters work together to establish the frequency support of the PSF, as shown in Figure 2.18. As it was already mentioned, here is evident that the smallest wavelength (Blue channel) provides more frequency information. It is also visible the dependence of the bias retardation on the wavelength values. To observe this in more detail, it is useful to plot the horizontal and vertical profiles of the PSF as in Figure 2.19 and Figure 2.20, where we have fixed the shear angle to $\tau_1 = -\pi/4$ and we see again the influence of the wavelengths for two values of bias retardation.

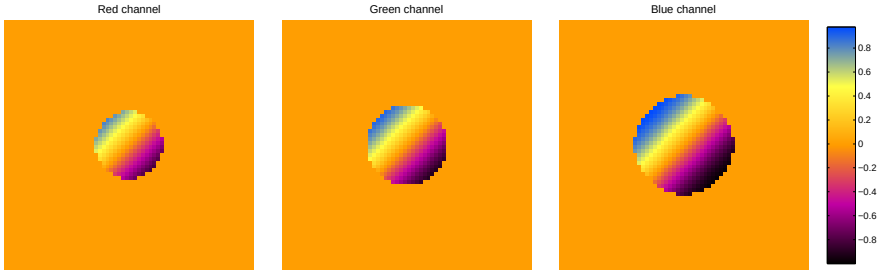

(a) Imag$\{H_{1,\lambda_\ell}(m,n)\}$; $\tau_1 = -\pi/4$

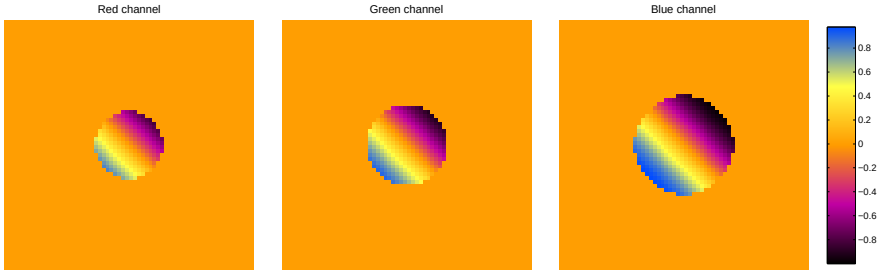

(b) Imag$\{H_{2,\lambda_\ell}(m,n)\}$; $\tau_2 = \pi/4$

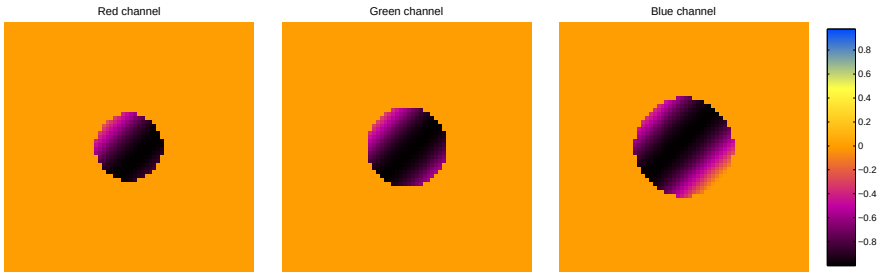

(c) Imag$\{H_{1,\lambda_\ell}(m,n)\}$; $\tau_1 = -\pi/4$

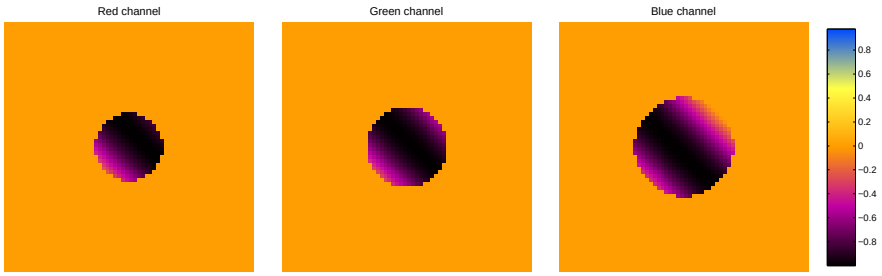

(d) Imag$\{H_{2,\lambda_\ell}(m,n)\}$; $\tau_2 = \pi/4$

Figure 2.18: Frequency domain support of polychromatic PSF. (a)-(b) $2\Delta\theta_1 = 0$; (c)-(d) $2\Delta\theta_2 = \pi/2$

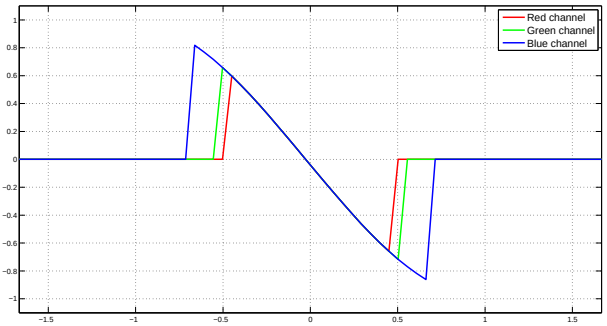

(a) Imag$\{H_{1,\lambda_\ell}(m,0)\}$; $\tau_1 = -\pi/4$

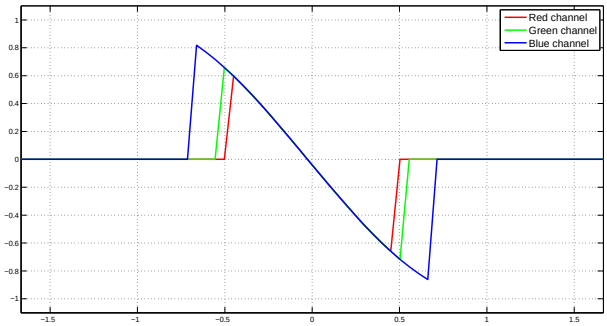

(b) Imag$\{H_{1,\lambda_\ell}(0,m)\}$; $\tau_1 = -\pi/4$

Figure 2.19: Vertical and horizontal profiles of polychromatic PSF. $2\Delta\theta_1 = 0$

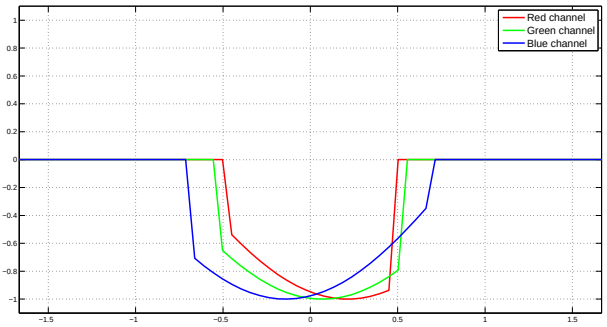

(a) Imag$\{H_{1,\lambda_\ell}(m,0)\}$; $\tau_1 = -\pi/4$

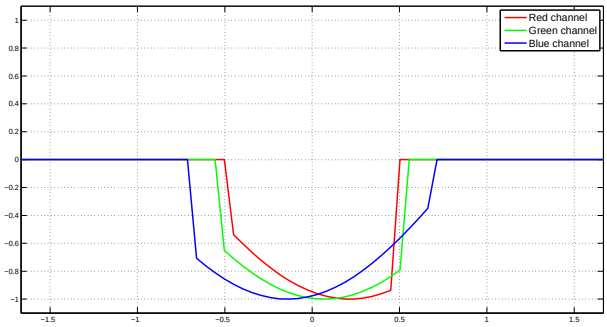

(b) Imag$\{H_{1,\lambda_\ell}(0,m)\}$; $\tau_1 = -\pi/4$

Figure 2.20: Vertical and horizontal profiles of polychromatic PSF. $2\Delta\theta_2 = \pi/2$

Since DIC microscopy is sensible to the shear direction, we did the same analysis of the PSF in the case when the shear angle is equal to 0 and $\pi/2$. The results are included in Appendix A.

Influence of the numerical aperture

DIC microscopy has been recognized by its capability of allowing high numerical apertures in order to provide more illumination to the specimen and therefore, to produce high resolution images. To verify this fact, we have done the same analysis of the PSF with a different value of the numerical aperture set to 0.9; we have maintained the same values for the microscope parameters. Figures 2.21 and 2.22 illustrate the changes on the PSF.

The first change is the decreasing in the size of the bright spots, which introduces better resolution and precision, being more evident for bias retardation of $\pi/2$.

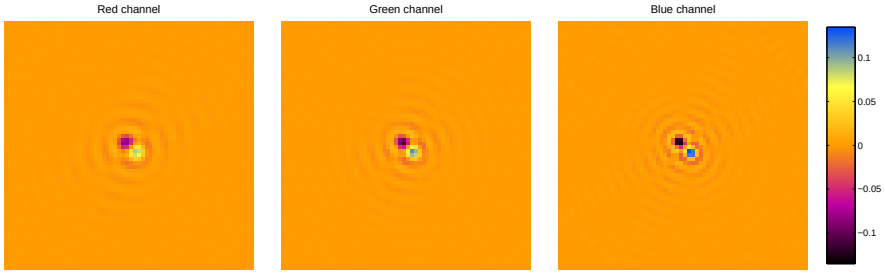

(a) Real$\{h_{1,\lambda_\ell}(x,y)\}$; $\tau_1 = -\pi/4$

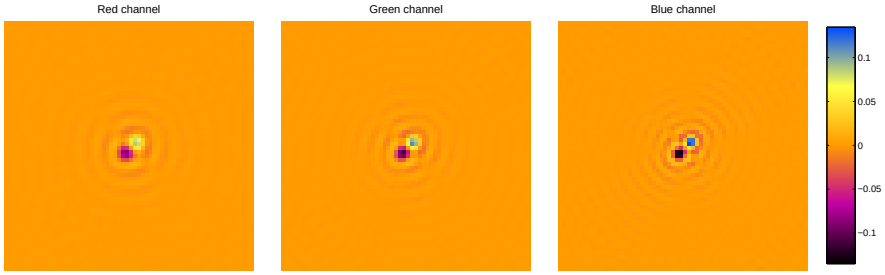

(b) Real$\{h_{2,\lambda_\ell}(x,y)\}$; $\tau_2 = \pi/4$

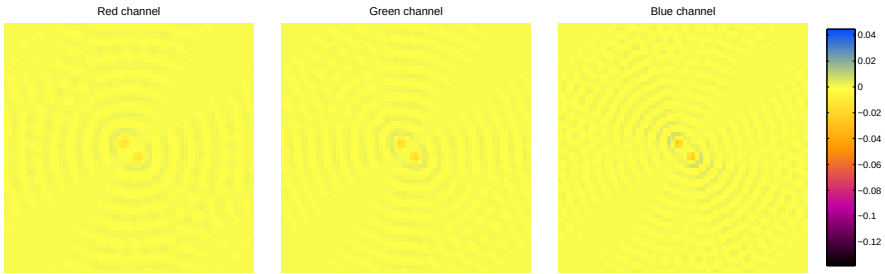

(c) Imag$\{h_{1,\lambda_\ell}(x,y)\}$; $\tau_1 = -\pi/4$

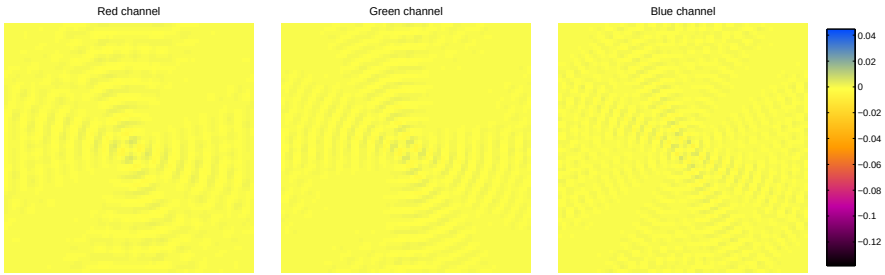

(d) Imag$\{h_{2,\lambda_\ell}(x,y)\}$; $\tau_2 = \pi/4$

Figure 2.21: Effect of NA $= 0.9$ on polychromatic PSF. Case 1: $2\Delta\theta_1 = 0$

(a) Real$\{h_{1,\lambda_\ell}(x,y)\}$; $\tau_1 = -\pi/4$

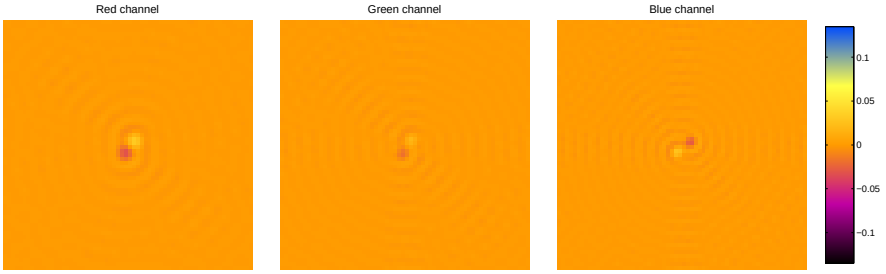

(b) Real$\{h_{2,\lambda_\ell}(x,y)\}$; $\tau_2 = \pi/4$

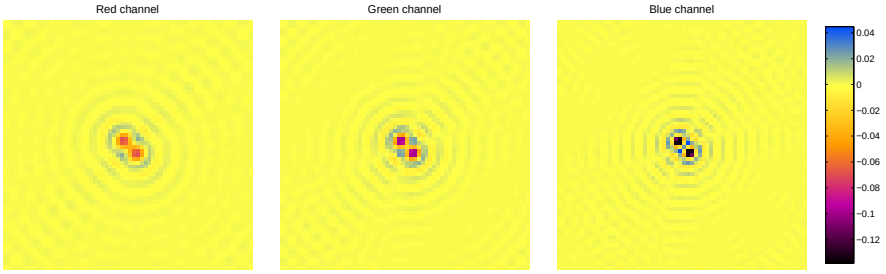

(c) Imag$\{h_{1,\lambda_\ell}(x,y)\}$; $\tau_1 = -\pi/4$

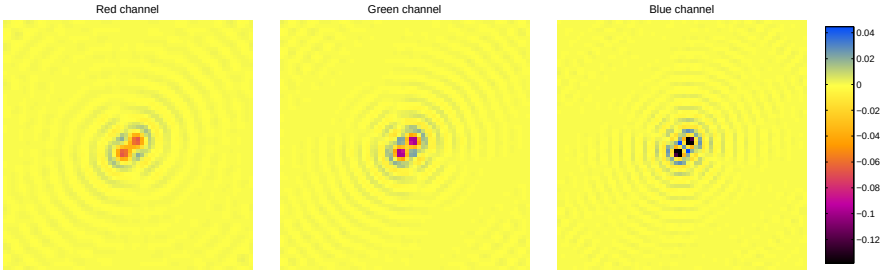

(d) Imag$\{h_{2,\lambda_\ell}(x,y)\}$; $\tau_2 = \pi/4$

Figure 2.22: Effect of NA $= 0.9$ on polychromatic PSF. Case 1: $2\Delta\theta_2 = \pi/2$

As in the previous case, we present the frequency support in Figure 2.23. We can observe the increasing in the size for all PSFs, and also the increasing in the oscillations inside the domain of the functions, as well as more symmetric behavior when bias retardation is $\pi/2$. This is also observed in the vertical and horizontal profiles shown in Figures 2.24 and 2.25. With this we can conclude that high numerical aperture gives better resolution since it increases the frequency support of the PSF in the Fourier domain.

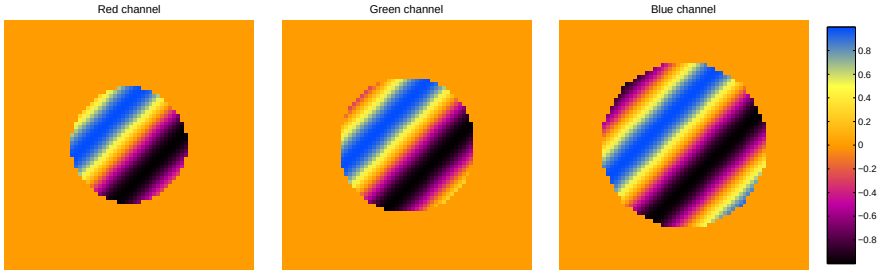

(a) Imag$\{H_{1,\lambda_\ell}(m,n)\}$; $\tau_1 = -\pi/4$

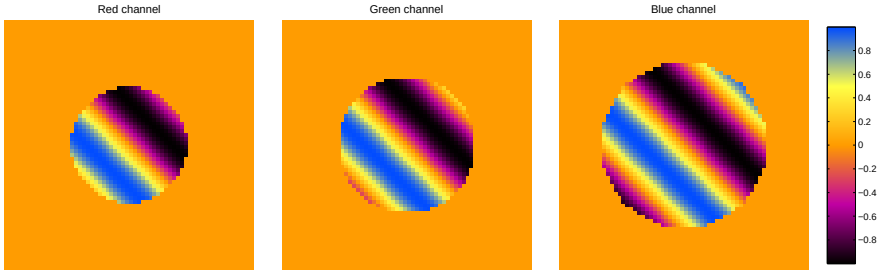

(b) Imag$\{H_{2,\lambda_\ell}(m,n)\}$; $\tau_2 = \pi/4$

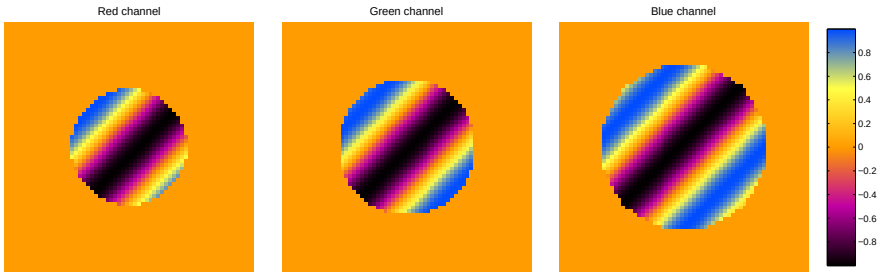

(c) Imag$\{H_{1,\lambda_\ell}(m,n)\}$; $\tau_1 = -\pi/4$

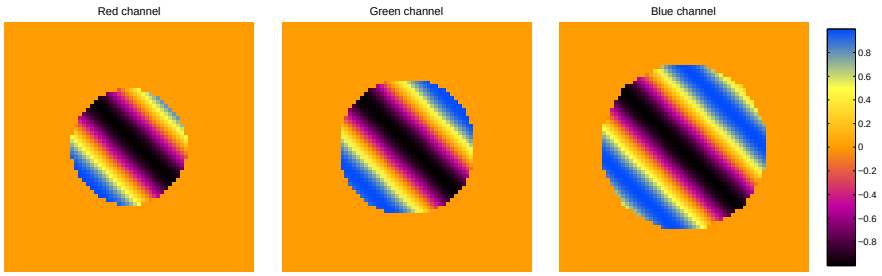

(d) Imag$\{H_{2,\lambda_\ell}(m,n)\}$; $\tau_2 = \pi/4$

Figure 2.23: Frequency domain support of polychromatic PSF. (a)-(b) $2\Delta\theta_1 = 0$; (c)-(d) $2\Delta\theta_2 = \pi/2$

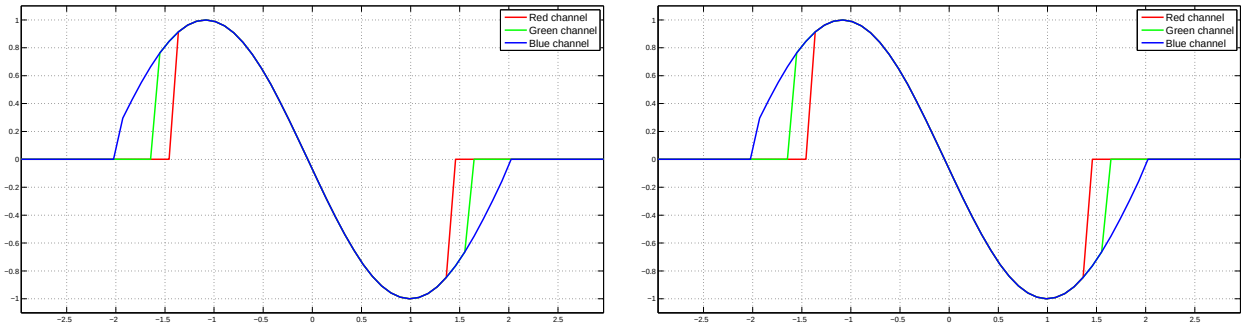

(a) Imag$\{H_{1,\lambda_\ell}(m,0)\}$; $\tau_1 = -\pi/4$ (b) Imag$\{H_{1,\lambda_\ell}(0,m)\}$; $\tau_1 = -\pi/4$

Figure 2.24: Vertical and horizontal profiles of polychromatic PSF. $2\Delta\theta_1 = 0$

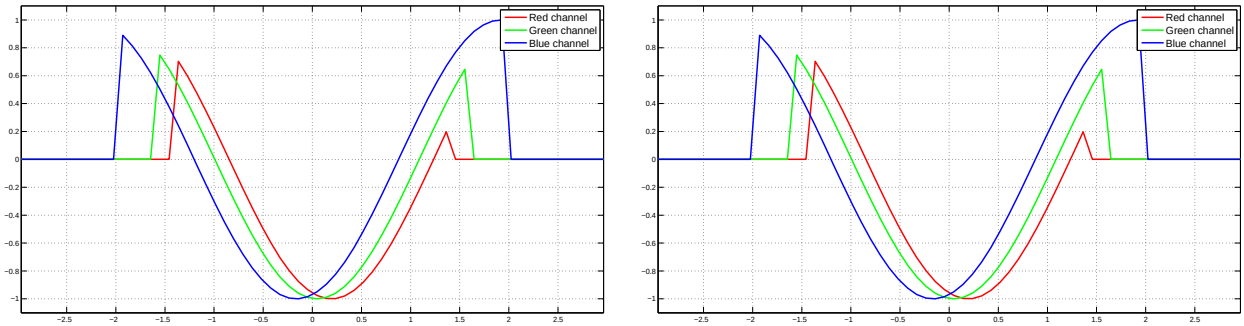

(a) Imag$\{H_{1,\lambda_\ell}(m,0)\}$; $\tau_1 = -\pi/4$ (b) Imag$\{H_{1,\lambda_\ell}(0,m)\}$; $\tau_1 = -\pi/4$

Figure 2.25: Vertical and horizontal profiles of polychromatic PSF. $2\Delta\theta_2 = \pi/2$

2.3.4 Observed DIC images

Now that we have presented the details of the DIC PSF, we can discuss the output of the imaging model in Equation (2.14). For this we can assume a theoretical phase object with a cross shape as in Figure 2.26; the dark areas correspond to zero phase values, and the maximum value in the light area corresponds to a phase value of 0.14 radians. Figures 2.27 and 2.28 show the results after convolving the true phase object with the PSF, under different configurations of numerical aperture, shear angle and bias retardation. The simulations were done with noise level of 4.5 dB. Further results for shear angle in $\{0, \pi/2\}$ are in Figures A.9 and A.10.

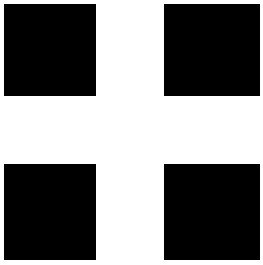

Figure 2.26: Simulated true phase object

It can be noticed that for bias retardation of $2\Delta\theta = 0$, there is no observable object, due to the fact that at this value, the PSF in the Fourier domain (Equation (2.16)) has its minimum, what in practical terms means absence of contrast. The opposite happens when $2\Delta\theta = \pi/2$.

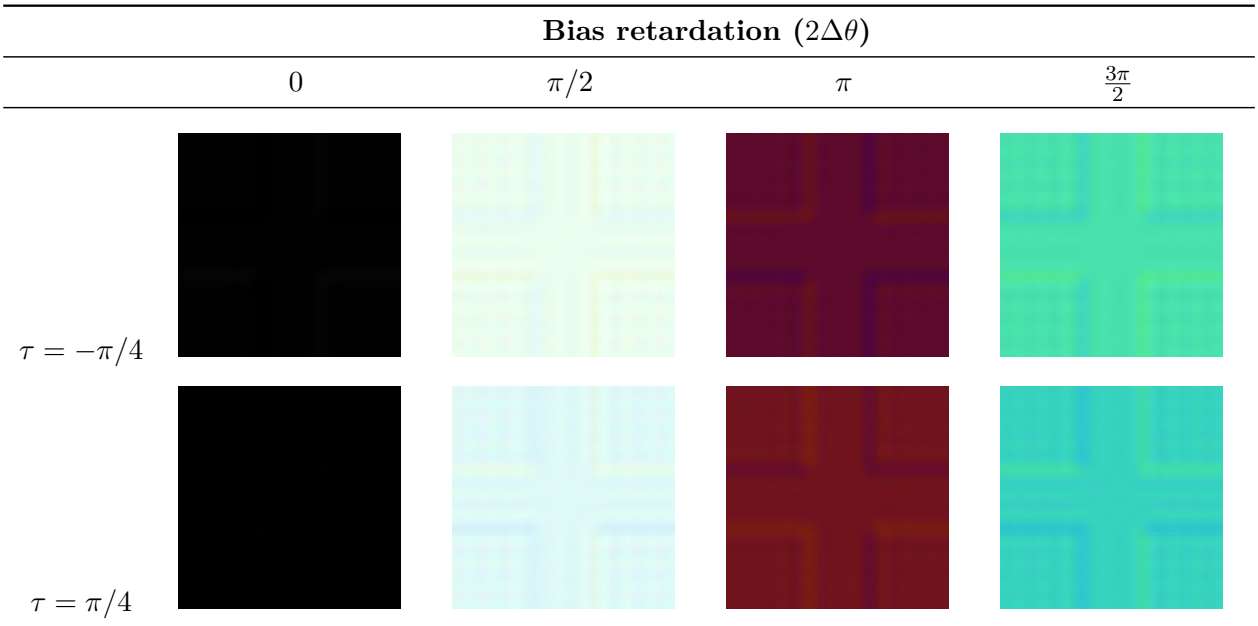

Figure 2.27: Observed DIC images for different combinations of shear angle and bias retardation. NA = 0.3

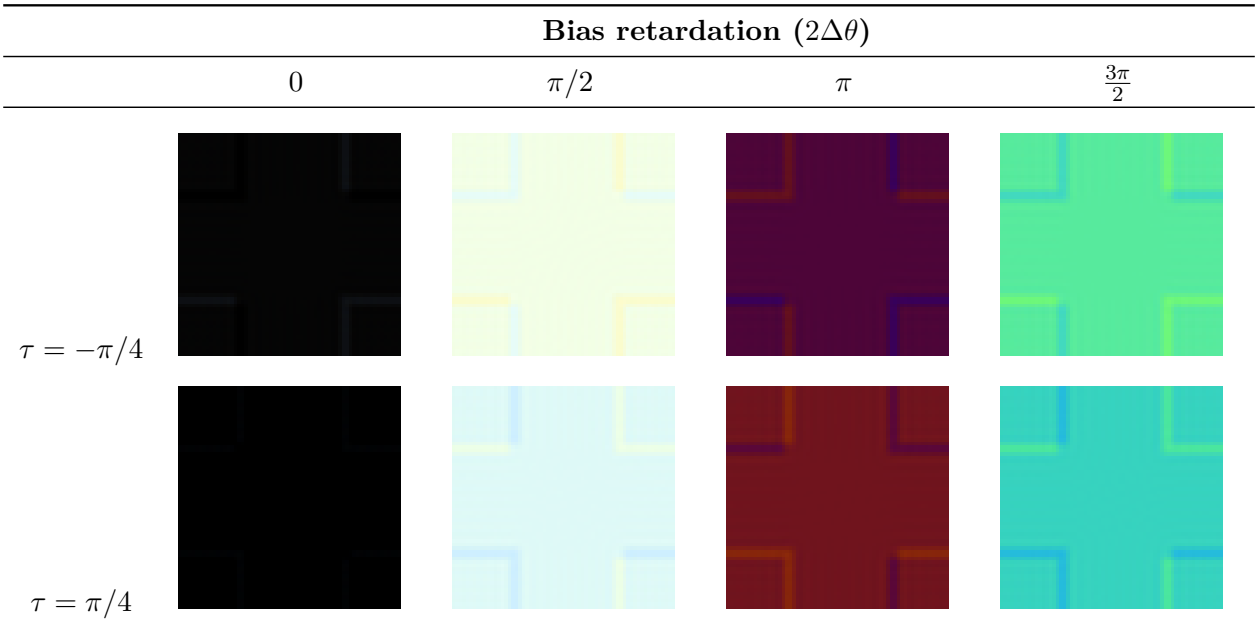

Figure 2.28: Observed DIC images for different combinations of shear angle and bias retardation. NA = 0.9

2.4 Summary

In this chapter we introduced some of the physical and optical concepts needed to understand DIC microscopy. We also described the image formation model for this technique, and we presented the polychromatic model in order to have into account information provided by three different wavelengths. There were also described the main characteristics of the DIC point spread function under different microscope parameters configuration, in both spatial and frequency domains. At the end it was also presented a comparison of the resulting observed images for the possible configurations we studied for the PSF, leaving as a conclusion to take advantage of the high numerical aperture capacity of DIC microscope to produce better resolved images. In this order of ideas, we have chosen as proper configuration for simulation of phantom objects the following parameters: NA $= 0.9$; shear distance $2\Delta x = 0.68$ μm; shear angle $\{-\pi/4, \pi/4\}$; bias retardation $2\Delta\theta = \pi/2$.

Chapter 3

Phase Estimation in DIC microscopy

DIC microscopy lacks the ability to provide morphological analysis of the observed object, since the information regarding to refractive indexes and optical path length differences of light is encoded into the exponential function of the nonlinear relationship established in model (2.14). The argument of the exponential represents the phase of the light beams traversing the physical object. Then, in order to obtain morphological information from a DIC image, it is needed to recover the phase function $\phi(x, y)$ from the K observed RGB images $o_{1,\lambda_\ell}, \ldots, o_{K,\lambda_\ell}$.

This problem can be addressed by means of the maximum likelihood (ML) approach. Assuming that the $3K$ images o_{k,λ_ℓ} are corrupted by Gaussian noise, then the negative log likelihood of each image is a least-squares measure, which is nonlinear due to the presence of the exponential inside the modulus square in (2.14). If we assume white Gaussian noise, statistically independent of the data, the negative log likelihood of the problem is the sum of the negative log likelihoods of the different images, namely the following fit-to-data term

$$J_0(\phi) = \sum_{\ell=1}^{3} \sum_{k=1}^{K} \sum_{j \in \chi} \left[(o_{k,\lambda_\ell})_j - a_1 \left| (h_{k,\lambda_\ell} \otimes e^{-i\phi/\lambda_\ell})_j \right|^2 \right]^2. \tag{3.1}$$

Then the ML approach to the phase reconstruction problem consists in the minimization of the function in (3.1):

$$\min_{\phi \in \mathbb{R}^{MP}} J_0(\phi). \tag{3.2}$$

Another approaches have been proposed to solve the problem of phase reconstruction from images obtained with model (2.14), such as phase-shifting interferometry [60, 31], phase retrieval [78, 40, 34, 23], transport-of-intensity equation [52, 19], and iterative methods [72, 73]. In the following section we present a brief review of these methods. In section 3.2 we prove the properties of existence and non-uniqueness of problem 3.2. Section 3.4 is devoted to describe two iterative approaches we proposed to assure fast convergence to the solution of this problem.

The results of this chapter have been collected into an article entitled "A comparison of edge-preserving approaches for differential interference contrast microscopy", accepted to the Inverse Problems Journal (article reference IP-101183.R3). This was done in collaboration with Dr. Luca Zanni, Dr. Marco Prato and PhD student Simone Rebegoldi, from the department of Physics, Computer Science and Mathematics of the University of Modena and Reggio Emilia in Italy.

3.1 Review of existing methods

3.1.1 Phase-shifting interferometry

This technique originated as a mean to test and characterize perfect optical surfaces [60], on which several interferograms are taken with different phase shifts (bias retardation). The accuracy in the setup for the acquisition at different biases is controlled by a piezo-electric transducer. In the DIC microscope this happens at the second Nomarski prism, which is translated laterally in order to induce the bias retardation. In commercial microscopes such as the Carl Zeiss Axio Imager z1[1], this can be adjusted automatically by software or manually by rotating a knob as illustrated in Figure 2.13.

In section 2.2 it was explained that the specimen is traversed by a pair of orthogonally polarised beams with the following complex amplitudes:

$$b_1 = a_1 e^{i(\phi_1 - \Delta\theta)}$$
$$b_2 = a_2 e^{i(\phi_2 + \Delta\theta)}$$

where $\phi_1 - \phi_2 = \Delta\phi$ is the phase difference caused by the specimen phase gradient and $2\Delta\theta$ is the bias retardation. The observed intensity image is the result of the interference of the two beams, which is computed as

$$I = |b_1 + b_2|^2 = a_1^2 + a_2^2 + 2a_1 a_2 \cos(\Delta\phi + 2\Delta\theta)$$

On this equation there are four variables, where we want to retrieve the unknown $\Delta\phi$. In order to build a linear system, it is necessary to acquire four images such that $2\Delta\theta$ is incremented by $\pi/2$ radians each time. This is known as the ***4-step algorithm***:

$$\begin{aligned}
I_0 &= a_1^2 + a_2^2 + 2a_1 a_2 \cos(\Delta\phi) \\
I_{\frac{\pi}{2}} &= a_1^2 + a_2^2 + 2a_1 a_2 \cos\left(\Delta\phi + \frac{\pi}{2}\right) &&= a_1^2 + a_2^2 + 2a_1 a_2 \sin(\Delta\phi) \\
I_{\pi} &= a_1^2 + a_2^2 + 2a_1 a_2 \cos(\Delta\phi + \pi) &&= a_1^2 + a_2^2 - 2a_1 a_2 \cos(\Delta\phi) \\
I_{\frac{3\pi}{2}} &= a_1^2 + a_2^2 + 2a_1 a_2 \cos\left(\Delta\phi + \frac{3\pi}{2}\right) &&= a_1^2 + a_2^2 - 2a_1 a_2 \sin(\Delta\phi)
\end{aligned}$$

where the phase difference is computed as

$$\Delta\phi = \tan^{-1} \frac{I_{\frac{\pi}{2}} - I_{\frac{3\pi}{2}}}{I_0 - I_\pi}$$

This algorithm has been previously used for DIC microscopy by Cogswell et al in [28] and Arnison et al in [58]. From this works it has been explored the method of Fourier phase integration and the Hilbert transform [59] to retrieve the exact phase function.

[1] `https://www.zeiss.com/microscopy/int/products/light-microscopes/axio-imager-2-for-biology.html`

Phase-shifting interferometry have the drawback of sensitivity to noise and the inherent ambiguity of the arctangent function which wraps the phase variations with phase jumps, which is a recurrent problem for most of the phase retrieval algorithms. Another drawback is the need to do at least three acquisitions, which depends on the mechanic characteristics of the working microscope.

3.1.2 Phase retrieval by partial differential equations

On this category appears the variational method of **Transport-of-Intensity**, which has been already applied to DIC microscopy by Kou et al [52] and Bostan et al [19]. "*The transport-of-intensity equation (TIE) links the phase image to the variations in the intensity induced by wave propagation along the optical axis*". This allows to formulate a second-order differential equation with a unique solution as follows

$$\frac{\partial I(x,y,z)}{\partial z} = -\frac{\lambda}{2\pi}\nabla_{\perp}\cdot[I(x,y,0)\nabla_{\perp}\phi(x,y)]$$

where $\nabla_{\perp} = (\partial/\partial x, \partial/\partial y)$ denotes the two-dimensional gradient operator in the $x-y$ plane. The algorithm developed in [52] applied an inverse operator to the solution of the differential equation, which introduced noisy artifacts; instead, Bostan in [19] proposed a forward model with a Total Variation (TV) regularizer to deal with the abrupt changes in the phase function. The reconstruction algorithm was designed to produce an equivalent constrained problem with Augmented Lagrangian which was solved using an Alternating Direction Method of Multipliers (ADMM). Although TIE is computationally efficient, it is highly sensitive to noise.

3.1.3 Phase retrieval by functional minimization

The problem of phase estimation has been studied by means of the phase retrieval problem, whose objective is to recover the phase function given the magnitude of its Fourier transform. In the recent review paper by Shechtman et al [78], they state that the Fourier phase-retrieval problem belongs to the following general problem:

$$\min_{x\in\mathbb{C}^N} \sum_{k=1}^{K} \left(y_k - |\langle a_k, x\rangle|^2\right)^2 \tag{3.3}$$

where $x \in \mathbb{C}^N$ is the unknown signal, $y_k \in \mathbb{R}^N$ is the observations vector and $a_k \in \mathbb{R}^N$ denotes the measurements vector.

The first algorithm to solve problem (3.3) was proposed by Gerchberg and Saxton [40] which used an **alternating projections** approach. The projections are done between the real-plane constraint $|x|$ and the Fourier-plane constraint $|X|$. This algorithm was improved after by J.R. Fienup [34] by adding more constraints in terms of nonnegativity and the signal support. As many of iterative-type algorithms for solving non-convex problems, the approximation could only converge to a local minimum.

In [78] it is also mentioned the use of **semidefinite programming** (SDP) to convexificate the phase retrieval problem. SDP is a generalization of linear programming, which enables to specify a semidefinite constraint in addition to a set of linear constraints. The *PhaseLift* algorithm proposed by Candès et al [23] was designed under this approach and their previous work on matrix completion [22]. The idea behind PhaseLift is to uplift the unknown vector by replacing it with a higher dimension matrix, that is, $X = xx^*$, where $\text{rank}(X) = 1$. This means that

$$\begin{aligned} |\langle a_k, x\rangle|^2 &= \text{Tr}(x^* a_k a_k^* x) = \text{Tr}(a_k a_k^* x x^*) \\ &:= \text{Tr}(A_k X) \end{aligned}$$

This converts the problem into a low-rank matrix completion optimization problem where the objective is to find the positive semidefinite matrix X. The restriction of this algorithm is that it increases the dimension of the original problem, which affects the computational time when the input problem is of high dimension.

3.1.4 Phase functional by least-squares minimization

This approach was used in the *Rotational diversity* model proposed by Preza et al in [72]. The objective was to obtain an estimation of the phase functional *"by minimizing the least-squares discrepancy measure between the measured images and the model predictions"* as in (3.2). In order to do so, they used the Conjugate Gradient method, on which the direction of descent was calculated with the Polak-Ribiere formulation, and the steplength parameter was updated with a polynomial-based linesearch strategy. They also used a Tikhonov penalty to deal with the discontinuities at the pixel approximations. One of the drawbacks of this approach is the computational time, since at every iteration is needed to compute the gradient of the functional, which in that case was of the order of $\mathcal{O}(N^4)$; another one is the fact that the Tikhonov penalty does not deal very well to preserve edges and strong jumps in the values of the gradient of the phase.

3.2 Properties of J_0

Before describing the optimization methods implemented to solve problem (3.2), we present the properties of function J_0.

3.2.1 Periodicity, additive invariance, smoothness

Lemma 1 *Let $J_0 : \mathbb{R}^{MP} \to \mathbb{R}$ be defined as in* (3.1)*. Then we have the following:*

(i) ***Periodicity****. There exists $T > 0$ such that J_0 is periodic of period T with respect to each variable, i.e. for any $j \in \chi$, where $\chi = \{1, \ldots, M\} \times \{1, \ldots, P\}$, M and P meaning the size of the acquired image, defining $\boldsymbol{e}_j = (\delta_{j,r})_{r\in\chi} = (0, \ldots, 0, 1, 0, \ldots, 0) \in \mathbb{R}^{MP}$ where $\delta_{j,r}$*

is the Kronecker delta, it holds

$$J_0(\phi + T\boldsymbol{e}_j) = J_0(\phi), \quad \forall\ \phi \in \mathbb{R}^{MP}. \tag{3.4}$$

(ii) ***Additive constant-invariance****.* $J_0(\phi + c\mathbf{1}) = J_0(\phi)$, $\forall\ c \in \mathbb{R}$, *where* $\mathbf{1} \in \mathbb{R}^{MP}$ *is the vector of all ones.*

(iii) ***Smoothness****.* J_0 *is an analytic function on* $\mathbb{R}^{MP}$ *and therefore* $J_0 \in C^\infty(\mathbb{R}^{MP})$.

Proof. (i) Fix $j \in \chi$, $\ell \in \{1,2,3\}$ and consider the exponential in (3.1). Then for all $r \in \chi$

$$\left(e^{-i(\phi+2\pi\lambda_\ell \boldsymbol{e}_j)/\lambda_\ell}\right)_r = \begin{cases} e^{-i\phi_r/\lambda_\ell} & ,\ r \neq j \\ e^{-i[(\phi_j/\lambda_\ell)+2\pi]} = e^{-i\phi_r/\lambda_\ell} & ,\ r = j \end{cases} = (e^{-i\phi/\lambda_\ell})_r, \tag{3.5}$$

where the equality inside the curly bracket is due to the periodicity of the complex exponential. Then, for a fixed $\ell \in \{1,2,3\}$, the expression given in (3.1) without the sum in ℓ is $2\pi\lambda_\ell$ periodic w.r.t. the variable ϕ_j. This means that J_0 is the sum of three periodic functions of variable ϕ_j whose periods are $2\pi\lambda_1$, $2\pi\lambda_2$ and $2\pi\lambda_3$ respectively. By recalling that the sum of two periodic functions is periodic if the ratio of the periods is a rational number, we can conclude that J_0 is periodic, as we have $\frac{\lambda_\ell}{\lambda_{\ell'}}$ rational for all $\ell, \ell' \in \{1,2,3\}$. Without loss of generality, we make this assumption since each R,G,B wavelength value represents a mean value of the wavelengths selected by an optical color bandpass in the actual microscope.

(ii) Set $J_{\ell,k,j}(\phi) = \left|(h_{k,\lambda_\ell} \otimes e^{-i\phi/\lambda_\ell})_j\right|^2 = \left|\sum_{r\in\chi}(h_{k,\lambda_\ell})_r e^{-i(\phi_{j-r})/\lambda_\ell}\right|^2$. If the thesis holds for $J_{\ell,k,j}$, then it holds also for J_0. We have

$$\begin{aligned} J_{\ell,k,j}(\phi + c\mathbf{1}) &= \left|\sum_{r\in\chi}(h_{k,\lambda_\ell})_r e^{-i(\phi_{j-r}+c)/\lambda_\ell}\right|^2 = \left|e^{-ic/\lambda_\ell}\sum_{r\in\chi}(h_{k,\lambda_\ell})_r e^{-i(\phi_{j-r})/\lambda_\ell}\right|^2 \\ &= \left|e^{-ic/\lambda_\ell}\right|^2 \left|\sum_{r\in\chi}(h_{k,\lambda_\ell})_r e^{-i(\phi_{j-r})/\lambda_\ell}\right|^2 = J_{\ell,k,j}(\phi). \end{aligned} \tag{3.6}$$

(iii) If $J_{\ell,k,j}$ is an analytic function on $\mathbb{R}^{MP}$, then J_0 is given by sums and compositions of analytic functions and thus it is itself analytic [53, Propositions 1.6.2 and 1.6.7]. Hence we focus on $J_{\ell,k,j}$. Since $(h_{k,\lambda_\ell})_r \in \mathbb{C}$, it can be expressed in its trigonometric form $(h_{k,\lambda_\ell})_r = \rho_r e^{i\theta_r}$, with $\rho_r \in \mathbb{R}_{\geq 0}$, $\theta_r \in [0, 2\pi)$. Then we can rewrite $J_{\ell,k,j}$ as follows

$$\begin{aligned} J_{\ell,k,j}(\phi) &= \left|\sum_{r\in\chi}\rho_r e^{i[\theta_r - (\phi_{j-r}/\lambda_\ell)]}\right|^2 = \\ &= \left|\sum_{r\in\chi}\rho_r\cos(\theta_r - (\phi_{j-r}/\lambda_\ell)) + i\sum_{r\in\chi}\rho_r\sin(\theta_r - (\phi_{j-r}/\lambda_\ell))\right|^2 = \\ &= \left(\sum_{r\in\chi}\rho_r\cos(\theta_r - (\phi_{j-r}/\lambda_\ell))\right)^2 + \left(\sum_{r\in\chi}\rho_r\sin(\theta_r - (\phi_{j-r}/\lambda_\ell))\right)^2. \end{aligned}$$

We now observe that the function $J_{\ell,k,j}$ contains $\sin(\theta_r - (\phi_{j-r}/\lambda_\ell))$ and $\cos(\theta_r - (\phi_{j-r}/\lambda_\ell))$,

which are both analytic functions with respect to the single variable ϕ_{j-r} and thus also with respect to ϕ, and the square function $(\cdot)^2$, which is also analytic. Since $J_{\ell,k,j}$ is given by sums and compositions of these functions, it is analytic. □

3.2.2 Existence and non-uniqueness

Problem (3.2) admits infinitely many solutions, as stated in the following theorem.

Theorem 1 *J_0 admits at least one global minimum point. Furthermore, if $\psi \in \mathbb{R}^{MP}$ is a global minimizer of J_0, then also $\{\psi + c\mathbf{1} : \ c \in \mathbb{R}\} \cup \{\psi + mT\boldsymbol{e}_j : \ j \in \chi, \ m \in \mathbb{Z}\}$ are global minimizers of J_0.*

Proof. Let $\Omega = [0, T]^{MP} \subset \mathbb{R}^{MP}$. Point (iii) of Lemma 1 ensures that J_0 is continuous on Ω, thus from the extreme value theorem J_0 admits at least one minimum point ψ on Ω. Now let's show that ψ is a global minimizer of J_0 on $\mathbb{R}^{MP}$. By contradiction, assume that there exists $\phi \in \mathbb{R}^{MP} \setminus \Omega$ such that $J_0(\phi) < J_0(\psi)$. Let $I \subset \chi$ be the subset of indices such that $\{\phi_s\}_{s\in I}$ is the set of all components of ϕ which belong to $\mathbb{R} \setminus [0, T]$ and $\{m_s\}_{s\in I} \subset \mathbb{Z} \setminus \{1\}$ is the set of integers such that $\phi_s \in [(m_s - 1)T, m_s T]$. Define $\bar{\phi} = \phi - \sum_{s\in I}(m_s - 1)T\boldsymbol{e}_s \in \Omega$. By periodicity of J_0 w.r.t. the variables ϕ_s, $s \in I$, we obtain

$$J_0(\bar{\phi}) = J_0(\phi) < J_0(\psi). \tag{3.7}$$

Therefore, we have found a point $\bar{\phi} \in \Omega$ such that $J_0(\bar{\phi}) < J_0(\psi)$, where ψ is a minimum point on Ω. This is absurd, hence ψ is a global minimizer for J_0. The second part of the thesis follows from points (i)-(ii) of Lemma 1. □

3.2.3 Gradient of J_0

In order to solve problem (3.2) using any gradient-based optimization method it is necessary to have a compact computation of the gradient of the functional. Here we present the general expression of the gradient for functional (3.1).

Let us introduce the residual image $r_{k,\lambda_\ell} = \left|(h_{k,\lambda_\ell} \otimes e^{-i\phi/\lambda_\ell})\right|^2 - o_{k,\lambda_\ell}$ and fix $s \in \chi$; the partial derivative of J_0 with respect to ϕ_s is given by

$$\frac{\partial J_0(\phi)}{\partial \phi_s} = \sum_{\ell=1}^{3}\sum_{k=1}^{K}\sum_{j\in\chi}\frac{4}{\lambda_\ell}(r_{k,\lambda_\ell})_j \mathrm{Im}\Big\{e^{-i\phi_s/\lambda_\ell}(h_{k,\lambda_\ell})_{j-s}\overline{(h_{k,\lambda_\ell} \otimes e^{-i\phi/\lambda_\ell})_j}\Big\}, \tag{3.8}$$

which can be written in a compact way as

$$\frac{\partial J_0(\phi)}{\partial \phi_s} = \sum_{\ell=1}^{3}\sum_{k=1}^{K}\frac{4}{\lambda_\ell}\mathrm{Im}\Big\{\Big((r_{k,\lambda_\ell}. * (\overline{h_{k,\lambda_\ell}} \otimes e^{i\phi/\lambda_\ell})) \otimes \tilde{h}_{k,\lambda_\ell}\Big)_s e^{-i\phi_s/\lambda_\ell}\Big\}, \tag{3.9}$$

where $\mathrm{Im}(\cdot)$ denotes the imaginary part of a complex number, $h_1 . * h_2$ denotes the componentwise product between two images h_1, h_2 and $(\tilde{h}_{k,\lambda_\ell})_j = (h_{k,\lambda_\ell})_{-j}$ for all $j \in \chi$. Details of the development are found in Appendix B.1.

It is important to remark that the complexity of this gradient computation is of the order of $\mathcal{O}(\mathrm{MP}\log\mathrm{MP})$, which is better to the one previously proposed by Preza in [72] of the order of $\mathcal{O}((\mathrm{MP})^2)$.

3.3 Smooth Regularized DIC Phase Estimation

Theorem 1 asserts that the solution to problem (3.2) is not unique and it may be determined only up to an unknown real constant or to multiples of the period T w.r.t. any variable ϕ_j. Furthermore, since J_0 is periodic, it is a nonconvex function of the phase ϕ, thus it may admit several local minima as well as saddle points. In the light of these considerations, we can conclude that (3.2) is a severely ill-posed problem, which requires regularization in order to impose some a priori knowledge on the unknown phase. In particular, we propose to solve the following regularized optimization problem

$$\min_{\phi\in\mathbb{R}^{MP}} J(\phi) \equiv J_0(\phi) + J_{TV}(\phi), \tag{3.10}$$

where J_0 is the least-squares distance defined in (3.1) and J_{TV} is the smooth total variation functional (also known as hypersurface potential - HS) defined as [1, 11, 25]

$$J_{TV}(\phi) = \mu \sum_{j\in\chi} \sqrt{((\mathcal{D}\phi)_j)_1^2 + ((\mathcal{D}\phi)_j)_2^2 + \delta^2}, \tag{3.11}$$

where $\mu > 0$ is a regularization parameter, the discrete gradient operator $\mathcal{D} : \mathbb{R}^{MP} \longrightarrow \mathbb{R}^{2MP}$ is set through the standard finite difference with periodic boundary conditions

$$(\mathcal{D}\phi)_{j_1,j_2} = \begin{pmatrix} ((\mathcal{D}\phi)_{j_1,j_2})_1 \\ ((\mathcal{D}\phi)_{j_1,j_2})_2 \end{pmatrix} = \begin{pmatrix} \phi_{j_1+1,j_2} - \phi_{j_1,j_2} \\ \phi_{j_1,j_2+1} - \phi_{j_1,j_2} \end{pmatrix}, \ \phi_{M+1,j_2} = \phi_{1,j_2}, \ \phi_{j_1,P+1} = \phi_{j_1,1}$$

and the additional parameter $\delta \geq 0$ plays the role of a threshold for the gradient of the phase, that is, *"it tunes the value of the gradient above which a discontinuity is detected"* [25]. Obviously J_{TV} reduces to the standard TV functional [76] by setting $\delta = 0$. The choice of this kind of regularization term instead of the first-order Tikhonov one used e.g. in [72, 73] lies in the capability of the HS regularizer to behave both as a Tikhonov-like regularization in regions where the gradient assumes small values (w.r.t. δ), and as an edge-preserving regularizer in regions where the gradient is very large, as it happens in the neighborhood of jumps in the values of the phase.

3.3.1 Properties of $J(\phi)$

Problem (3.10) is still a difficult nonconvex optimization problem and, when $\delta = 0$, it is also nondifferentiable. Some properties of the objective function J are now reported.

Constant-invariance and Gradient Lipschitz continuous

Lemma 2 *Let $J : \mathbb{R}^{MP} \to \mathbb{R}$ be defined as in* (3.10) *for $\delta \geq 0$. Then:*

- $J(\phi + c\mathbf{1}) = J(\phi)$, $\forall\ c \in \mathbb{R}$.
- *If $\delta > 0$, then $J \in C^\infty(\mathbb{R}^{MP})$ and ∇J is Lipschitz continuous, namely there exists $L > 0$ such that*

$$\|\nabla J(\phi) - \nabla J(\psi)\|_2 \leq L\|\phi - \psi\|_2, \quad \forall \phi, \psi \in \mathbb{R}^{MP}. \tag{3.12}$$

Proof. (i) We have already proved in point (ii) of Lemma 1 that the property holds for J_0. Since it is immediate to check that $(\mathcal{D}(\phi + c\mathbf{1}))_{j_1,j_2} = (\mathcal{D}\phi)_{j_1,j_2}$, the property is true also for J_{TV} and thus for J.
(ii) Point (iii) of Lemma 1 states that $J_0 \in C^\infty(\mathbb{R}^{MP})$ and the same property holds for J_{TV} when $\delta > 0$, hence J is the sum of two $C^\infty(\mathbb{R}^{MP})$ functions.
It is known that ∇J_{TV} is $L_{TV}-$Lipschitz continuous with $L_{TV} = 8\mu/\delta^2$ [30]. We prove that also ∇J_0 is Lipschitz continuous and defined in equation (3.8). As concerns the entries of the Hessian $\nabla^2 J_0$, the second derivative w.r.t. ϕ_s, ϕ_t $(s, t \in \chi)$ is given by (see Appendix B.2)

$$\frac{\partial^2 J_0(\phi)}{\partial\phi_t\partial\phi_s} = 4\sum_{\ell=1}^{3}\sum_{k=1}^{K}\sum_{j\in\chi}\frac{2}{\lambda_\ell^2}\mathrm{Im}\{\vartheta_s\}\,\mathrm{Im}\{\vartheta_t\} + \frac{(r_{k,\lambda_\ell})_j}{\lambda_\ell^2}\mathbb{R}e\Big\{e^{i(\phi_t-\phi_s)/\lambda_\ell}(h_{k,\lambda_\ell})_{j-s}\overline{(h_{k,\lambda_\ell})_{j-t}} - \delta_{s,t}\vartheta_s\Big\}, \tag{3.13}$$

where $\vartheta_p = e^{-i\phi_p/\lambda_\ell}(h_{k,\lambda_\ell})_{j-p}\overline{(h_{k,\lambda_\ell} \otimes e^{-i\phi/\lambda_\ell})_j}$ $(p \in \chi)$, $\mathbb{R}e(\cdot)$ denotes the real part of a complex number and $\delta_{s,t}$ is the Kronecker delta. By using the triangle inequality and the fact that $|e^{-i\phi_r/\lambda_\ell}| = 1$, the following inequality hold:

$$|\vartheta_p| \leq |(h_{k,\lambda_\ell})_{j-p}|\sum_{r\in\chi}|(h_{k,\lambda_\ell})_r|. \tag{3.14}$$

By applying again the triangle inequality, the fact that $|e^{-i\phi_r/\lambda_\ell}| = 1$, $|\mathrm{Im}(z)| \leq |z|$ and $|\mathbb{R}e(z)| \leq |z|$ for any $z \in \mathbb{C}$ and inequality (3.14) to (3.13), we obtain the following bound on the second derivative of J_0:

$$\left|\frac{\partial^2 J_0(\phi)}{\partial\phi_t\partial\phi_s}\right| \leq 4\sum_{\ell=1}^{3}\sum_{k=1}^{K}\sum_{j\in\chi}\frac{2}{\lambda_\ell^2}|(h_{k,\lambda_\ell})_{j-s}||(h_{k,\lambda_\ell})_{j-t}|\left(\sum_{r\in\chi}|(h_{k,\lambda_\ell})_r|\right)^2 + \frac{|(r_{k,\lambda_\ell})_j|}{\lambda_\ell^2}\left\{|(h_{k,\lambda_\ell})_{j-s}||(h_{k,\lambda_\ell})_{j-t}| + |(h_{k,\lambda_\ell})_{j-s}|\sum_{r\in\chi}|(h_{k,\lambda_\ell})_r|\right\}. \tag{3.15}$$

Set $H_{k,\ell} = \sum_{r\in\chi} |(h_{k,\lambda_\ell})_r|$. Taking the sum of (3.15) over $s \in \chi$ and picking the maximum over $t \in \chi$, a bound on the $\ell_\infty-$norm of the Hessian $\nabla^2 J_0$ is obtained:

$$\begin{aligned}\|\nabla^2 J_0(\phi)\|_\infty &= \max_{t\in\chi} \sum_{s\in\chi} \left| \frac{\partial^2 J_0(\phi)}{\partial\phi_t \partial\phi_s} \right| \\ &\leq 4 \sum_{\ell=1}^{3} \sum_{k=1}^{K} \sum_{j\in\chi} \frac{H_{k,\ell}}{\lambda_\ell^2} \left\{ 2 \max_{t\in\chi} |(h_{k,\lambda_\ell})_{j-t}| H_{k,\ell}^2 + |(r_{k,\lambda_\ell})_j| \left[\max_{t\in\chi} |(h_{k,\lambda_\ell})_{j-t}| + H_{k,\ell} \right] \right\} \\ &= L_0, \quad \forall\, \phi \in \mathbb{R}^{MP}.\end{aligned}$$

From relation $\|A\|_2 \leq \sqrt{\|A\|_1 \|A\|_\infty}$ and the fact that $\|\nabla^2 J(\phi)\|_1 = \|\nabla^2 J(\phi)\|_\infty$ ($\nabla^2 J_0(\phi)$ is a symmetric matrix), it follows that $\|\nabla^2 J_0(\phi)\|_2 \leq L_0$ for all $\phi \in \mathbb{R}^{MP}$. Fix $\phi, \psi \in \mathbb{R}^{MP}$. By the mean value theorem for vector-valued functions, we have

$$\|\nabla J_0(\phi) - \nabla J_0(\psi)\|_2 \leq \sup_{\theta\in(0,1)} \|\nabla^2 J_0(\psi + \theta(\phi - \psi))\|_2 \|\phi - \psi\|_2 \leq L_0 \|\phi - \psi\|_2. \tag{3.16}$$

Then ∇J_0 is L_0-Lipschitz continuous and consequently also ∇J is Lipschitz continuous with constant $L = L_0 + L_{TV}$. □

Remark: *bound L_0 is pessimistic and it is not explicitly used in the algorithm implementation; because of this, it does not need to be sharp.*

Existence and uniqueness of a solution

Point (i) of Lemma 2 makes clear that, if a solution to problem (3.10) exists, then it is not unique and it can be determined only up to a real constant. This is a common feature shared with the unregularized problem (3.2). However, unlike in (3.2), the objective function J is not periodic and, in addition, none of the two terms J_0 and J_{TV} are coercive, therefore we can not prove the existence of a minimum point of J neither as in Theorem 1 nor by coercivity. A specific proof of existence of the solution for problem (3.10) is now presented.

Theorem 2 *The objective function J admits at least one global minimum point. Furthermore, if $\psi \in \mathbb{R}^{MP}$ is a global minimizer of J, then also $\{\psi + c\mathbf{1} :\ c \in \mathbb{R}\}$ are global minimizers of J.*

Proof. Let $S = \{\phi \in \mathbb{R}^{MP} :\ \phi = c\mathbf{1},\ c \in \mathbb{R}\}$ be the line in $\mathbb{R}^{MP}$ of all constant images and Π any hyperplane intersecting S in one point ϕ_S, i.e.

$$\Pi = \{\phi \in \mathbb{R}^{MP} : \sum_{r\in\chi} a_r \phi_r + b = 0\},\ \sum_{r\in\chi} a_r \neq 0,\ b \in \mathbb{R}. \tag{3.17}$$

Thanks to part (i) of Lemma 2, for any $\phi \in \mathbb{R}^{MP}$ the point $\phi_\Pi = \phi - \left(\frac{\sum_r a_r \phi_r + b}{\sum_r a_r} \right) \mathbf{1} \in \Pi$ is such that $J(\phi_\Pi) = J(\phi)$. Consequently, if ψ is a minimum point of J on Π, then it is also a minimum point on $\mathbb{R}^{MP}$, because $J(\psi) \leq J(\phi_\Pi) = J(\phi)$ for all $\phi \in \mathbb{R}^{MP}$. Hence we restrict the search of the minimum point on Π and we denote with $J|_\Pi$ the restriction of J to Π. Since $S = \arg\min_{\phi\in\mathbb{R}^{MP}} J_{TV}(\phi)$ and Π intersects S only in ϕ_S, J_{TV} is a convex function with a

unique minimum point on Π, which implies that J_{TV} is coercive on Π. Furthermore, being J_0 periodic and continuous, it is a bounded function on Π. Then $J|_\Pi$ is the sum of a coercive term and a bounded one, therefore it is itself coercive. This allows to conclude that J admits a minimum point on Π and thus also on $\mathbb{R}^{MP}$. The second part of the thesis follows from Lemma 2, part (i). □

Note that the above proof of existence holds also for the regularized DIC problem proposed in [72, 73], in which the Tikhonov-like regularizer used instead of the TV functional is also noncoercive.

3.4 Optimization approach for phase estimation in DIC microscopy

In previous works [72, 73, 74], the problem of DIC phase reconstruction had been addressed with the nonlinear conjugate gradient method [66]. However, as it is explained in Subsection 3.5.1, these methods require in practice several evaluations of the objective function and possibly its gradient in order to compute the linesearch parameter. What we propose instead is to tackle problem (3.10) with a gradient descent algorithm in the differentiable case ($\delta > 0$) and a proximal-gradient method in the nondifferentiable case ($\delta = 0$). The key ingredients of both methods are the use of an Armijo linesearch at each iteration, which ensures convergence to a stationary point of problem (3.10), and a clever adaptive choice of the steplength in order to improve the speed of convergence.

For sake of simplicity, from now on we assume that each monochromatic image is treated as a vector in $\mathbb{R}^N$ (being $N = MP$) obtained by a lexicographic reordering of its pixels.

3.4.1 LMSD: Gradient method

In this subsection we describe the first proposed algorithm to address problem (3.10) when $\delta > 0$. In this case the objective function is differentiable and we exploit the limited memory steepest descent (LMSD) method proposed by Fletcher [35] and outlined in Algorithm 1.

The LMSD method is a standard gradient method equipped with a monotone Armijo linesearch and variable steplengths approximating the inverse of some eigenvalues of the Hessian matrix $\nabla^2 J(\phi^{(n)})$ in order to improve the convergence speed. Unlike the classical Barzilai–Borwein (BB) rules [8] and its generalizations (see e.g. [32, 33, 87]) which tries to approximate $(\nabla^2 J(\phi^{(n)}))^{-1}$ with a constant diagonal matrix, the idea proposed by Fletcher for quadratic objective functions is based on a Lanczos iterative process applied to the Hessian matrix of the objective function. Some algebra shows that this can be practically performed without the explicit knowledge of the Hessian itself but exploiting only a set of back gradients and steplengths (see steps 6–10 of Algorithm 1). Generalization to nonquadratic functions can

be obtained by computing the eigenvalues of the matrix $\widetilde{\Phi}$ in step 10 instead of Φ (we remark that for quadratic J the two matrices coincide).

Some practical issues have to be addressed in the implementation of Algorithm 1:

- The first loop (step 1 to 5) build a matrix

$$G = \left[\nabla J(\phi^{(n-m)}) \quad \nabla J(\phi^{(n-m+1)}) \dots \nabla J(\phi^{(n-1)})\right]$$

  of size $MP \times m$. The initial values for the first m steplengths can be provided by the user (e.g. by computing the BB ones) or can be chosen with the same approach described in steps 6–10 but with smaller matrices. For example, one can fix $\alpha_0^{(0)}$, compute $G = \nabla J(\phi^{(0)})$ and use steps 6–10 to compute $\alpha_1^{(0)}$. At this point, defining $G = [\nabla J(\phi^{(0)}) \quad \nabla J(\phi^{(1)})]$ one can compute $\alpha_2^{(0)}$ and $\alpha_3^{(0)}$ and repeat the procedure until a whole set of m back gradients is available.

- The same procedure can be adopted when step 10 provides only $m' < m$ positive eigenvalues. In this case, all columns of G are discarded, G becomes the empty matrix and the algorithm proceeds with m' instead of m until a whole set of m back gradients is computed. If $m' = 0$, a set of m "safeguard" steplengths, corresponding to the last set of m positive steplengths values provided by step 10, is exploited for the next m iterations.

- If $G^T G$ in step 7 is not positive definite, then the oldest gradient of G is discarded and a new matrix $G^T G$ is computed. This step is repeated until $G^T G$ becomes positive definite.

- The stopping criterion can be chosen by the user and be related to the decrease of J or to the distance between two successive iterates. In our tests we decided to arrest the iterations when the norm of the gradient ∇J goes below a given threshold κ:

$$\|\nabla J(\phi^{(n)})\| \leq \kappa. \tag{3.18}$$

Concerning the computational costs of LMSD, the heaviest tasks at each iteration are the computation of $\nabla J(\phi^{(n)})$ at step 1 and $J(\phi^{(n)} - \alpha_n \nabla J(\phi^{(n)}))$ at step 2. Considering step 1, we focus on ∇J_0. As it is written in (3.8), due to the product between $e^{-i\phi_s/\lambda_\ell}$ and $(h_{k,\lambda_\ell})_{j-s}$, ∇J_0 can be performed with $\mathcal{O}(N^2)$ complexity; this is how the gradient is computed in [72]. However, if we take the sum over j of the residuals into the argument of $\mathrm{Im}(\cdot)$, then we can conveniently rewrite (3.8) as

$$\frac{\partial J_0(\phi)}{\partial \phi_s} = \sum_{\ell=1}^{3} \sum_{k=1}^{K} \frac{4}{\lambda_\ell} \mathrm{Im}\left\{ \left((r_{k,\lambda_\ell} . * (\overline{h_{k,\lambda_\ell}} \otimes e^{i\phi/\lambda_\ell})) \otimes \tilde{h}_{k,\lambda_\ell} \right)_s e^{-i\phi_s/\lambda_\ell} \right\}, \tag{3.19}$$

where $h_1 . * h_2$ denotes the componentwise product between two images h_1, h_2 and $(\tilde{h}_{k,\lambda_\ell})_j = (h_{k,\lambda_\ell})_{-j}$ for all $j \in \chi$. Then the heaviest operations in (3.19) are the two convolutions which, thanks to the assumption of periodic boundary conditions, can be performed with a FFT/IFFT pair ($\mathcal{O}(N \log N)$) complexity). Hence, since ∇J_{TV} has $\mathcal{O}(N)$ complexity, we can conclude that step 1 has an overall complexity of $\mathcal{O}(N \log N)$. Similarly, the function at step

2 is computed with complexity $\mathcal{O}(N \log N)$, due to the presence of one convolution inside the triple sum in (3.1).

From a practical point of view, we have already shown that the LMSD method is an effective tool for DIC imaging, especially if compared to more standard gradient methods equipped with the BB rules [9]. From a mathematical point of view, one can prove, in the same way as in [14], that every limit point of the sequence generated by Algorithm 1 is a stationary point for problem (3.10). In addition, the convergence of Algorithm 1 can be asserted whenever the objective function J satisfies the Kurdyka–Łojasiewicz (KL) property [57, 54] at each point of its domain.

More precisely, as shown in a number of recent papers [5, 37, 15], one can prove the convergence of a sequence $\{\phi^{(n)}\}_{n\in\mathbb{N}}$ to a limit point (if any exists) which is stationary for J if the following three conditions are satisfied:

$$
\begin{aligned}
&(H1) \quad \exists\, a > 0 :\ J(\phi^{(n+1)}) + a\|\phi^{(n+1)} - \phi^{(n)}\|^2 \leq J(\phi^{(n)}) \\
&(H2) \quad \exists\, b > 0 :\ \|\nabla J(\phi^{(n+1)})\| \leq b\|\phi^{(n+1)} - \phi^{(n)}\| \\
&(H3) \quad J \text{ satisfies the KL property.}
\end{aligned}
$$

This scheme applies to the LMSD method. First of all, condition $(H3)$ is satisfied for the DIC functional defined in (3.10). Indeed J_0 is an analytic function (Lemma 1, part (iii)) and J_{TV} is a semialgebraic function, which means that its graph is defined by a finite sequence of polynomial equations and inequalities (see [86] for a definition). Hence J is the sum of an analytic function and a semialgebraic one and for this reason it satisfies the KL property on $\mathbb{R}^N$ (see [86, p. 1769] and references therein). Conditions $(H1) - (H2)$ follows from step 2 and 3, combined with the fact that ∇J is Lipschitz continuous (Lemma 2, part (ii)), provided that the sequence of steplengths $\alpha_n^{(0)}$ defined at step 11 is bounded from above. Therefore we can state the following result:

Theorem 3 *Let J be defined as in* (3.10)*, $\{\phi^{(n)}\}_{n\in\mathbb{N}}$ the sequence generated by Algorithm 1 and assume that $\alpha_n^{(0)} \leq \alpha_{\max}$, where $\alpha_{\max} > 0$. If ϕ^* is a limit point of $\{\phi^{(n)}\}_{n\in\mathbb{N}}$, then ϕ^* is a stationary point of J and $\phi^{(n)}$ converges to ϕ^*.*

Algorithm 1 Limited memory steepest descent (LMSD) method

Choose $\rho, \omega \in (0,1)$, $m \in \mathbb{N}_{>0}$, $\alpha_0^{(0)}, \ldots, \alpha_{m-1}^{(0)} > 0$, $\phi^{(0)} \in \mathbb{R}^N$ and set $n = 0$.
While True

For $l = 1, \ldots, m$

1. Define $G(:, l) = \nabla J(\phi^{(n)})$.
2. Compute the smallest non-negative integer i_n such that $\alpha_n = \alpha_n^{(0)} \rho^{i_n}$ satisfies

$$J(\phi^{(n)} - \alpha_n \nabla J(\phi^{(n)})) \leq J(\phi^{(n)}) - \omega \alpha_n \|\nabla J(\phi^{(n)})\|^2. \tag{3.20}$$

3. Compute $\phi^{(n+1)} = \phi^{(n)} - \alpha_n \nabla J(\phi^{(n)})$.

   If "Stopping Criterion" is satisfied

   4. Return

   Else

   5. Set $n = n + 1$.

   EndIf

EndFor

6. Define the $(m+1) \times m$ matrix $\Gamma = \begin{bmatrix} \alpha_{n-m}^{-1} & & \\ -\alpha_{n-m}^{-1} & \ddots & \\ & \ddots & \alpha_{n-1}^{-1} \\ & & -\alpha_{n-1}^{-1} \end{bmatrix}$.
7. Compute the Cholesky factorization $R^T R$ of the $m \times m$ matrix $G^T G$.
8. Solve the linear system $R^T r = G^T \nabla J(\phi^{(n)})$.
9. Define the $m \times m$ matrix $\Phi = [R, r] \Gamma R^{-1}$.
10. Compute the eigenvalues $\theta_1, \ldots, \theta_m$ of the symmetric and tridiagonal approximation $\widetilde{\Phi}$ of Φ defined as

$$\widetilde{\Phi} = \text{diag}(\Phi) + \text{tril}(\Phi, -1) + \text{tril}(\Phi, -1)^T,$$

    being $\text{diag}(\cdot)$ and $\text{tril}(\cdot, -1)$ the diagonal and the strictly lower triangular parts of a matrix.
11. Define $\alpha_{n+i-1}^{(0)} = 1/\theta_i$, $i = 1, \ldots, m$.

EndWhile

Proof. We start by proving condition $(H1)$. Step 3 of Algorithm 1 can be rewritten in the following way:

$$-\alpha_n \nabla J(\phi^{(n)}) = \phi^{(n+1)} - \phi^{(n)}$$

from which we have

$$\alpha_n \|\nabla J(\phi^{(n)})\|^2 = \frac{1}{\alpha_n} \|\phi^{(n+1)} - \phi^{(n)}\|^2. \tag{3.21}$$

By substituting (3.21) in step 2 and since $\alpha_n \leq \alpha_n^{(0)} \leq \alpha_{\max}$, we obtain

$$J(\phi^{(n+1)}) \leq J(\phi^{(n)}) - \frac{\omega}{\alpha_n}\|\phi^{(n+1)} - \phi^{(n)}\|^2 \leq J(\phi^{(n)}) - \frac{\omega}{\alpha_{\max}}\|\phi^{(n+1)} - \phi^{(n)}\|^2. \tag{3.22}$$

Then $(H1)$ holds with $a = \omega/\alpha_{\max}$. Regarding condition $(H2)$, we can rewrite again step 3 as:

$$\nabla J(\phi^{(n)}) = \frac{1}{\alpha_n}(\phi^{(n)} - \phi^{(n+1)}). \tag{3.23}$$

Recall that the Lipschitz continuity of ∇J implies that there is $\alpha_{\min} > 0$ such that the linesearch parameter $\alpha_n \geq \alpha_{\min}$ (see [17, Proposition 4.2] for a proof). Then

$$\begin{aligned}\|\nabla J(\phi^{(n+1)})\| &\leq \|\nabla J(\phi^{(n+1)}) - \nabla J(\phi^{(n)})\| + \|\nabla J(\phi^{(n)})\| \\ &\leq L\|\phi^{(n+1)} - \phi^{(n)}\| + \frac{1}{\alpha_n}\|\phi^{(n+1)} - \phi^{(n)}\| \\ &\leq \left(L + \frac{1}{\alpha_{\min}}\right)\|\phi^{(n+1)} - \phi^{(n)}\|.\end{aligned}$$

This concludes the proof of $(H2)$ with $b = L + 1/\alpha_{\min}$. The thesis follows from [5, Theorem 2.9]. □

3.4.2 ILA: Proximal-Gradient method

We now turn to the algorithm we used to address the nonsmooth case when $\delta = 0$. In particular, we considered a simplified version of a recently proposed proximal-gradient method called VMILA (Variable Metric Inexact Linesearch Algorithm) [17]. In its general form, this method exploits a variable metric in the (possibly inexact) computation of the proximal point at each iteration and a backtracking loop to satisfy an Armijo–like inequality. Effective variable metrics can be designed for specific objective functions by exploiting suitable decompositions of the gradient of the smooth part of the objective function itself [14, 56, 16, 13]. However, since in the DIC problem the gradient of J_0 does not lead to a natural decomposition in the required form, in our tests we used the standard Euclidean distance (we will denote with ILA this simplified version of VMILA). The main steps of ILA are detailed in Algorithm 2.

At each iteration n, given the point $\phi^{(n)} \in \mathbb{R}^N$ and the parameters $\alpha_n > 0$, $\gamma \in [0, 1]$, we define the function

$$h_\gamma^{(n)}(\phi) = \nabla J_0(\phi^{(n)})^T(\phi - \phi^{(n)}) + \frac{\gamma}{2\alpha_n}\|\phi - \phi^{(n)}\|^2 + J_{TV}(\phi) - J_{TV}(\phi^{(n)}). \tag{3.24}$$

We observe that $h_\gamma^{(n)}$ is strongly convex for any $\gamma \in (0, 1]$. By setting $h^{(n)} = h_1^{(n)}$ and $z^{(n)} = \phi^{(n)} - \alpha_n \nabla J_0(\phi^{(n)})$, we define the unique proximal point

$$\psi^{(n)} := \mathrm{prox}_{\alpha_n J_{TV}}(z^{(n)}) = \arg\min_{\phi \in \mathbb{R}^N} h^{(n)}(\phi). \tag{3.25}$$

In step 2 of Algorithm 2, an approximation $\tilde{\psi}^{(n)}$ of the proximal point $\psi^{(n)}$ is defined by means of condition (3.29). Such a point can be practically computed by remarking that J_{TV} can be written as

$$J_{TV}(\phi) = g(\mathcal{D}\phi), \qquad g(t) = \mu \sum_{j=1}^{N} \left\| \begin{pmatrix} t_{2j-1} \\ t_{2j} \end{pmatrix} \right\|, \qquad t \in \mathbb{R}^{2N}.$$

Then considering the dual problem of (3.25)

$$\max_{v \in \mathbb{R}^{2N}} \Gamma^{(n)}(v), \tag{3.26}$$

the dual function $\Gamma^{(n)}$ has the following form

$$\Gamma^{(n)}(v) = -\frac{\|\alpha_n \mathcal{D}^T v - z^{(n)}\|^2}{2\alpha_n} - g^*(v) - J_{TV}(\phi^{(n)}) - \frac{\alpha_n}{2}\|\nabla J_0(\phi^{(n)})\|^2 + \frac{\|z^{(n)}\|^2}{2\alpha_n} \tag{3.27}$$

where g^* is the convex conjugate of g, namely the indicator function of the set $\left(B^2_{0,\mu}\right)^N$, being $B^2_{0,\mu} \subset \mathbb{R}^2$ the 2-dimensional Euclidean ball centered in 0 with radius μ.

Condition (3.29) is fulfilled by any point $\tilde{\psi}^{(n)} = z^{(n)} - \alpha_n A^T v$ with $v \in \mathbb{R}^{2N}$ satisfying [17]

$$h^{(n)}(\tilde{\psi}^{(n)}) \leq \eta \Gamma^{(n)}(v), \qquad \eta = 1/(1+\tau). \tag{3.28}$$

Such a point can be found by applying an iterative method to problem (3.26) and using (3.28) as stopping criterion.

Similarly to LMSD, any limit point of the sequence generated by ILA is stationary for problem (3.10) [17, Theorem 4.1] and, under the assumption that a limit point exists, the convergence of ILA to such a point holds when J satisfies the Kurdyka–Łojasiewicz property, the gradient of the smooth part ∇J_0 is Lipschitz continuous and the proximal point $\tilde{\psi}^{(n)}$ is computed exactly [15]. Whether and when ILA converges when the proximal point is computed inexactly is still an open problem, therefore all we can say for Algorithm 2 applied to the DIC problem is that all its limit points are stationary.

3.4.3 Nonlinear conjugate gradient methods

We compare the performances of LMSD and ILA with several nonlinear conjugate gradient methods, including some standard CG methods [66, 36] and the heuristic CG method previously used for DIC problems [74, 72]. The general scheme for a CG method is recalled in Algorithm 3 and some classical choices for the parameter β_{n+1} are shown in Table 3.1, namely the Fletcher-Reeves (FR), Polak-Ribière (PR), PR with nonnegative values (PR^+) and PR constrained by the FR values (FR-PR) strategies [41].

Algorithm 2 Inexact Linesearch based Algorithm (ILA)

Choose $0 < \alpha_{\min} \leq \alpha_{\max}$, $\rho, \omega \in (0,1)$, $\gamma \in [0,1]$, $\tau > 0$, $\phi^{(0)} \in \mathbb{R}^N$ and set $n = 0$.
While True

1. Set $\alpha_n = \max\left\{\min\left\{\alpha_n^{(0)}, \alpha_{\max}\right\}, \alpha_{\min}\right\}$, where $\alpha_n^{(0)}$ is chosen as in Algorithm 1.

2. Let $h_\gamma^{(n)}$, $h^{(n)}$ and $\psi^{(n)}$ be defined as in (3.24)-(3.25). Compute $\tilde{\psi}^{(n)} \in \mathbb{R}^N$ and $\epsilon_n \geq 0$ such that
$$h^{(n)}(\tilde{\psi}^{(n)}) - h^{(n)}(\psi^{(n)}) \leq \epsilon_n \quad ; \quad \epsilon_n \leq -\tau h_\gamma^{(n)}(\tilde{\psi}^{(n)}). \tag{3.29}$$

3. Set $d^{(n)} = \tilde{\psi}^{(n)} - \phi^{(n)}$.

4. Compute the smallest non-negative integer i_n such that $\lambda_n = \rho^{i_n}$ satisfies
$$J(\phi^{(n)} + \lambda_n d^{(n)}) \leq J(\phi^{(n)}) + \omega \lambda_n h_\gamma^{(n)}(\tilde{\psi}^{(n)}). \tag{3.30}$$

5. Compute the new point as $\phi^{(n+1)} = \phi^{(n)} + \lambda_n d^{(n)}$.

   If "Stopping Criterion" is satisfied

   6. Return

   Else

   7. Set $n = n + 1$.

   EndIf

EndWhile

In order to ensure the global convergence of the FR and FR-PR methods, the steplength parameter α_n in step 1 must comply with the strong Wolfe conditions [41, 66]

$$\begin{aligned} J(\phi^{(n)} + \alpha_n p^{(n)}) &\leq J(\phi^{(n)}) + c_1 \alpha_n \nabla J(\phi^{(n)})^T p^{(n)} \\ |\nabla J(\phi^{(n)} + \alpha_n p^{(n)})^T p^{(n)}| &\leq c_2 |\nabla J(\phi^{(n)})^T p^{(n)}| \end{aligned} \tag{3.31}$$

where $0 < c_1 < c_2 < \frac{1}{2}$. Concerning the PR methods, one can prove convergence if β_{n+1} is chosen according to the PR$^+$ rule and α_n satisfies both (3.31) and the following additional condition [41, 66]

$$\nabla J(\phi^{(n)})^T p^{(n)} \leq -c_3 \|\nabla J(\phi^{(n)})\|^2, \qquad 0 < c_3 \leq 1. \tag{3.32}$$

Algorithm 3 Conjugate gradient (CG) method

Choose $\phi^{(0)} \in \mathbb{R}^N$ and set $n = 0$, $p^{(0)} = -\nabla J(\phi^{(0)})$.
While True

1. Compute α_n and set $\phi^{(n+1)} = \phi^{(n)} + \alpha_n p^{(n)}$.
2. Choose the scalar parameter β_{n+1} according to the CG strategy used.
3. Define $p^{(n+1)} = -\nabla J(\phi^{(n+1)}) + \beta_{n+1} p^{(n)}$.

   If "Stopping Criterion" is satisfied

   4. Return

   Else

   5. Set $n = n + 1$.

   EndIf

EndWhile

CG algorithm	β_{n+1}
FR	$\beta_{n+1}^{\mathrm{FR}} = \dfrac{\nabla J(\phi^{(n+1)})^T \nabla J(\phi^{(n+1)})}{\nabla J(\phi^{(n)})^T \nabla J(\phi^{(n)})}$
PR	$\beta_{n+1}^{\mathrm{PR}} = \dfrac{\nabla J(\phi^{(n+1)})^T (\nabla J(\phi^{(n+1)}) - \nabla J(\phi^{(n)}))}{\nabla J(\phi^{(n)})^T \nabla J(\phi^{(n)})}$
PR$^+$	$\beta_{n+1}^{\mathrm{PR}^+} = \max(\beta_{n+1}^{\mathrm{PR}}, 0)$
FR-PR	$\beta_{n+1}^{\mathrm{FR-PR}} = \begin{cases} \beta_{n+1}^{\mathrm{PR}} & \text{if } \lvert\beta_{n+1}^{\mathrm{PR}}\rvert \le \beta_{n+1}^{\mathrm{FR}} \\ \beta_{n+1}^{\mathrm{FR}} & \text{otherwise} \end{cases}$

Table 3.1: Choice of the parameter β_{n+1} in CG methods. From top to bottom: Fletcher-Reeves (FR), Polak-Ribière (PR), Polak-Ribière with nonnegative β_{n+1} (PR$^+$), Polak-Ribière constrained by the FR method (FR-PR).

For a practical implementation of a backtracking method to satisfy (3.31) see e.g. [66, Section 3.5], while for the addition of condition (3.32) see [41, Section 6]. In Section 3.5, the CG methods equipped with the FR, FR-PR, PR$^+$ rules for the parameter β_{n+1}, together with conditions (3.31) for the linesearch parameter α_n, will be denominated FR-SW, FR-PR-SW and PR$^+$-SW respectively, where SW stands for Strong Wolfe conditions.

Since in the DIC problem the evaluation of the gradient ∇J is computational demanding and its nonlinearity w.r.t. α requires a new computation for each step of the backtracking loop, in [74, 72] a heuristic version of the FR and PR methods is used exploiting a linesearch based on a polynomial approximation method. The resulting scheme for the choice of α_n is detailed in Algorithm 4, even if we recognize that our routines might differ from those used in [74, 72] due to the lack of several details crucial for reproducing their practical

implementation. As we will see in the next Section, this linesearch is quite sensitive to the choice of the parameter t. Moreover, since the strong Wolfe conditions are not imposed, there is no guarantee that the FR or PR methods endowed with this choice for α_n converges, nor that $p^{(n+1)}$ is a descent direction for all n. In the following, the CG methods equipped with the FR and PR rule, together with the linesearch described in Algorithm 4, will be indicated as FR-PA and PR-PA respectively, where PA stands for polynomial approximation.

Algorithm 4 Linesearch based on polynomial approximation

Let $\psi(\alpha) := J(\phi^{(n)} + \alpha p^{(n)})$ and set $t > 0$, $a = 0$, $b = t$.
Compute $\psi(a)$ and $\psi(b)$.

1. Find a point $c \in [a, b]$ such that $\psi(a) > \psi(c) < \psi(b)$ as follows
   If $\psi(b) < \psi(a)$

   Set $c = 2b$ and compute $\psi(c)$.

   While $\psi(c) \leq \psi(b)$

   Set $a = b$, $b = c$, $c = 2c$ and compute $\psi(c)$.

   EndWhile

   Else

   Set $c = \frac{b}{2}$ and compute $\psi(c)$.

   While $\psi(c) \geq \psi(a)$

   Set $b = c$, $c = \frac{c}{2}$ and compute $\psi(c)$.

   EndWhile

   EndIf

2. Compute α_n as the minimum point of the parabola interpolating the points $(a, \psi(a)), (b, \psi(b)), (c, \psi(c))$.

3.5 Numerical experiments

In this section we test the effectiveness of the algorithms previously described in some synthetic problems. All the numerical results have been obtained on a PC equipped with an INTEL Core i7 processor 2.60GHz with 8GB of RAM running Matlab R2013a with its standard settings. For each test we will report the number of function evaluations, the number of gradient evaluations and the computational time needed by each algorithm to provide the reconstructed phase. With this information the reader should be able to estimate the complexity of the different approaches independently of the environment in which the algorithms are implemented and run. The LMSD and ILA routines for the DIC problem together with an illustrative example can be downloaded

at the webpage http://www.oasis.unimore.it/site/home/software.html.

3.5.1 Comparison with state–of–the–art methods

Since in the DIC problem the evaluation of the gradient ∇J is computational demanding and its nonlinearity w.r.t. α requires a new computation for each step of the backtracking loop, in [74, 72] a heuristic version of a nonlinear conjugate gradient (CG) is used exploiting a gradient–free linesearch based on a polynomial approximation method. Although this formulation has practical advantages, the resulting scheme is not guaranteed to converge, and in our tests we experienced very different behaviours w.r.t. to the choice of some initial parameters of the linesearch procedure. For this reason, we also implemented several standard CG methods [66, 36], namely the Fletcher–Reeves (FR), Polak–Ribière (PR), PR with nonnegative values (PR^+) and PR constrained by the FR values (FR–PR) strategies [41]. For these algorithms, the global convergence is ensured by computing the steplength parameter by means of the strong Wolfe conditions [66, 41].

The evaluations of the optimization methods have been carried out on two phantom objects (see Figure 3.1), which have been computed by using the formula for the phase difference between two waves travelling through two different media

$$\phi_s = 2\pi(n_1 - n_2)t_s, \tag{3.33}$$

where n_1 and n_2 are the refractive indices of the object structure and the surrounding medium, respectively, and t_s is the thickness of the object at pixel $s \in \chi$. The first phantom, denominated "cone" and reported at the top row of Figure 3.1, is a 64×64 phase function representing a truncated cone of radius $r = 3.2$ μm with $n_1 = 1.33$, $n_2 = 1$ and maximum value $\phi_{\max} = 1.57$ rad attained at the cone vertex. The "cross" phantom, shown at the bottom row of Figure 3.1, is another 64×64 phase function of two crossing bars, each one of width 5 μm, measuring 0.114 rad inside the bars and 0 in the background. For both simulations, the DIC microscope parameters were set as follows:

- shear: $2\Delta x = 0.6$ μm;
- bias: $2\Delta\theta = \pi/2$ rad;
- numerical aperture of the objective: NA $= 0.9$.

For each phantom, a dataset consisting of $K = 2$ polychromatic DIC images acquired at shear angles $\tau_1 = -\pi/4$ rad and $\tau_2 = \pi/4$ rad was created, as in model (2.14), by convolving the true phase function with the accordingly rotated DIC PSFs and then by corrupting the result with white Gaussian noise at different values of the signal–to–noise ratio

$$\text{SNR} = 10 \log_{10} \left(\frac{\overline{\phi^*}}{\sigma} \right) \tag{3.34}$$

where $\overline{\phi^*}$ is the mean value of the true object and σ is the standard deviation of noise. The

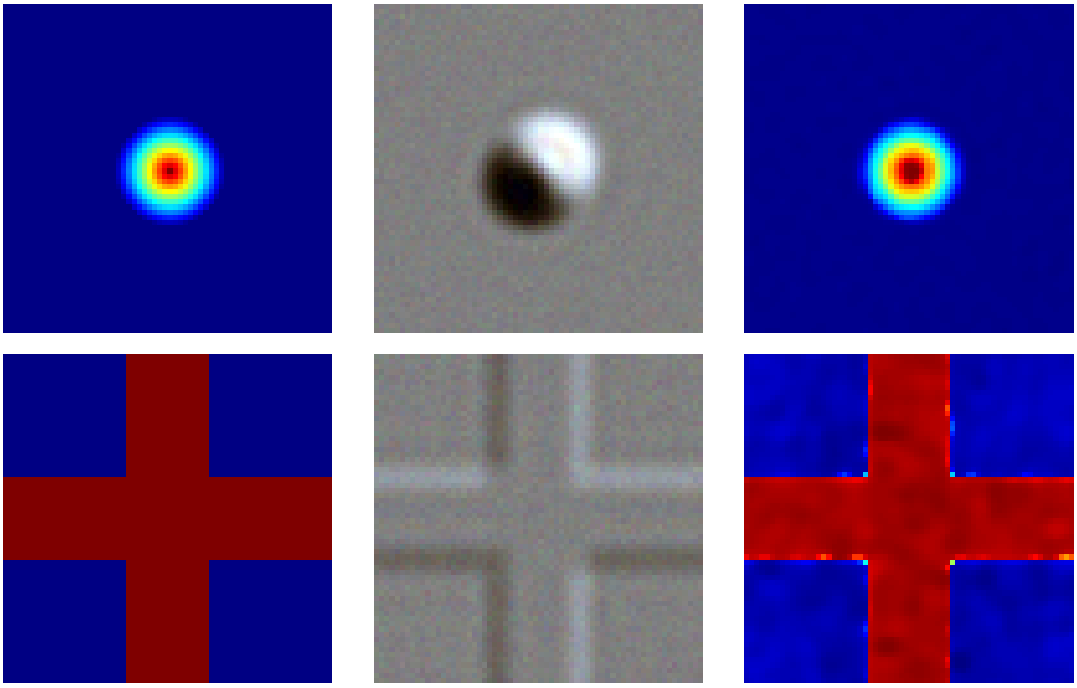

Figure 3.1: Data and results for the cone (top row) and cross (bottom row) objects. From left to right: true object, noisy DIC color image taken at shear angle $\frac{\pi}{4}$ rad and corrupted with white Gaussian noise at SNR = 4.5 dB, and reconstructed phase with the LMSD method from observations at shear angles equal to $-\pi/4$ rad and $\pi/4$ rad.

SNR values chosen in the simulations were 9 dB and 4.5 dB.

As far as the regularization parameter μ and the threshold δ in (3.11) are concerned, these have been manually chosen from a fixed range in order to obtain a visually satisfactory reconstruction. Note that the parameters were first set in the differentiable case ($\delta > 0$) for the LMSD and the nonlinear CG methods and then the same value of the parameter μ was used also in the nondifferentiable case ($\delta = 0$) for the ILA method. The values reported below have been used for each simulation presented in this section. The resulting values have been $\mu = 10^{-2}, \delta = 10^{-2}$ for the cone and $\mu = 4 \cdot 10^{-2}, \delta = 10^{-3}$ for the cross.

Some details regarding the choice of the parameters involved in the optimization methods of Section 3.4 are now provided. The linesearch parameters ρ, ω of the LMSD and ILA methods have been respectively set to 0.5, 10^{-4}. These are the standard choices for the Armijo parameters, however it is known that the linesearch algorithm is not so sensible to modifications of these values [14, 71]. The parameter γ in the Armijo–like rule (3.30) has been fixed equal to 1, which corresponds to the mildest choice in terms of decrease of the objective function J. The parameter m in Algorithm 1 is typically a small value ($m = 3, 4, 5$), in order to avoid a significant computational cost in the calculation of the steplengths $\alpha_n^{(0)}$; here we let $m = 4$. The same choice for m is done in Algorithm 2, where the values $\alpha_n^{(0)}$ are constrained in the interval $[\alpha_{\min}, \alpha_{\max}]$ with $\alpha_{\min} = 10^{-5}$ and $\alpha_{\max} = 10^2$. The dual problem (3.26) is addressed, at each iteration of ILA, by means of algorithm FISTA [10] which is stopped by using criterion

(3.28) with $\eta = 10^{-6}$. This value represents a good balance between convergence speed and computational time per iteration [17]. Concerning the nonlinear CG methods equipped with the strong Wolfe conditions, we use the same parameters as done in [41] and we initialize the related backtracking procedure as suggested in [66, p. 59]. Regarding the CG methods endowed with the polynomial approximation, a restart of the method is performed by taking a steepest descent step, whenever the search direction fails to be a descent direction. Finally, the constant phase object $\phi^{(0)} = 0$ is chosen as initial guess for all methods.

In order to evaluate the performance of the phase reconstruction methods proposed in Section 3.4, we will make use of the following error distance

$$E(\phi^{(n)}, \phi^*) = \min_{c\in\mathbb{R}} \frac{\|\phi^{(n)} - \phi^* - c\mathbf{1}\|}{\|\phi^*\|} = \frac{\|\phi^{(n)} - \phi^* - \bar{c}\mathbf{1}\|}{\|\phi^*\|} \tag{3.35}$$

where ϕ^* is the phase to be reconstructed and $\bar{c} = \sum_{j\in\chi} \frac{(\phi_j^{(n)} - \phi_j^*)}{N}$. Unlike the usual root mean squared error, which is recovered by setting $c = 0$ in (3.35), the error distance defined in (3.35) is invariant with respect to phase shifts, i.e.

$$E(\phi + c\mathbf{1}, \phi^*) = E(\phi, \phi^*), \quad \forall \phi \in \mathbb{R}^N,\ \forall c \in \mathbb{R}. \tag{3.36}$$

That makes the choice of (3.35) well–suited for problem (3.10), whose solution might be recovered only up to a real constant.

The methods have been run for the cone and cross phantoms with the parameters setting previously outlined. On one hand, the iterations of the LMSD and the CG methods have been arrested when the following stopping criterion based on the decrease of the gradient norm

$$\|\nabla J(\phi^{(n)})\| \leq \kappa \tag{3.37}$$

was met with $\kappa = 4 \cdot 10^{-2}$ for the cone and $\kappa = 10^{-3}$ for the cross. On the other hand, the ILA method has been stopped when the error up–to–a–constant between two successive iterates was lower than a prefixed $\kappa > 0$, that is

$$\frac{\left\|\phi^{(n+1)} - \phi^{(n)} - \left(\overline{\phi^{(n+1)} - \phi^{(n)}}\right)\mathbf{1}\right\|}{\|\phi^{(n+1)}\|} \leq \kappa, \tag{3.38}$$

where $\overline{\phi^{(n+1)} - \phi^{(n)}}$ is the mean value of the difference between the two objects. The tolerance κ in (3.38) was set equal to $5 \cdot 10^{-5}$ for the cone and 10^{-4} for the cross.

In Figure 3.2 we show the reconstruction error provided by the different methods as a function of the computational time. Among the CG methods, we report only the results obtained by the PR algorithm combined with a polynomial–approximation–based linesearch (PR–PA) and the FR–PR one in which the linesearch parameter is computed with the SW conditions (FR–PR–SW), since they always outperformed the other possible choices. From the plots of Figure

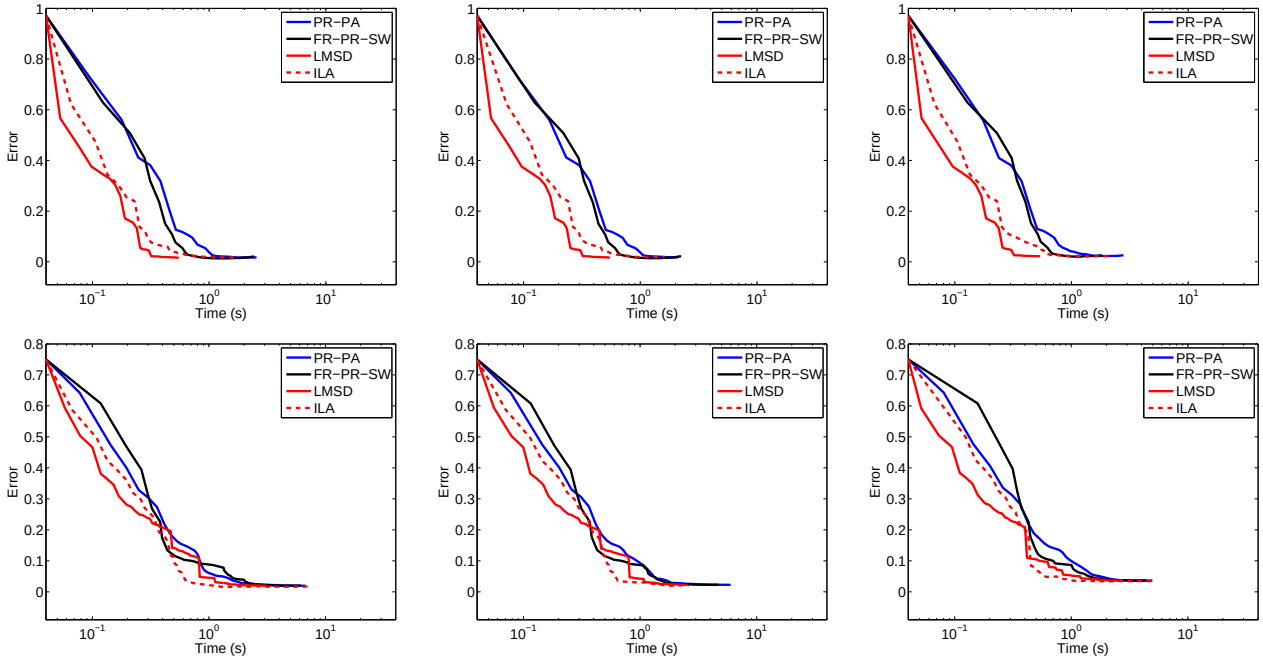

Figure 3.2: Error versus computational time plots for the cone (top row) and cross (bottom row) objects. From left to right: noise–free data, SNR = 9 dB and SNR = 4.5 dB.

3.2, it can be drawn that each method is quite stable with respect to the noise level on the DIC images. However, in terms of time efficiency, LMSD outperforms the CG methods in both tests, showing a time reduction of at least 50% to satisfy the stopping criterion. Furthermore, what emerges by looking at Tables 3.2 and 3.3 is that the CG methods are much more computationally demanding than LMSD. For instance, in the case of the cone (Table 3.2), LMSD evaluates the function less than 2 times per iteration. By contrast, the backtracking procedure exploited in the FR–PR–SW method requires an average of 4 evaluations per iteration of both the function and gradient to satisfy the strong Wolfe conditions, whereas the PR–PA method, despite evaluating the gradient only once, need on average 12 evaluations of the function before detecting the correct three–points–interval (see [72]). One could reduce the number of evaluations in PR–PA by properly tuning the initial parameters of the linesearch. However, as mentioned before, this method is quite sensitive to this choice, and little variations might result in a great increase of the number of restarts and, eventually, in the divergence of the algorithm. In addition, it seems that the optimal value of these parameters strictly depends on the object to be reconstructed.

3.5.2 Comparison between LMSD and ILA

We now compare the performance of LMSD and ILA. On one hand, ILA reconstructs the cross object slightly better than LMSD. Indeed, ILA provides the lowest reconstruction error in Table 3.3 for each SNR value and the corresponding phase estimates have better preserved edges, as clearly depicted in Figure 3.3, where we consider the following "up–to–a–constant" residual

$$R_j = \left| \phi_j - \phi_j^* - \overline{\phi - \phi^*} \right|, \quad \forall j \in \chi \tag{3.39}$$

SNR (dB)	Algorithm	Iterations	# f	# g	Time (s)	Obj fun	Error
∞	PR–PA	37	465	37	2.55	0.89	1.74 %
	FR–PR–SW	38	157	157	2.44	0.89	2.09 %
	LMSD	29	35	29	0.55	0.89	1.64 %
	ILA	66	119	66	1.77	0.52	1.76 %
9	PR–PA	31	389	31	2.12	1.65	1.81 %
	FR–PR–SW	37	142	142	2.24	1.65	2.19 %
	LMSD	29	35	29	0.55	1.65	1.69 %
	ILA	60	91	60	1.56	1.29	1.91 %
4.5	PR–PA	41	514	41	2.79	6.88	2.57 %
	FR–PR–SW	34	115	115	1.81	6.88	2.54 %
	LMSD	29	35	29	0.54	6.88	2.22 %
	ILA	61	104	61	1.56	6.80	2.50 %

Table 3.2: Cone tests. From left to right: number of iterations required to meet the stopping criteria, number of function and gradient evaluations, execution time, objective function value and error achieved at the last iteration.

SNR (dB)	Algorithm	Iterations	# f	# g	Time (s)	Obj fun	Error
∞	PR–PA	138	1373	138	6.73	1.01	1.98 %
	FR–PR–SW	109	423	423	6.14	1.01	1.98 %
	LMSD	168	231	168	3.09	1.01	2.00 %
	ILA	100	176	100	7.18	0.87	1.66 %
9	PR–PA	121	1209	121	5.97	1.96	2.26 %
	FR–PR–SW	106	323	323	4.69	1.96	2.25 %
	LMSD	140	190	140	2.52	1.96	2.27 %
	ILA	57	106	57	2.60	1.82	1.94 %
4.5	PR–PA	98	997	98	4.97	8.57	3.63 %
	FR–PR–SW	96	300	300	4.41	8.57	3.63 %
	LMSD	152	221	152	2.75	8.57	3.64 %
	ILA	97	179	97	5.26	8.47	3.46 %

Table 3.3: Cross tests. From left to right: number of iterations required to meet the stopping criteria, number of function and gradient evaluations, execution time, objective function value and error achieved at the last iteration.

to measure the quality of the reconstructions provided by the two methods. This result was expected, since ILA addresses problem (3.10) with the standard TV functional ($\delta = 0$ in (3.11)), which is more suited than HS regularization ($\delta > 0$) when the object to be reconstructed is piecewise constant. On the other hand, ILA may be computationally more expensive since, unlike LMSD, it requires to iteratively solve the inner subproblem (3.26) at each outer iteration. Indeed, looking at Table 3.3 we notice that, although the number of function evaluations per iteration in LMSD and ILA is quite similar (on average around 1.4 for LMSD and 1.8 for ILA) and the ILA iterations are stopped way before the LMSD ones, the computational time in ILA is always higher. For instance, in the case SNR = 9 dB, the methods require approximately the same time, although the number of iterations of ILA is more than halved. This fact is explained if we look at the average number of inner iterations required by ILA to compute the approximate proximal point: 21.3, 10.11 and 13.43 for SNR $= \infty, 9, 4.5$ dB respectively. Analogous conclusions on the costs per iteration can be drawn by considering the results on the

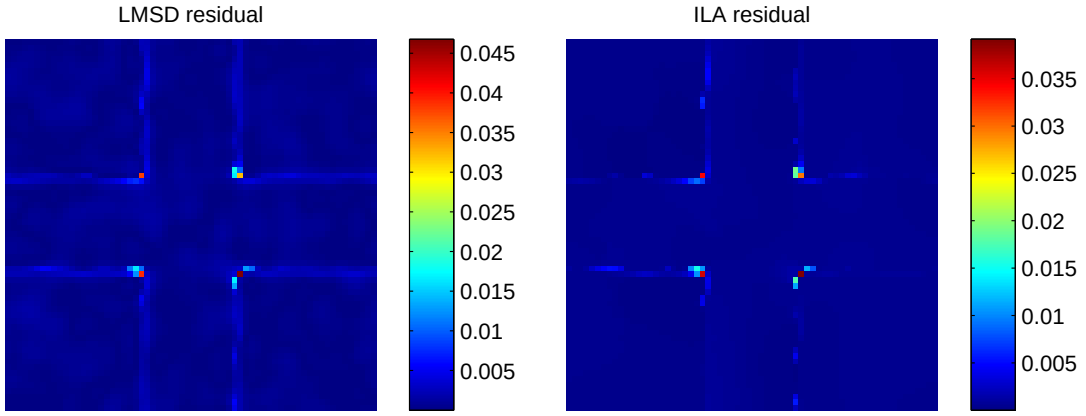

Figure 3.3: Cross test. The residuals defined in (3.39) for the reconstructions provided by LMSD and ILA, respectively, when the acquired images are corrupted with SNR = 9 dB.

cone object (see Table 3.2). In this case, LMSD is able to achieve a lower reconstruction error w.r.t. ILA in very few iterations, providing a remarkable gain in the computational time needed.

In order to deepen the analysis between the differentiable TV approximation and the original nondifferentiable one, we compared the LMSD and ILA methods in one further realistic simulation. In particular, we considered the "grid" object in Figure 3.4, which is a 1388×1040 image emulating the phase function of a multi–area calibration artifact[2], which measures 1.212 rad inside the black regions and 2.187 rad inside the white ones. The setup of the two methods is identical to that of the previous tests (with the exception of the numerical aperture of the objective NA which has been set equal to 0.8), and the parameters μ (for both models) and δ (for the smooth TV functional) have been set equal to $2 \cdot 10^{-1}$ and 10^{-1}, respectively. Instead of three levels of noise, here we only considered a SNR equal to 9 dB. In Figure 3.5 we report the behaviour of the error (3.35) as a function of time and the number of inner iterations needed by ILA to address problem (3.26)–(3.28).

The grid dataset confirms the remarks previously done, since ILA takes almost twice as long compared to LMSD to provide an estimate of the phase. This is again due to the number of inner iterations, which starts to oscillatory increase after the first 20 iterations (see Figure 3.5). To conclude, we reckon that the LMSD method is generally preferable since, unlike ILA, it does not require any inner subproblem to be solved and thus it is generally less expensive from the computational point of view. However, the ILA method should be considered as a valid alternative when the object to be reconstructed is piecewise constant.

3.5.3 Influence of color and bias retardation on phase reconstruction

Another analysis of our interest was to observe how color information and bias retardation in the observations affect the behavior of phase reconstruction. We set four scenarios for

[2]Bruker AFM Probes–Product description APCS-0099.
`http://www.brukerafmprobes.com/a-3472-apcs-0099.aspx`

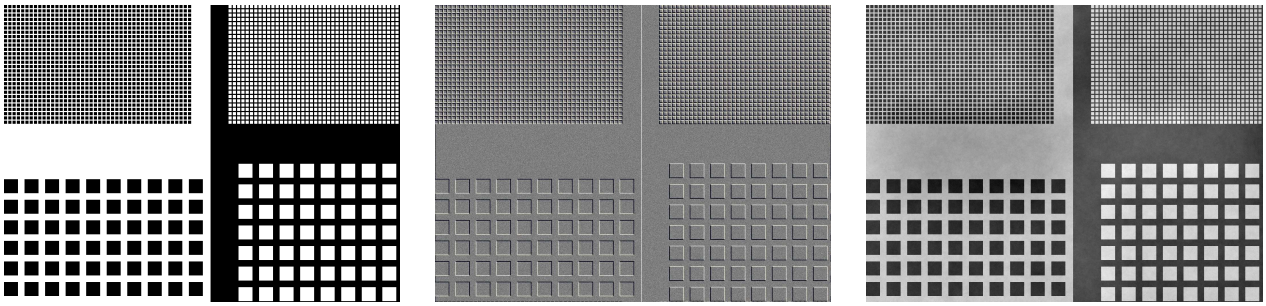

Figure 3.4: Data and results for the grid object. From left to right: true object, noisy DIC color image taken at shear angle $\frac{\pi}{4}$ rad and corrupted with white Gaussian noise at SNR = 9 dB, and reconstructed phase with the LMSD method from observations at shear angles equal to $-\pi/4$ rad and $\pi/4$ rad.

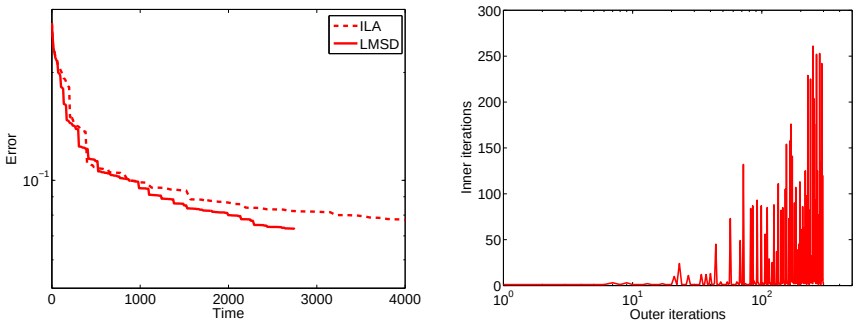

Figure 3.5: Grid test. From left to right: error versus time plots for LMSD and ILA and number of inner iterations versus number of outer iterations for ILA.

comparison: independent monochromatic observations with red, green, and blue light, and polychromatic observation where all wavelengths are combined. For each of these scenarios we used the cross object to generate 100 observations at different realizations of noise, for both SNR = 4.5 dB and SNR = 9 dB, and bias retardation of 0 rad and $\pi/2$ rad, at shear angles equal to $-\pi/4$ rad and $\pi/4$ rad. We tested the LMSD method to perform the reconstructions; results for SNR = 4.5 dB are shown in Figure 3.6 and for SNR = 9 dB in Figure 3.7.

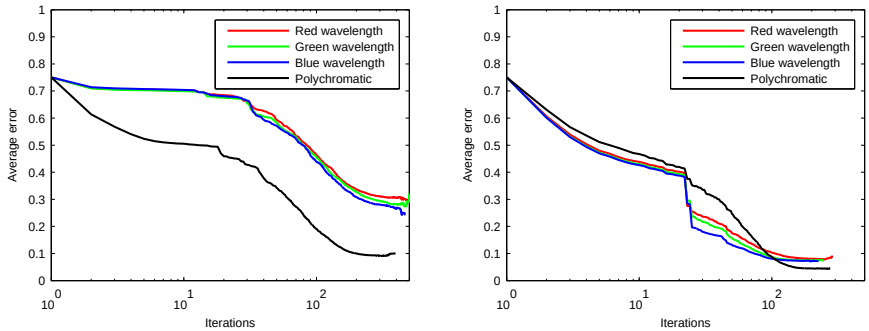

Figure 3.6: Average error comparison between monochromatic and polychromatic reconstructions. SNR = 4.5 dB. Left: bias 0 rad; right: bias $\pi/2$ rad.

The lines show the average error over the 100 observations. It is noticed that for 0 rad

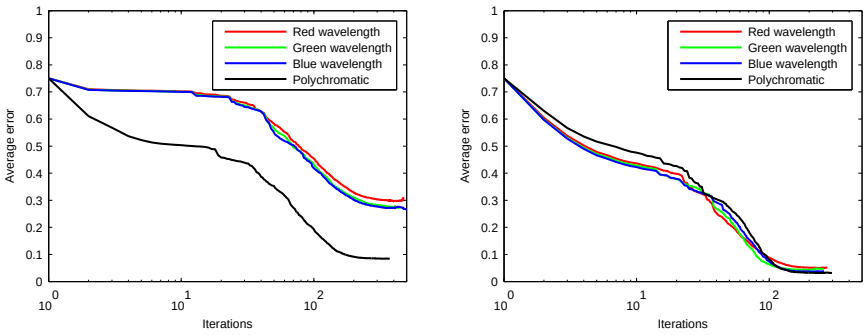

Figure 3.7: Average error comparison between monochromatic and polychromatic reconstructions. SNR = 9 dB. Left: bias 0 rad; right: bias $\pi/2$ rad.

bias retardation, the reconstruction for polychromatic observations behave better than for the monochromatic ones, even though the amount of error is not promising of a good reconstruction. For $\pi/2$ rad bias retardation the algorithm stops before the maximum number of iterations (500) is reached. In this case, for both levels of noise, the performance of the reconstruction with polychromatic light is quite comparable with monochromatic light. Another interesting finding about the convergence for monochromatic light, is that for all cases, it happens in the order red–green–blue; this is due to the fact that the amplitude PSF for blue light has the bigger frequency support, thus provides more information for reconstruction.

3.6 Summary

In this chapter we provided both theoretical and practical contributions to the inverse problem of phase estimation from polychromatic DIC images. First of all, we studied the analytical properties of the LS data fidelity function arising from a maximum likelihood approach, showing its periodicity, shift–invariance and analyticity. Secondly, we analyzed the minimization problem of the functional given by the sum of the discrepancy term and an edge–preserving regularizer, proving the existence of minimum points. Finally, we proposed two recent optimization strategies for the case of both smooth and nonsmooth regularizers, and compared their performance with state–of–the–art conjugate gradient methods. In particular, for the HS regularizer we considered the LMSD method while in the case of the nonsmooth TV functional we proposed to exploit the ILA approach.

From the analysis we performed we drive the conclusions that an edge–preserving regularizer combined with an effective optimization tool can rapidly provide a good reconstruction of the phase. Of course the LMSD method has a much simpler structure than ILA and, in general, it should converge faster since ILA depends on two cycles of iterations (the outer defining the sequence and the inner computing the proximal point). However, in our tests the differences in time are not so significant, therefore a possible user might prefer to avoid the choice of a further parameter (the δ defining the HS term) and adopt the standard LS+TV model.

We highlight that the efficiency in the computational time is accomplished by the

compact and faster calculation of the gradient in Equation (3.8). We reformulated this expression into a convolution-based operator which allows a complexity of $\mathcal{O}\left(\mathrm{MP}\log\mathrm{MP}\right)$ for an image of size $\mathrm{M}\times\mathrm{P}$, instead of $\mathcal{O}\left(\mathrm{MP}^2\right)$ initally reported in the literature by Preza et al [72].

A final remark is given to the fact that for the case when the bias retardation is $\pi/2$ rad, the phase reconstruction is invariant to the color information. This means that if there are available observations done with a single wavelength, the reconstruction will be as good as if it is done with polychromatic observations.

Chapter 4

Constrained Phase Estimation for DIC Microscopy

In this chapter we propose to follow another approach to deal with the non-linearity and non-convexity of the DIC phase estimation problem. In the previous chapter we presented two optimization methods for an unconstrained cost function. Here we introduce a constraint by doing a change of the optimization variable and we fix the observations to a single wavelength λ_ℓ, for $\ell \in \{1, 2, 3\}$, according to the results obtained in Chapter 3 that show that it is possible to reconstruct the phase with only one wavelength.

Let us define $u \in \mathbb{C}^{MP}$, such that $u_j = e^{-i\frac{\phi_j}{\lambda_\ell}}$ and $|u_j| = 1$, $\phi_j \in \mathbb{R}$ for all $j \in \chi$ (where $\chi = \{1, \ldots, M\} \times \{1, \ldots, P\}$). For the sake of simplicity, u_j is the complex number $(u_r + iu_i)_j$, with real part u_r and imaginary part u_i. According to this, and recalling models (3.1) and (3.2), the fit-to-data term under the variable u is expressed as

$$J_0(u) = \sum_{k=1}^{K} \sum_{j \in \chi} \left[(o_k)_j - a_1 \left| (h_k \otimes u)_j \right|^2 \right]^2 \tag{4.1}$$

and the inverse problem becomes

$$\begin{aligned} &\min_{u \in \mathbb{C}^{MP}} J_0(u) \\ &\text{subject to } |u_j| = 1, \text{ for all } j \in \chi \end{aligned} \tag{4.2}$$

Once an optimal solution $\hat{u}$ to problem (4.2) is found, we compute the searched phase as

$$\hat{\phi}_j = \lambda_\ell . \left(\arctan \left(\frac{\hat{u}_i}{\hat{u}_r} \right)_j \right) \tag{4.3}$$

Functional J_0 in (4.1) makes a mapping from $\mathbb{C}^{\mathrm{MP}}$ to $\mathbb{R}$ which gives its non-holomorphic nature and hence, not $\mathbb{C}$-derivable. As it is expressed according to a complex variable u but not according to the phase variable ϕ, it has no explicit properties such as the ones stated in Lemma 1. J_0 holds the smoothness property as long as it is expressed in terms of real variables as follows

$$\begin{aligned} J_0 : \mathbb{R}^{\mathrm{MP}} \times \mathbb{R}^{\mathrm{MP}} &\longrightarrow \mathbb{R} \\ (u_r, u_i)_j &\longmapsto J_0 (u_r, u_i)_j \end{aligned} \tag{4.4}$$

for all $j \in \chi$. In order to compute in a straight forward way the derivatives of J_0 with respect to $u = (u_r, u_i)$, we use the Wirtinger derivatives formalism as introduced by Adali et al [2] and

Candès et al [21], which we present in section 4.1.

Problem (4.2) is also a severely ill-posed problem, which also requires to add a regularization function as we did previously for problem (3.10). This transforms our optimization model as follows

$$\begin{aligned} &\min_{u\in\mathbb{C}^{MP}} J(u) \equiv J_0(u) + J_{TV}(u) \\ &\text{subject to } |u_j| = 1, \text{ for all } j \in \chi \end{aligned} \tag{4.5}$$

where J_{TV} is the smooth total variation functional

$$J_{TV}(u) = \mu \sum_{j\in\chi} \sqrt{|((\mathcal{D}u)_j)_1|^2 + |((\mathcal{D}u)_j)_2|^2 + \delta^2}, \tag{4.6}$$

with $\mu > 0$ the regularization parameter, $\delta \geq 0$ the smoothness parameter, and the discrete gradient operator $\mathcal{D} : \mathbb{C}^{MP} \longrightarrow \mathbb{C}^{2MP}$ is set through the standard finite difference with periodic boundary conditions

$$(\mathcal{D}u)_{j_1,j_2} = \begin{pmatrix} ((\mathcal{D}u)_{j_1,j_2})_1 \\ ((\mathcal{D}u)_{j_1,j_2})_2 \end{pmatrix} = \begin{pmatrix} u_{j_1+1,j_2} - u_{j_1,j_2} \\ u_{j_1,j_2+1} - u_{j_1,j_2} \end{pmatrix}, \; u_{M+1,j_2} = u_{1,j_2}, \; u_{j_1,P+1} = u_{j_1,1}$$

4.1 Wirtinger Derivatives

Before going further in our optimization problem, we present a short review of the concept of Wirtinger derivatives in order to develop the computation of the gradient of functional (4.1). Let us start by defining a real-valued function

$$\begin{aligned} f : \mathbb{C} &\longrightarrow \mathbb{R} \\ z &\longmapsto f(z) \end{aligned} \tag{4.7}$$

As it maps $\mathbb{C}$ into $\mathbb{R}$ it is a non-holomorphic function, hence it is not $\mathbb{C}$-derivable. However, as we are interested in optimizing f, we can consider this function as

$$\begin{aligned} f : \mathbb{R}\times\mathbb{R} &\longrightarrow \mathbb{R} \\ (z_r, z_i) &\longmapsto f(z_r, z_i) = f(z) \end{aligned} \tag{4.8}$$

and run a gradient descent algorithm on the real and imaginary components of f as follows

$$\begin{aligned} z_r^{(n+1)} &= z_r^{(n)} - \alpha_n \frac{\partial f(z_r^{(n)}, z_i^{(n)})}{\partial z_r} \\ z_i^{(n+1)} &= z_i^{(n)} - \alpha_n \frac{\partial f(z_r^{(n)}, z_i^{(n)})}{\partial z_i} \end{aligned} \tag{4.9}$$

When dealing with high dimensional complicated funcional as computing $\frac{\partial f(z_r, z_i)}{\partial z_r}$ and $\frac{\partial f(z_r, z_i)}{\partial z_i}$ can be tedious, that is why we have chosen to use the Wirtinger derivatives (denoted with the subscript W), which are defined as follows

$$\frac{\partial_W f(z)}{\partial z} \triangleq \frac{1}{2}\left(\frac{\partial f(z)}{\partial z_r} - i\frac{\partial f(z)}{\partial z_i}\right) \qquad \text{and} \qquad \frac{\partial_W f(z)}{\partial \bar{z}} \triangleq \frac{1}{2}\left(\frac{\partial f(z)}{\partial z_r} + i\frac{\partial f(z)}{\partial z_i}\right) \tag{4.10}$$

There exists an important property of the Wirtinger derivatives explained by Adali in [2] and Candès in [23] (see Appendix C.1), which leads to the following identity

$$\frac{\partial_W f}{\partial z} := \left.\frac{\partial f(z,\bar{z})}{\partial z}\right|_{\bar{z}=constant} \qquad \frac{\partial_W f}{\partial \bar{z}} := \left.\frac{\partial f(z,\bar{z})}{\partial \bar{z}}\right|_{z=constant} \tag{4.11}$$

Hence, Algorithm (4.9) is rewritten as

$$z^{(n+1)} = z^n - \alpha_n \cdot 2 \cdot \frac{\partial_W f}{\partial \bar{z}} \tag{4.12}$$

where $\frac{\partial_W f}{\partial \bar{z}}$ is easily computed by the second identity in (4.11)

4.1.1 n-dimensional Wirtinger derivatives

Since we are dealing with a 2-dimensional complex variable, it is pertinent to present the notation of Wirtinger derivatives in the n-dimensional case (see Appendix C.2 for details).

Define the n-dimensional column vector $\mathbf{z}$ by $\mathbf{z} = (z_1, \ldots, z_n)^T \in \mathbb{C}^n$, where $z_\ell = z_{r_\ell} + iz_{i_\ell}$ for $\ell = 1, \ldots, n$, or equivalently $\mathbf{z} = \mathbf{z}_r + i\mathbf{z}_i$ with $\mathbf{z}_r = (z_{r_1}, \ldots, z_{r_n})$ and $\mathbf{z}_i = (z_{i_1}, \ldots, z_{i_n})$. The corresponding conjugate vector of $\mathbf{z}$ is $\bar{\mathbf{z}} = (\bar{z}_1, \ldots, \bar{z}_n)^T \in \mathbb{C}^n$. This allows us to define the following real-valued function

$$\begin{aligned} f : \mathbb{C}^n &\longrightarrow \mathbb{R} \\ \mathbf{z} &\longmapsto f(\mathbf{z}) \end{aligned} \tag{4.13}$$

with complex conjugate coordinates $\begin{bmatrix} \mathbf{z} \\ \bar{\mathbf{z}} \end{bmatrix} \in \mathbb{C}^n \times \mathbb{C}^n$.

As in the one-dimensional case in (4.10), the n-dimensional Wirtinger derivatives are defined as

$$\frac{\partial_W f}{\partial z_\ell} \triangleq \frac{1}{2}\left(\frac{\partial f}{\partial z_{r_\ell}} - i\frac{\partial f}{\partial z_{i_\ell}}\right) \qquad \text{and} \qquad \frac{\partial_W f}{\partial \bar{z}_\ell} \triangleq \frac{1}{2}\left(\frac{\partial f}{\partial z_{r_\ell}} + i\frac{\partial f}{\partial z_{i_\ell}}\right) \qquad \text{for } \ell = 1, \ldots, n \tag{4.14}$$

from which we can describe the generalized complex derivatives

$$\begin{aligned} \frac{\partial_W f}{\partial \mathbf{z}} &:= \frac{\partial f(\mathbf{z}, \bar{\mathbf{z}})}{\partial \mathbf{z}} = \left.\left(\frac{\partial f(z,\bar{z})}{\partial z_1}, \ldots, \frac{\partial f(z,\bar{z})}{\partial z_n}\right)\right|_{\bar{\mathbf{z}}=constant} \\ \frac{\partial_W f}{\partial \bar{\mathbf{z}}} &:= \frac{\partial f(\mathbf{z}, \bar{\mathbf{z}})}{\partial \bar{\mathbf{z}}} = \left.\left(\frac{\partial f(z,\bar{z})}{\partial \bar{z}_1}, \ldots, \frac{\partial f(z,\bar{z})}{\partial \bar{z}_n}\right)\right|_{\mathbf{z}=constant} \end{aligned} \tag{4.15}$$

The gradient vector is defined as

$$\nabla_W f(\mathbf{z}) \triangleq \left(\frac{\partial f(\mathbf{z},\bar{\mathbf{z}})}{\partial \mathbf{z}}\right)^* = \left(\frac{\partial_W f(\mathbf{z})}{\partial \mathbf{z}}\right)^* \triangleq \frac{1}{2}\left(\frac{\partial f(\mathbf{z})}{\partial \mathbf{z}_r} + i\frac{\partial f(\mathbf{z})}{\partial \mathbf{z}_i}\right) \tag{4.16}$$

where $*$ represents the conjugate transpose.

In conclusion, Wirtinger derivatives provide us with a compact notation in order to obtain the gradient of our non-holomorphic optimization problem. In the following section we present the development of the gradient following that notation.

4.2 Gradient of $J_0(u)$

Now we consider again problem (4.1)

$$J_0(u) = \sum_{k=1}^{K}\sum_{j\in\chi}\left[(o_k)_j - a_1\left|(h_k \otimes u)_j\right|^2\right]^2$$

which can be stated as the mapping $\begin{aligned} J_0 : \mathbb{C}^{MP} &\longrightarrow \mathbb{R} \\ u &\longmapsto J_0(u) \end{aligned}$.

According to the Wirtinger theory previously described, and because of the complex coordinates, we can reformulate problem (4.1) in the following way

$$\begin{aligned} \tilde{J}_0 : \mathbb{C}^{MP}\times\mathbb{C}^{MP} &\longrightarrow \mathbb{R} \\ (u,\bar{u}) &\longmapsto \tilde{J}_0(u,\bar{u}) = \sum_{k=1}^{K}\sum_{j\in\chi}\left[(o_k)_j - \left[(h_k\otimes u)_j\cdot\left(\bar{h}_k\otimes\bar{u}\right)_j\right]\right]^2 \end{aligned} \tag{4.17}$$

where the gradient of J_0 and the gradient of $\tilde{J}_0$ relates to each other as $\nabla\tilde{J}_0 = (\nabla_1 J_0,\ldots,\nabla_{MP}J_0)$.

If we take the partial derivative of $\tilde{J}_0$ with respect to any element u_s for all $s\in\chi$ we have

$$\frac{\partial\tilde{J}_0(u,\bar{u})}{\partial u_s} = \sum_{k=1}^{K}\sum_{j\in\chi} 2\left[|(h_k\otimes u)_j|^2 - (o_k)_j\right]\cdot\frac{\partial\left(|(h_k\otimes u)_j|^2\right)}{\partial u_s} \tag{4.18}$$

where

$$\frac{\partial\left(|(h_k\otimes u)_j|^2\right)}{\partial u_s} = \frac{\partial\left[(h_k\otimes u)_j\cdot(\bar{h}_k\otimes\bar{u})_j\right]}{\partial u_s} = \overline{(h_k\otimes u)}_j\cdot h_{k_{j-s}}$$

then,

$$\begin{aligned} \frac{\partial\tilde{J}_0(u,\bar{u})}{\partial u_s} &= \sum_{k=1}^{K}\sum_{j\in\chi} 2\left[|(h_k\otimes u)_j|^2 - (o_k)_j\right]\cdot\overline{(h_k\otimes u)}_j\cdot h_{k_{j-s}} \\ &= 2\sum_{k=1}^{K}\sum_{j\in\chi}\left\{\left[|(h_k\otimes u)_j|^2 - (o_k)_j\right]\cdot\overline{(h_k\otimes u)}_j\right\}\otimes h_k^{-t} \end{aligned}$$

where $(\cdot)^{-t}$ represents the matrix transpose in arrows and columns.

According to the identity (4.16), we can conclude that $\nabla J_0(u) = \left(\frac{\partial \tilde{J}_0(u,\bar{u})}{\partial u_s}\right)^*$, where $*$ represents the conjugate transpose. This finally lead us to

$$\nabla J_0(u) = 2\sum_{k=1}^{K}\sum_{j\in\chi}\left\{\left[|(h_k \otimes u)_j|^2 - (o_k)_j\right]\cdot(h_k \otimes u)_j\right\} \otimes \bar{h}_k^{-t} \tag{4.19}$$

4.3 Projected DIC Phase Estimation

Now we proceed to develop the solution to problem 4.5. In order to meet the constraint $|u| = 1$, we introduce the projection operator $P_{\mathcal{C}}$, where $\mathcal{C} = \left\{u \in \mathbb{C}^{MP} : |u_j| = 1, \text{ for all } j \in \chi\right\}$. Thus, we rewrite the problem as follows

$$\min_{u\in\mathcal{C}} J_P(u) := J_0(u) + J_{TV}(u) \tag{4.20}$$

We obtain the numerical solution to problem (4.20) by means of a standard gradient descent algorithm, such that each feasible solution meets the modulus 1 constraint. Having into account Wirtinger theory and Equations (4.9) and (4.12) we find that each iteration for $J_0(u)$ is computed in the following way

$$u^{(n+1)} = u^{(n)} - \alpha_n \cdot 2 \cdot \nabla J_0(u) \tag{4.21}$$

where $\nabla J_0(u)$ is defined in equation (4.19).

With this result it is possible to compute the feasible solution at that iteration applying the projection operator $P_{\mathcal{C}}$ as follows

$$\hat{u}_j^{(n+1)} = P_{\mathcal{C}}\left(u_j^{(n+1)}\right) = \frac{u_j^{(n+1)}}{\left|u_j^{(m+1)}\right|} \tag{4.22}$$

The numerical implementation of this gradient descent method is described in Algorithm 5, which has a polynomial linesearch strategy for controlling the steplength parameter α_n presented in Algorithm 6. Further details about Algorithm 6 can be found in [51].

Algorithm 5 Gradient descent method with projection

Choose $\omega \in (0,1)$, $[\beta_{\text{low}}, \beta_{\text{high}}] \subset (0,1)$,$m \in \mathbb{N}_{>0}$, $u^{(0)} \in \mathbb{C}^{MP}$, $\alpha_0 = 1$ and set $n = 0$.
While True

For $l = 1, \ldots, m$

1. Compute $J_P(u^{(n)})$ and $\nabla J_P(u^{(n)})$.
2. Beginning with $\alpha_0 = 1$, repeatedly reduce α using any strategy that satisfies $\alpha_n = [\beta_{\text{low}}\alpha_{n-1}, \beta_{\text{high}}\alpha_{n-1}]$ until (3.20) holds.
3. Compute $u^{(n+1)} = u^{(n)} - \alpha_n \nabla J_P(u^{(n)})$.
4. Compute the projection $\hat{u}^{(n+1)} = \dfrac{u^{(n+1)}}{\left|u^{(n+1)}\right|}$.

If "Stopping Criterion" is satisfied

5. Return

Else

6. Set $n = n + 1$.

EndIf

EndFor

EndWhile

4.4 Numerical Experiments

In this section we test the behavior of the projected gradient descend method described in Algorithm 5 and the Conjugate Gradient (Algorithm 3) with polynomial approximation (PR-PA), which was modified to do the projection over the modulus constraint, for solving problem (4.20). We have used the same objects as for the tests in section 3.5; parameter ω in (3.20) was set to 10^{-4}. The extreme values for the polynomial linesearch were set to $\beta_{\text{low}} = 0.1$ and $\beta_{\text{high}} = 0.5$

We have chosen two constant complex functions of module 1 as initial guesses, say $u_{01} = (1, i0)$ and $u_{02} = \left(\frac{1}{\sqrt{2}}, i\frac{1}{\sqrt{2}}\right)$, far from the true value. The stopping criteria were the tolerance for the norm of the gradient at each iteration set to 10^{-2} and a maximum of 5000 iterations for both objects.

The true phase ($\check{\phi}$) and specimen ($\check{u}$) functions for the cone object are shown in Figure 4.1 and in Figure 4.2 for the cross object. These plots show the true values as they were generated in the simulation; their color bars are independent to each other in order to show the exact range of values of each function.

Algorithm 6 Polynomial linesearch

Let $d^{(n)} = -\nabla J_P(u^{(n)})$ be the current search direction. Set $[\beta_{\text{low}}, \beta_{\text{high}}] \subset (0,1)$.
Let $\xi(\alpha) = J_P(u^{(n)} + \alpha d^{(n)})$ and set initial data: $\xi(0) = J_P(u^{(n)})$; $\xi'(0) = \nabla J_P(u^{(n)})^T d^{(n)}$; $\xi(1) = J_P(u^{(n)} + d^{(n)})$.

If $n = 0$

1. Set $\alpha_n = 1$.
2. Approximate $\xi(\alpha)$ by the quadratic polynomial
$$q(\alpha) = \xi(0) + \xi'(0)\alpha + [\xi(1) - \xi(0) - \xi'(0)]\alpha^2$$
whose global minimum is given by $\alpha_t = \dfrac{-\xi'(0)}{2[\xi(1) - \xi(0) - \xi'(0)]}$
3. Assign $\alpha_+ = \begin{cases} \beta_{\text{low}}\alpha_n & , \alpha_t \leq \beta_{\text{low}}\alpha_n \\ \alpha_t & , \beta_{\text{low}}\alpha_n < \alpha_t < \beta_{\text{high}}\alpha_n \\ \beta_{\text{high}}\alpha_n & , \alpha_t \leq \beta_{\text{high}}\alpha_n \end{cases}$
4. Update $\alpha_n = \alpha_+$

Else

5. Set initial data $\xi(0) = J_P(u^{(n)})$; $\xi'(0) = \nabla J_P(u^{(n)})^T d^{(n)}$; $\xi(\alpha_-)$; $\xi(\alpha_n)$, where α_- and α_n are the most recent values of α to fail to satisfy (3.20).
6. Approximate $\xi(\alpha)$ by the cubic polynomial
$$q(\alpha) = \xi(0) + \xi'(0)\alpha + c_2\alpha^2 + c_3\alpha^3$$
whose local minimum is at $\alpha_t = \dfrac{-c_2 + \sqrt{c_2^2 - 3c_3\xi'(0)}}{3c_3}$
7. Assign α_+ as in step 3.
8. Update $\alpha_n = \alpha_+$

EndIf

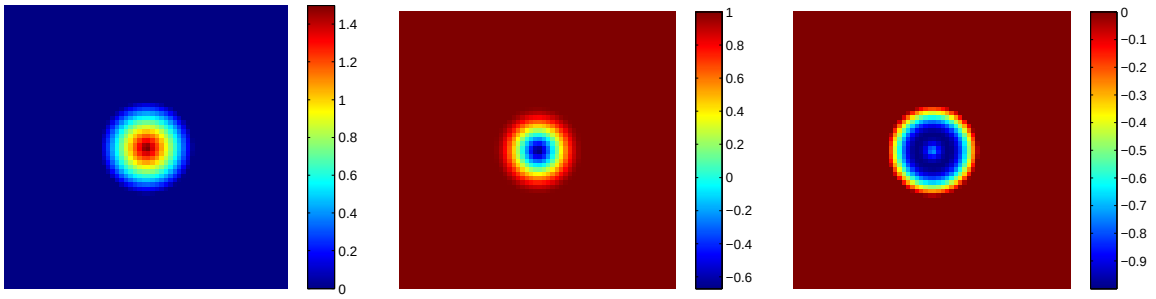

(a) (b) (c)

Figure 4.1: Cone object. True values for phase and specimen functions (a) Phase function $\check{\phi}$, (b) $\text{Re}\{\check{u}\}$, (c) $\text{Im}\{\check{u}\}$

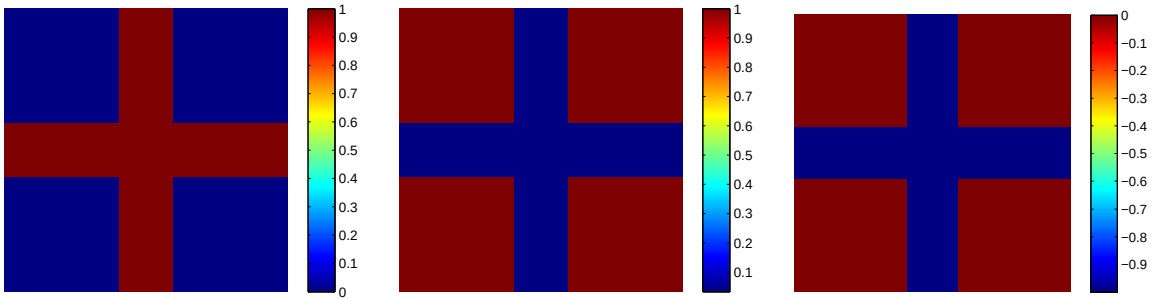

(a) (b) (c)

Figure 4.2: Cross object. True values for phase and specimen functions (a) Phase function $\check{\phi}$, (b) $\mathrm{Re}\{\check{u}\}$, (c) $\mathrm{Im}\{\check{u}\}$

In the following we present results for the Red color channel when bias $2\Delta\theta = \pi/2$ and SNR= 9dB. For the regularization parameters we have set $\mu = 4.10^{-2}$ and $\delta = 10^{-4}$ for both objects cone and cross. Each figure shows *a)* the real part of estimation $\hat{u}$ (denoted as $\mathrm{Re}\{\hat{u}\}$), *b)* the imaginary part of estimation $\hat{u}$ (denoted as $\mathrm{Im}\{\hat{u}\}$), *c)* the real part of residual between the true and estimated object $\mathrm{Re}\{|\hat{u} - \check{u}|\}$, *d)* the imaginary part of residual $\mathrm{Im}\{|\hat{u} - \check{u}|\}$, *e)* the reconstructed phase $\hat{\phi}$, *f)* the residual $\left|\hat{\phi} - \check{\phi}\right|$, and *g)* the up–to–a–constant residual $\left|\check{\phi}_j - \hat{\phi}_j - \overline{\check{\phi} - \hat{\phi}}\right|$, $\forall j \in \chi$ as in Equation (3.39). For the purpose of visualization in the comparison of results, the color bar for all plots has the same values dynamic, for both the specimen and the phase. Figures 4.4 to 4.12 are the results for the object cone, and Figures 4.14 to 4.24 for the cross object.

One of the objectives of these experiments was to analyze the influence of the projection operator on the output of the estimation for two initial guesses. Figure 4.4 presents the results without projection and Figure 4.5, with projection, for the initial guess $u_{01} = (1, i0)$ using Algorithm 5 (results for the Conjugate Gradient PR-PA can be found in Appendix D). In order to have a better understanding of the results, and since the dynamic of the estimated values are distant from the expected ones (true objects shown in Figures 4.1 and 4.2), we present in Figure 4.3 the true cone objects with color bars dynamic adjusted to the ones obtained in the results in Figures 4.4 and 4.5.

Although the shape of the specimen and the phase function are very well recovered, by observing the residual images for the specimen ((c) and (d)), there is a considerable difference with respect to the expected result. If we focus on the estimated phase ((e)) and the residual in (f), we corrobarate that its solution is recovered up to a real constant, as is observed in (g) where we calculate a more precise residual by giving up that constant. It is evident that there is no big difference in the estimations whether having or not the projection operator. However, if we analyze the performance of both algorithms in terms of their convergence, evolution of the norm of the gradient and error along the iterations, we observe that the projection operator provides more stability and gives more preference to the Gradient Descent method, see Figures 4.6 and 4.7.

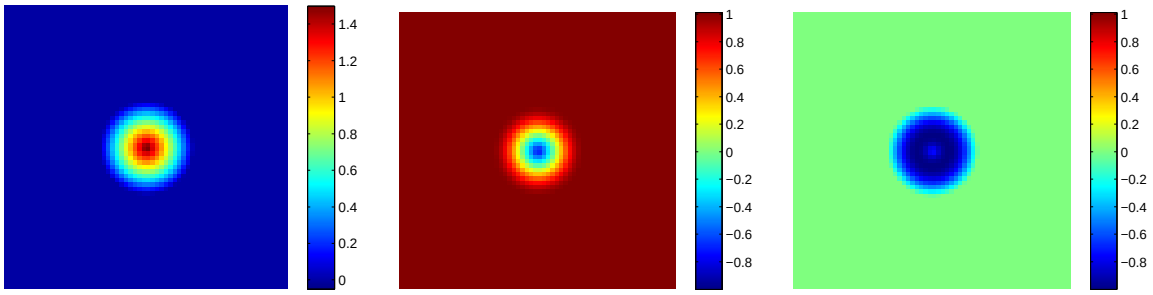

(a) (b) (c)

Figure 4.3: Cone object. True values for phase and specimen functions (a) Phase function $\check{\phi}$, (b) $\mathrm{Re}\{\check{u}\}$, (c) $\mathrm{Im}\{\check{u}\}$. (Same as in Figure 4.1, color bar adjusted to results in Figures 4.4 and 4.5).

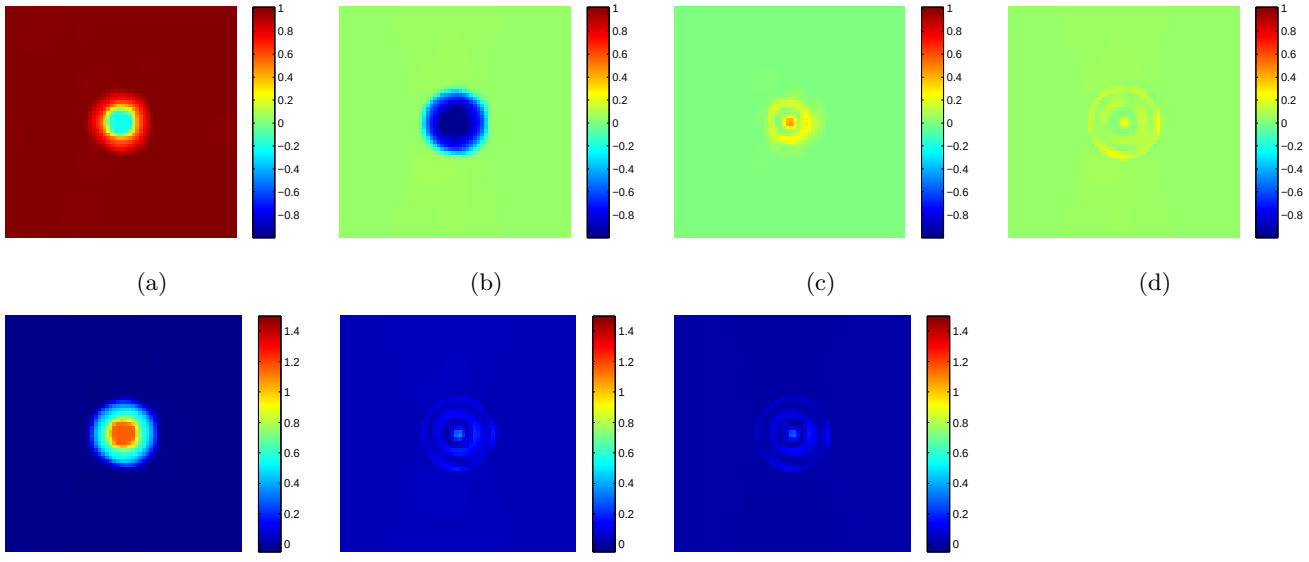

(a) (b) (c) (d)

(e) (f) (g)

Figure 4.4: Estimation of Gradient Descent method without projection, initial guess $u_{01} = (1, i0)$. (a) $\mathrm{Re}\{\hat{u}\}$, (b) $\mathrm{Im}\{\hat{u}\}$, (c) $\mathrm{Re}\{|\hat{u} - \check{u}|\}$, (d) $\mathrm{Im}\{|\hat{u} - \check{u}|\}$, (e) $\hat{\phi}$, (f) $\left|\hat{\phi} - \check{\phi}\right|$, (g) $\left|\check{\phi}_j - \hat{\phi}_j - \overline{\check{\phi} - \hat{\phi}}\right|$

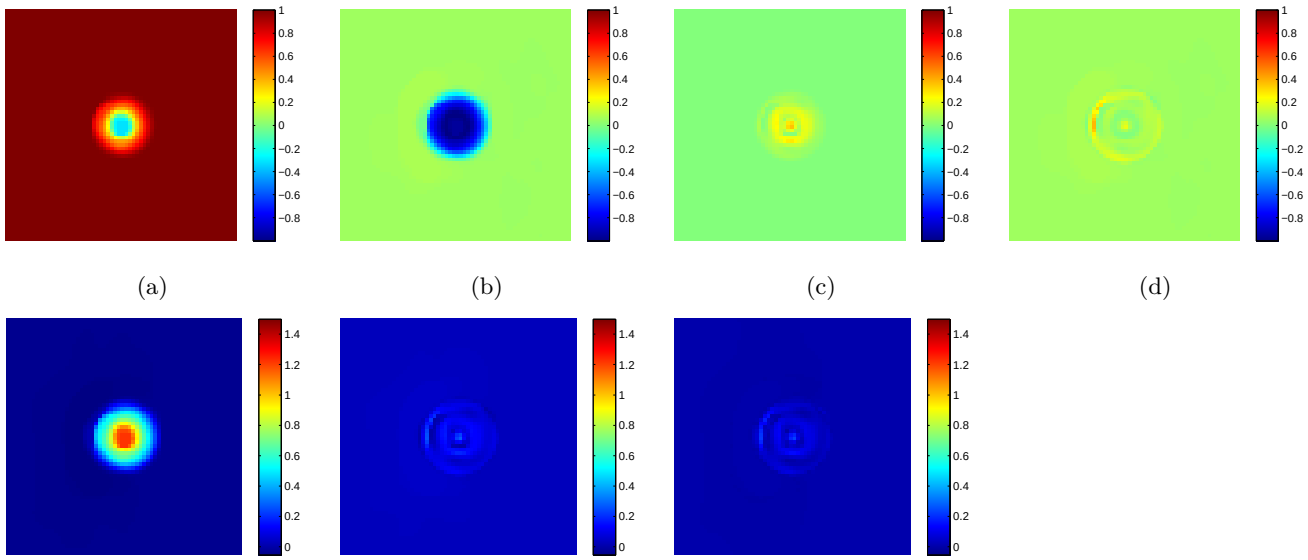

(a) (b) (c) (d)

(e) (f) (g)

Figure 4.5: Estimation of Gradient Descent method with projection, initial guess $u_{01} = (1, i0)$. (a) $\mathrm{Re}\{\hat{u}\}$, (b) $\mathrm{Im}\{\hat{u}\}$, (c) $\mathrm{Re}\{|\hat{u} - \check{u}|\}$, (d) $\mathrm{Im}\{|\hat{u} - \check{u}|\}$, (e) $\hat{\phi}$, (f) $\left|\hat{\phi} - \check{\phi}\right|$, (g) $\left|\check{\phi}_j - \hat{\phi}_j - \overline{\check{\phi} - \hat{\phi}}\right|$

Figures 4.6 and 4.7 present the comparison of performance for the Gradient Descent method (red curve) and the Conjugate Gradient PR-PA (blue curve), without and with projection respectively.

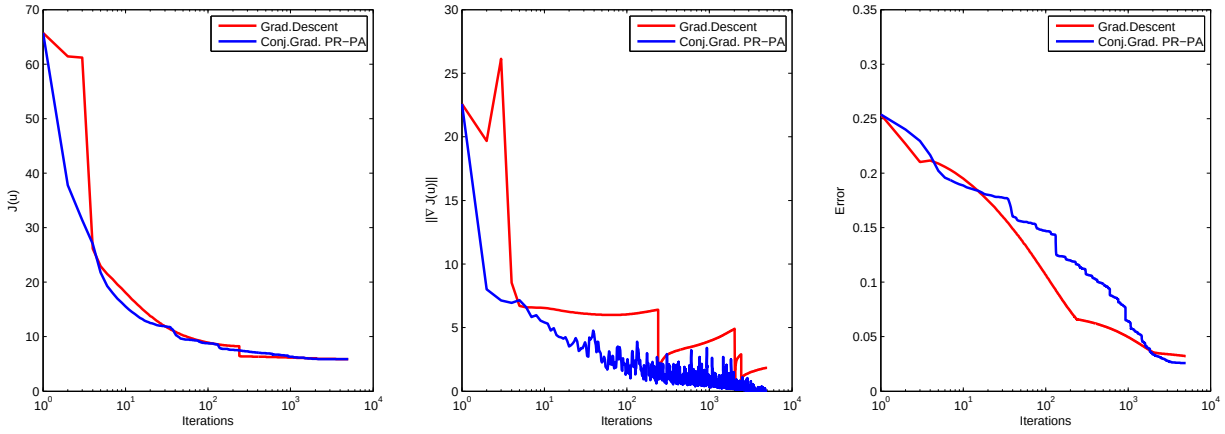

(a) (b) (c)

Figure 4.6: Methods comparison without projection, initial guess $u_{01} = (1, i0)$. (a) Convergence, (b) Norm of gradient, (c) Error

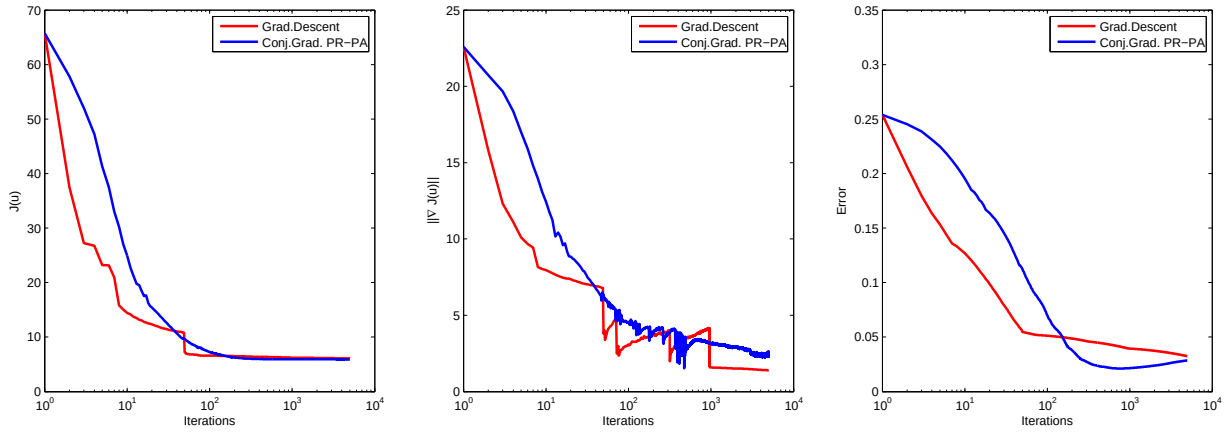

(a) (b) (c)

Figure 4.7: Methods comparison with projection, initial guess $u_{01} = (1, i0)$. (a) Convergence, (b) Norm of gradient, (c) Error

The results when initial guess is $u_{02} = \left(\frac{1}{\sqrt{2}}, i\frac{1}{\sqrt{2}}\right)$ are shown from Figure 4.9 to Figure 4.12. As in the previous case, the reconstructions are far from the true objects; much further than with initial guess $u_{01} = (1, i0)$. However, the behavior of the convergence and the norm of the gradient are smoother for this initial guess in both cases with and without projection. We present in Figure 4.8 the true cone values with color bars dynamic adjusted for the results of the estimation with this initial guess.

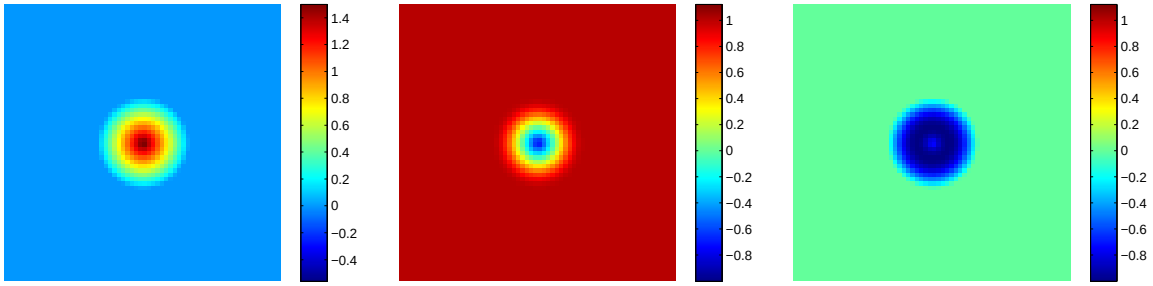

(a) (b) (c)

Figure 4.8: Cone object. True values for phase and specimen functions (a) Phase function $\check{\phi}$, (b) $\mathrm{Re}\{\check{u}\}$, (c) $\mathrm{Im}\{\check{u}\}$

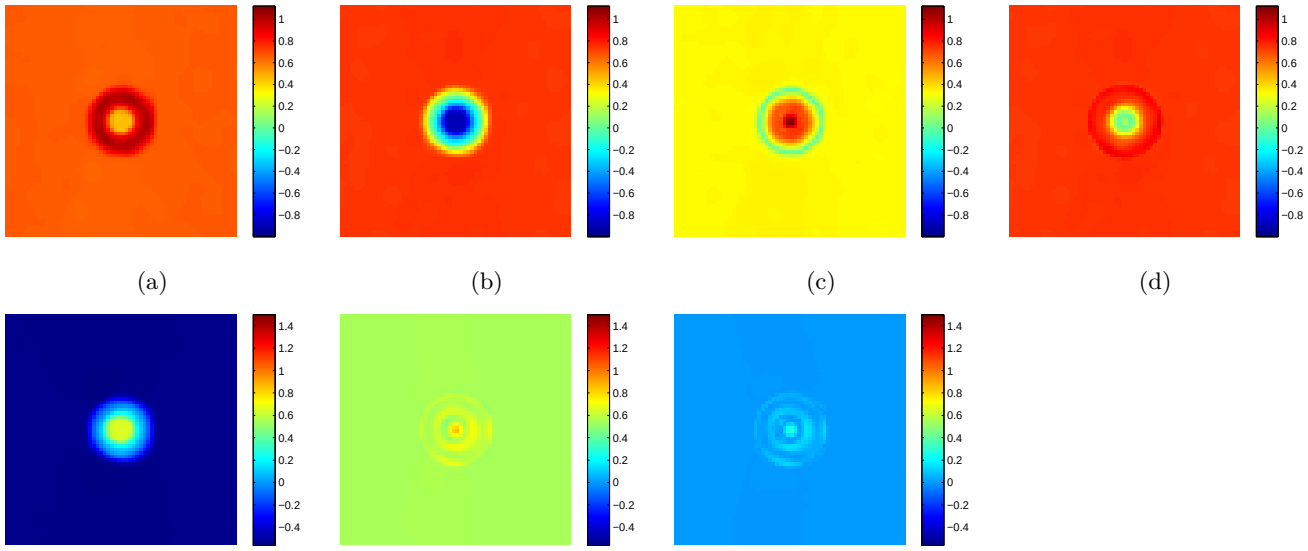

(a) (b) (c) (d)

(e) (f) (g)

Figure 4.9: Estimation of Gradient Descent method without projection, initial guess $u_{02} = \left(\frac{1}{\sqrt{2}}, i\frac{1}{\sqrt{2}}\right)$. (a) $\mathrm{Re}\{\hat{u}\}$, (b) $\mathrm{Im}\{\hat{u}\}$, (c) $\mathrm{Re}\{|\hat{u} - \check{u}|\}$, (d) $\mathrm{Im}\{|\hat{u} - \check{u}|\}$, (e) $\hat{\phi}$, (f) $\left|\hat{\phi} - \check{\phi}\right|$, (g) $\left|\check{\phi}_j - \hat{\phi}_j - \overline{\check{\phi} - \hat{\phi}}\right|$

We can conclude that the estimations, although not strictly good, are better for initial guess $u_{01} = (1, i0)$, which is equivalent to the initial guess of $\phi_0 = 0$ in section 3.5. This confirms to us the dependency on the initial guess for iterative algorithms.

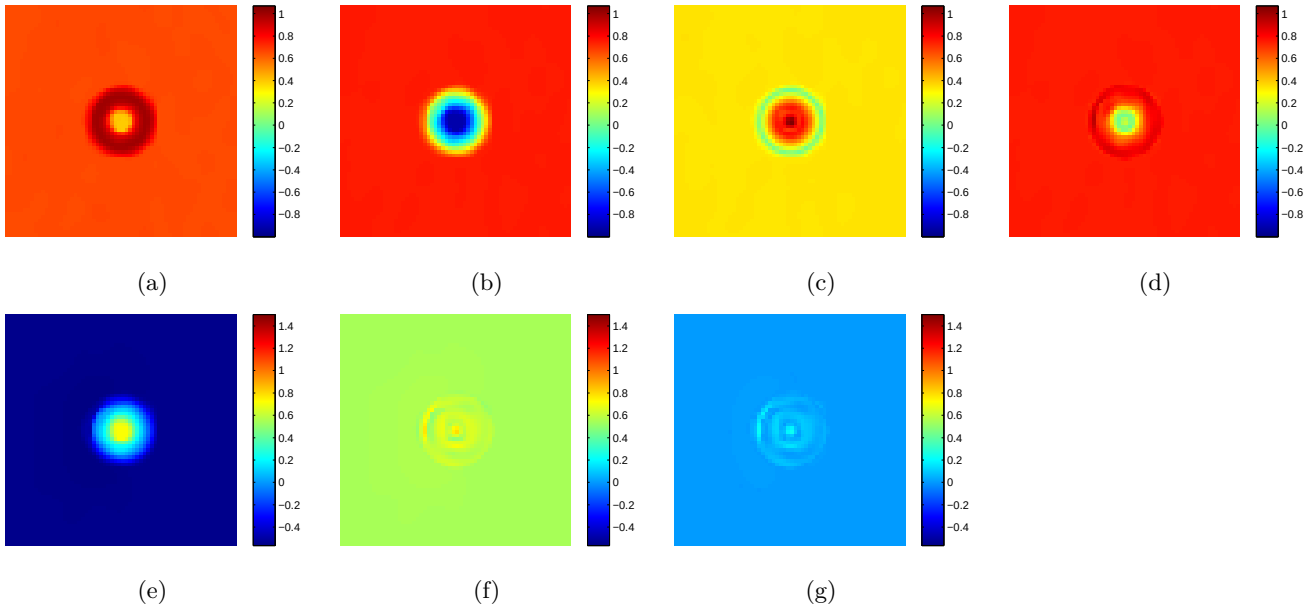

(a) (b) (c) (d)

(e) (f) (g)

Figure 4.10: Estimation of Gradient Descent method with projection, initial guess $u_{02} = \left(\frac{1}{\sqrt{2}}, i\frac{1}{\sqrt{2}}\right)$. (a) $\mathrm{Re}\{\hat{u}\}$, (b) $\mathrm{Im}\{\hat{u}\}$, (c) $\mathrm{Re}\{|\hat{u} - \check{u}|\}$, (d) $\mathrm{Im}\{|\hat{u} - \check{u}|\}$, (e) $\hat{\phi}$, (f) $\left|\hat{\phi} - \check{\phi}\right|$, (g) $\left|\check{\phi}_j - \hat{\phi}_j - \overline{\check{\phi} - \hat{\phi}}\right|$

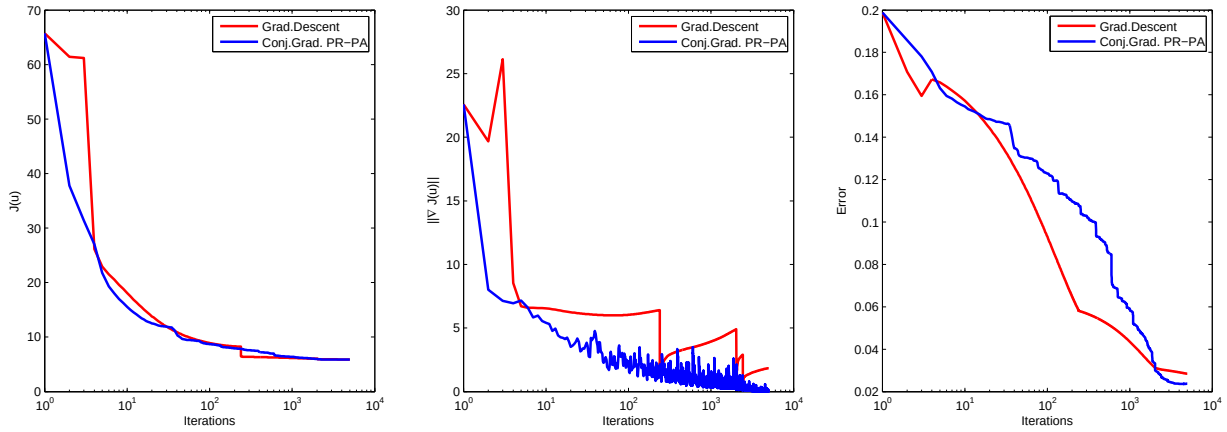

(a) (b) (c)

Figure 4.11: Methods comparison without projection, initial guess $u_{02} = \left(\frac{1}{\sqrt{2}}, i\frac{1}{\sqrt{2}}\right)$. (a) Convergence, (b) Norm of gradient, (c) Error

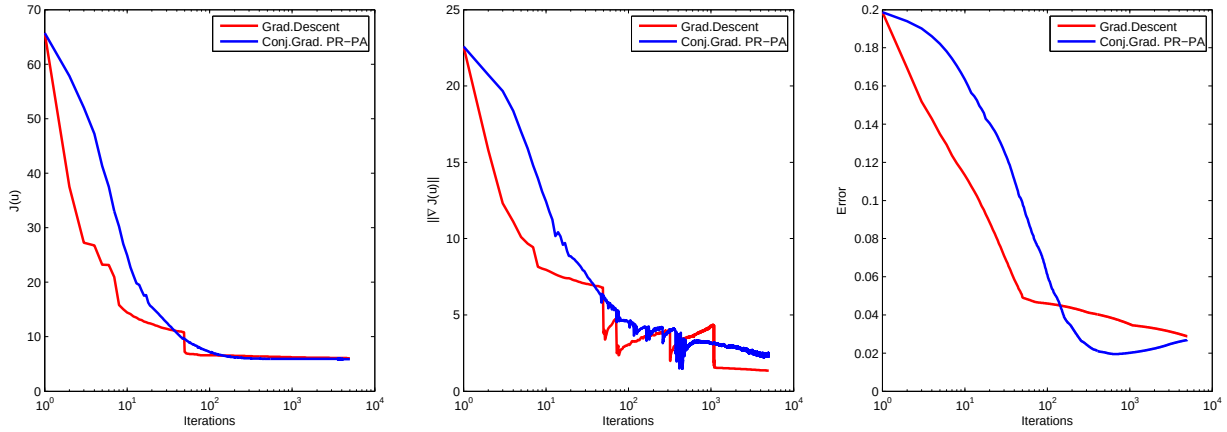

(a) (b) (c)

Figure 4.12: Methods comparison with projection, initial guess $u_{02} = \left(\frac{1}{\sqrt{2}}, i\frac{1}{\sqrt{2}}\right)$. (a) Convergence, (b) Norm of gradient, (c) Error

Now we proceed to do the same analysis for the cross object. Figure 4.14 presents the results without projection and Figure 4.16 with projection, both for initial guess $u_{01} = (1, i0)$. In Figure 4.13 we present the true cross object with color bars dynamic adjusted to the results for this initial guess without projection and in Figure 4.15 adjusted to the results with projection.

In general, we observe the same behavior as for the cone, in terms that the sharp shape is very well reconstructed, but the values of the specimen and phase functions are distant from the expected ones. In terms of the curves of performance of the algorithms, it is also more favorable the projection operator for the Gradient Descent method.

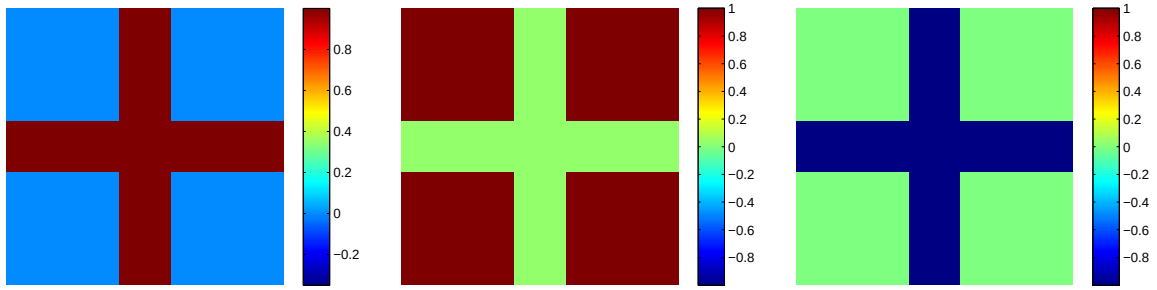

(a) (b) (c)

Figure 4.13: Cross object. True values for phase and specimen functions (a) Phase function $\check{\phi}$, (b) $\mathbb{R}e\{\check{u}\}$, (c) $\mathrm{Im}\{\check{u}\}$

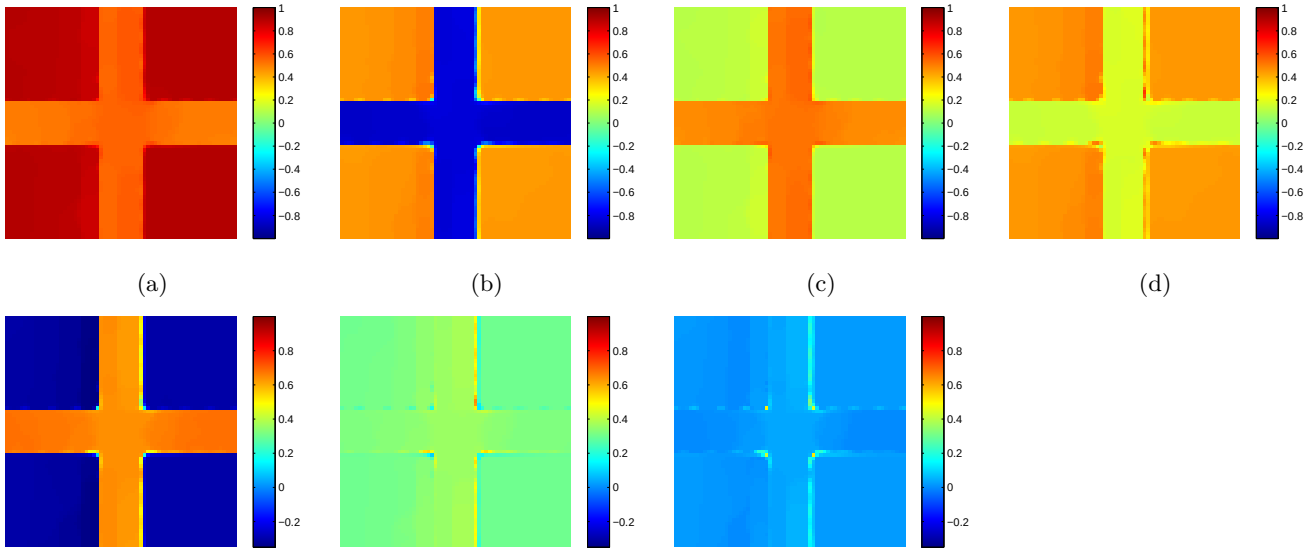

(a) (b) (c) (d)

(e) (f) (g)

Figure 4.14: Estimation of Gradient Descent method without projection, initial guess $u_{01} = (1, i0)$. (a) $\mathrm{Re}\{\hat{u}\}$, (b) $\mathrm{Im}\{\hat{u}\}$, (c) $\mathrm{Re}\{|\hat{u} - \check{u}|\}$, (d) $\mathrm{Im}\{|\hat{u} - \check{u}|\}$, (e) $\hat{\phi}$, (f) $\left|\hat{\phi} - \check{\phi}\right|$, (g) $\left|\check{\phi}_j - \hat{\phi}_j - \overline{\check{\phi} - \hat{\phi}}\right|$

In comparison with the cone, for the cross object using this initial guess, there is a considerable difference in the estimations according to the range of values for either the phase and the specimen, with respect to the use of the projection operator. It is also noticed that the values inside the bars are closer to the expected ones, specially for the imaginary part of the reconstructed $\hat{u}$; however it is not possible to achieve it for the background areas. With respect to the Conjugate Gradient PR-PA method with projection, there is a better estimation as can be observed in Figures D.13 and D.14.

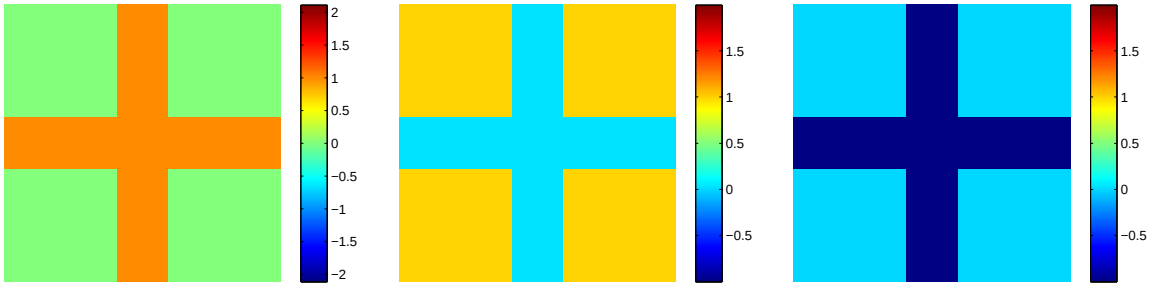

(a) (b) (c)

Figure 4.15: Cross object. True values for phase and specimen functions (a) Phase function $\check{\phi}$, (b) $\mathbb{R}e\{\check{u}\}$, (c) $\mathrm{Im}\{\check{u}\}$

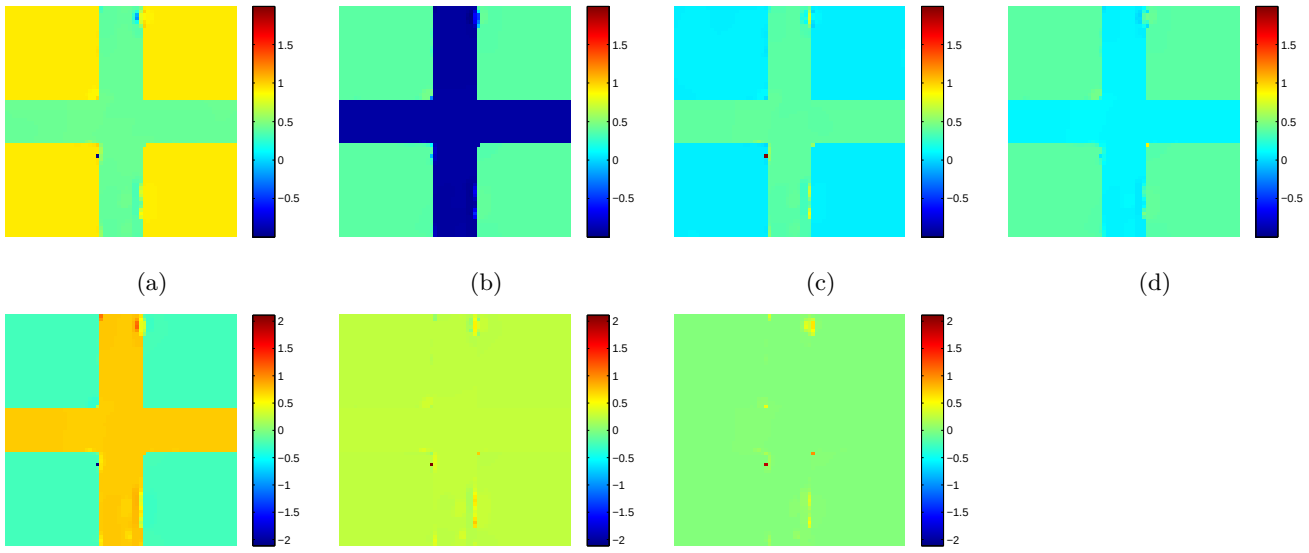

(a) (b) (c) (d)

(e) (f) (g)

Figure 4.16: Estimation of Gradient Descent method with projection, initial guess $u_{01} = (1, i0)$. (a) $\mathrm{Re}\{\hat{u}\}$, (b) $\mathrm{Im}\{\hat{u}\}$, (c) $\mathrm{Re}\{|\hat{u} - \check{u}|\}$, (d) $\mathrm{Im}\{|\hat{u} - \check{u}|\}$, (e) $\hat{\phi}$, (f) $\left|\hat{\phi} - \check{\phi}\right|$, (g) $\left|\check{\phi}_j - \hat{\phi}_j - \overline{\check{\phi} - \hat{\phi}}\right|$

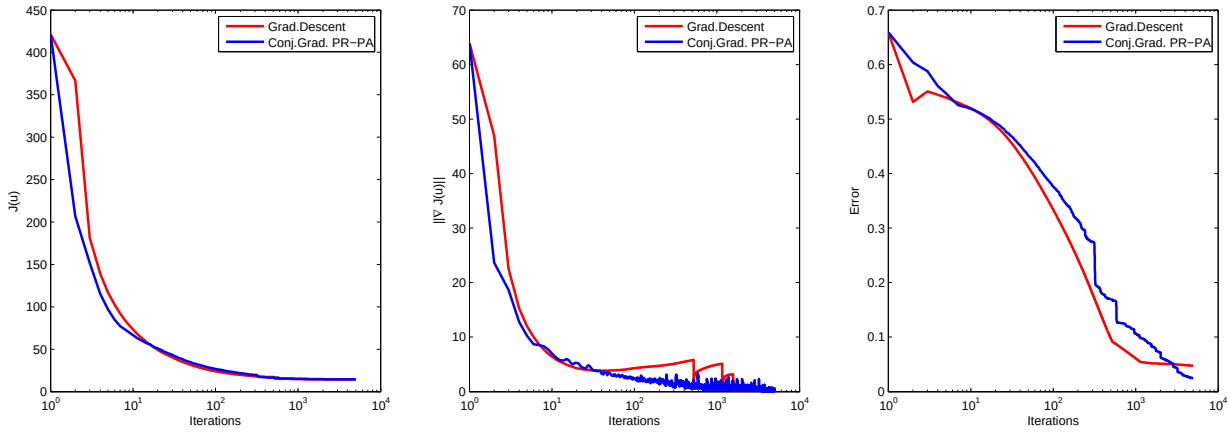

(a) (b) (c)

Figure 4.17: Methods comparison without projection, initial guess $u_{01} = (1, i0)$. (a) Convergence, (b) Norm of gradient, (c) Error

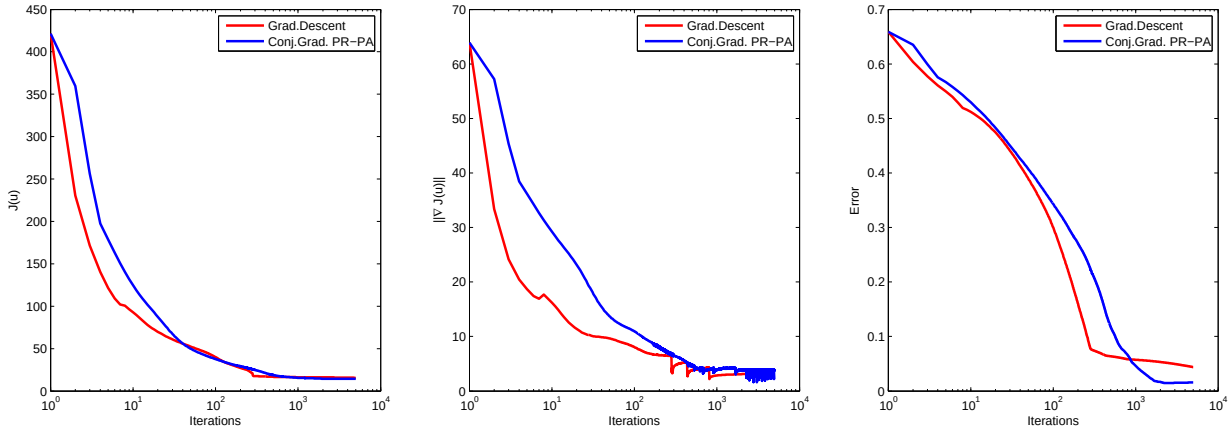

(a) (b) (c)

Figure 4.18: Methods comparison with projection, initial guess $u_{01} = (1, i0)$. (a) Convergence, (b) Norm of gradient, (c) Error

Figures 4.20 to 4.24 present the results when used initial guess $u_{02} = (\frac{1}{\sqrt{2}}, i\frac{1}{\sqrt{2}})$. Figure 4.19 shows the true values without projection and Figure 4.21 with projection, both with dynamic adjusted to this initial guess. It can be observed that as in the previous case, the estimations are affected by having or not the projection operator. However, for the Conjugate Gradient PR-PA method there was better estimation with the projection operator (see Figures D.19 and D.20).

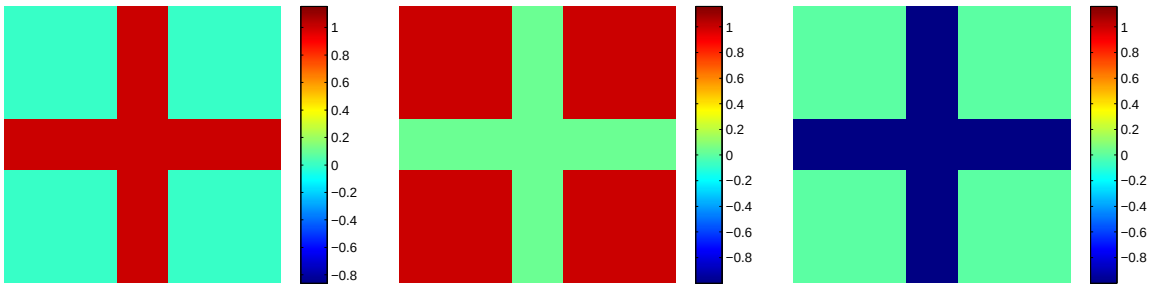

(a) (b) (c)

Figure 4.19: Cross object. True values for phase and specimen functions (a) Phase function $\check{\phi}$, (b) $\mathbb{R}e\{\check{u}\}$, (c) $\mathrm{Im}\{\check{u}\}$

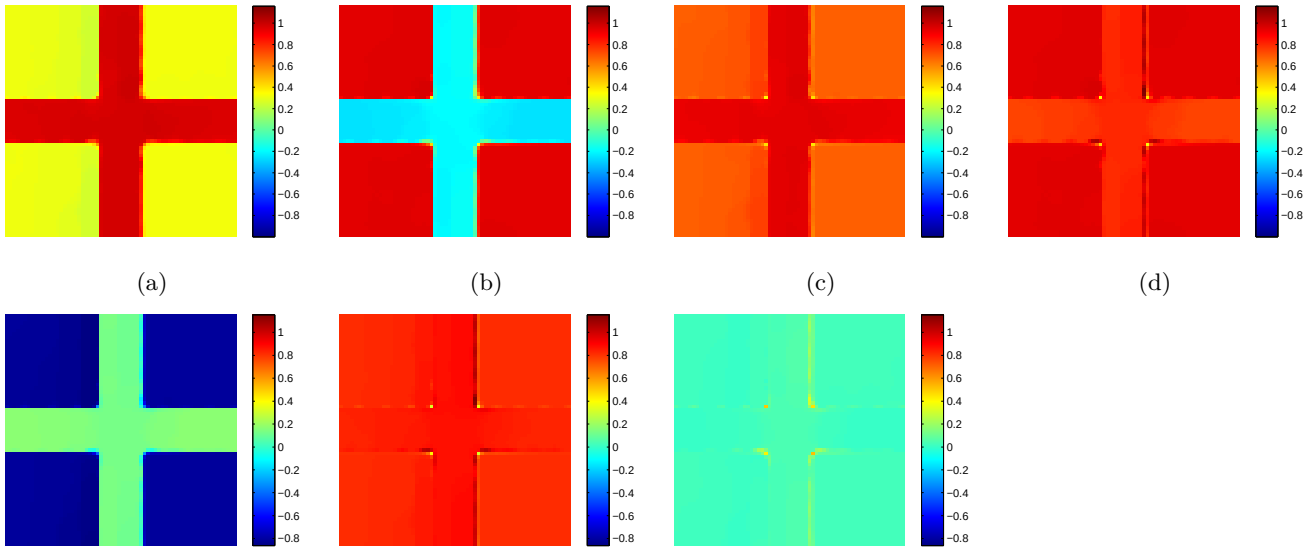

(a) (b) (c) (d)

(e) (f) (g)

Figure 4.20: Estimation of Gradient Descent method without projection, initial guess $u_{02} = (\frac{1}{\sqrt{2}}, i\frac{1}{\sqrt{2}})$. (a) $\mathrm{Re}\{\hat{u}\}$, (b) $\mathrm{Im}\{\hat{u}\}$, (c) $\mathrm{Re}\{|\hat{u} - \check{u}|\}$, (d) $\mathrm{Im}\{|\hat{u} - \check{u}|\}$, (e) $\hat{\phi}$, (f) $\left|\hat{\phi} - \check{\phi}\right|$, (g) $\left|\check{\phi}_j - \hat{\phi}_j - \overline{\check{\phi} - \hat{\phi}}\right|$

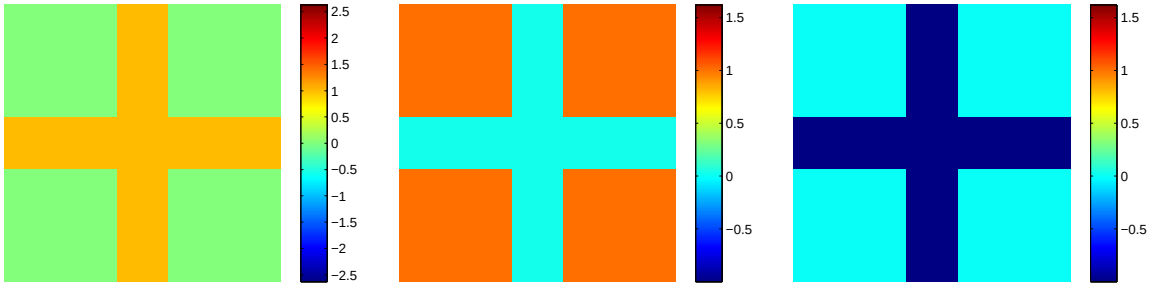

(a) (b) (c)

Figure 4.21: Cross object. True values for phase and specimen functions (a) Phase function $\check{\phi}$, (b) $\mathbb{R}e\{\check{u}\}$, (c) $\mathrm{Im}\{\check{u}\}$

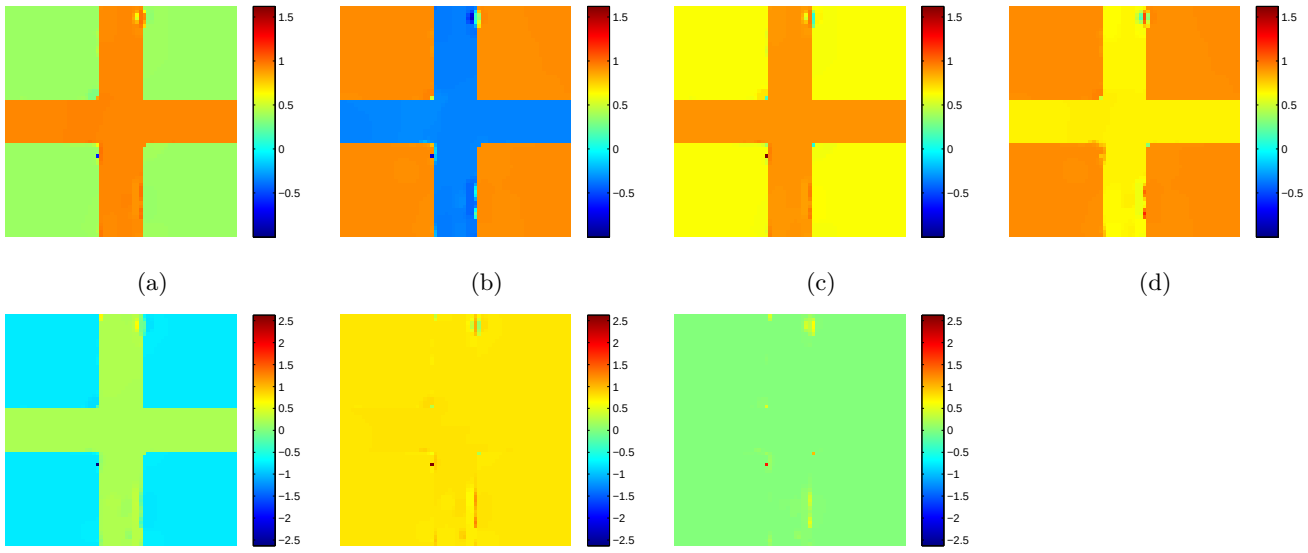

(a) (b) (c) (d)

(e) (f) (g)

Figure 4.22: Estimation of Gradient Descent method with projection, initial guess $u_{02} = (\frac{1}{\sqrt{2}}, i\frac{1}{\sqrt{2}})$. (a) $\mathrm{Re}\{\hat{u}\}$, (b) $\mathrm{Im}\{\hat{u}\}$, (c) $\mathrm{Re}\{|\hat{u} - \check{u}|\}$, (d) $\mathrm{Im}\{|\hat{u} - \check{u}|\}$, (e) $\hat{\phi}$, (f) $\left|\hat{\phi} - \check{\phi}\right|$, (g) $\left|\check{\phi}_j - \hat{\phi}_j - \overline{\check{\phi} - \hat{\phi}}\right|$

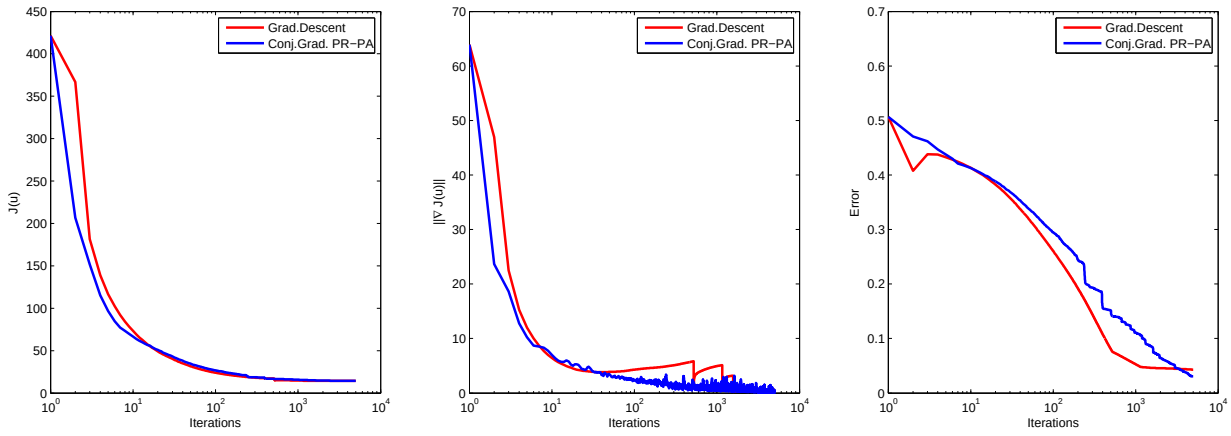

(a) (b) (c)

Figure 4.23: Methods comparison without projection. (a) Convergence, (b) Norm of gradient, (c) Error

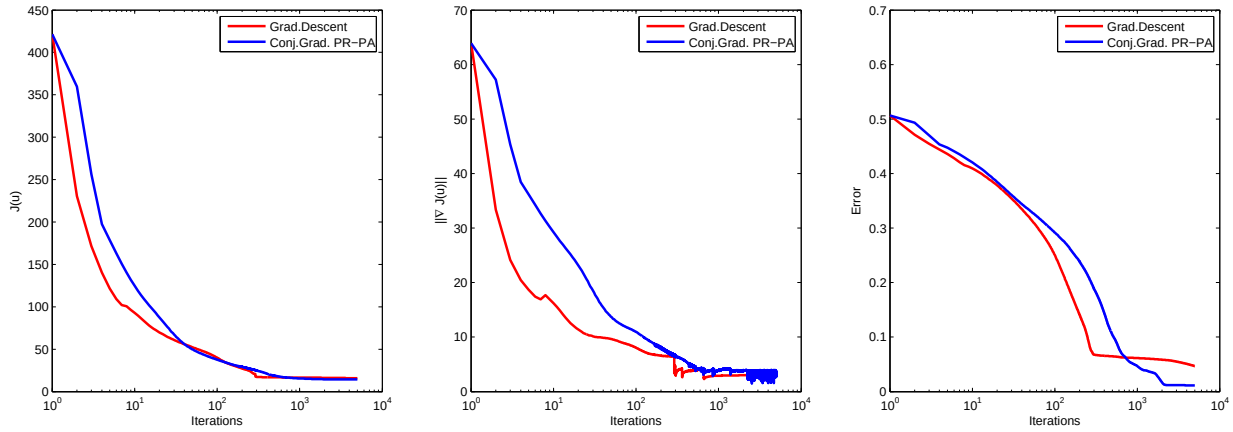

(a) (b) (c)

Figure 4.24: Methods comparison with projection. (a) Convergence, (b) Norm of gradient, (c) Error

In comparison to the results obtained for the unconstrained problem in section 3.5, the projected approach is not as efficient as it was expected. We could think that the constrained problem is more difficult to optimize and sensitive to the initial guess, leading the output to be stuck in a local minimum.

4.5 Towards uplifting the phase

Given the non-linearity and non-convexity of problem 4.20, we have considered the use of another novel approaches leading to the linearization of the problem. One of the most known methods in that direction, designed for the phase retrieval problem is the *PhaseLift* method proposed by Candès et al in [23], which we shortly described in section 3.1.3. We present the main principle in the abstract level.

Here we consider the problem of finding $u \in \mathbb{C}^n$, given a vector of observations $b_j \in \mathbb{R}$ such that

$$b_j = |\langle a_j, u\rangle|^2 \qquad \text{for } j = 1, ..., m; m \leq n$$

In the phase retrieval problem a_j is the vector of size n containing the j^{th} line of the Fourier transform matrix such that $\langle a_j, u\rangle$ is the j^{th} frequency of u. We have the quadratic measurements of the form $\mathbb{A}(u) = \left\{|\langle a_j, u\rangle|^2 : j = 1, ..., m\right\}$. Then, the phase retrieval problem is

$$\begin{aligned} &\text{find} && u \\ &\text{s.t.} && \mathbb{A}(u) = b \end{aligned} \tag{4.23}$$

which can be approached by the optimization problem

$$\min_{u\in\mathbb{C}^n} \|\mathbb{A}(u) - b\|^2 = \min_{u\in\mathbb{C}^n} \sum_{j=1}^{m} \left[|\langle a_j, u\rangle|^2 - b_j\right]^2 \tag{4.24}$$

Due to the square modulus in operator $\mathbb{A}$, this is a non-linear non-convex problem. The *PhaseLift* idea is to reformulate this quadratic measurements by lifting them up and interpreting them as linear measurements of the rank-one matrix $U = u\bar{u}$. This is based on the fact that we have

$$|\langle a_j, u\rangle|^2 = Tr(\bar{u}a_j a_j^* u) = Tr(a_j a_j^* u\bar{u}) := Tr(A_j U) \tag{4.25}$$

where A_j (respectively U) is the rank-one matrix $a_j a_j^*$ (respectively uu^*). Then the problem (4.25) can be reformulated as

$$\min_{\substack{U\in\mathbb{C}^n\times\mathbb{C}^n \\ U\succeq 0 \\ rank(U)=1}} \|\mathcal{A}(U) - b\|^2 = \min_{\substack{U\in\mathbb{C}^n\times\mathbb{C}^n \\ U\succeq 0 \\ rank(U)=1}} \sum_{j=1}^{m} \left(Tr(A_j U) - b_j\right)^2 \tag{4.26}$$

4.5.1 Application to the DIC problem

Our main concern is to reformulate the original DIC phase estimation problem (4.5), as a phase retrieval problem in order to apply *PhaseLift* to it. We start by considering first problem (4.2)

$$\min_{u\in\mathbb{C}^{MP},\,|u_j|=1} J_0(u) = \sum_{k=1}^{K}\sum_{j\in\chi}\left[(o_k)_j - \left|(h_k \otimes u)_j\right|^2\right]^2$$

which can be rewritten as follows

$$\begin{aligned}\min_{u\in\mathbb{C}^{MP},\,|u_j|=1} J_0(u) &= \sum_{k=1}^{K}\sum_{j\in\chi}\left[(o_k)_j - \left|(H_k \cdot u)_j\right|^2\right]^2 \\ &= \sum_{k=1}^{K}\sum_{j\in\chi}\left[(o_k)_j - \left|\langle H_{k_j}, u_j\rangle\right|^2\right]^2\end{aligned} \tag{4.27}$$

where H_{k_j} is the MP $\times$ 1 vector containing the j^{th} line of matrix H_k. Then the problem (4.27) can be reformulated as in (4.26):

$$\min_{\substack{U\in\mathbb{C}^{MP}\times\mathbb{C}^{MP} \\ rank(U)=1 \\ U\succeq 0 \\ U_{ii}=1,\forall j}} \sum_{k=1}^{K}\|\mathcal{H}_k(U) - b\|^2 = \min_{\substack{U\in\mathbb{C}^{MP}\times\mathbb{C}^{MP} \\ rank(U)=1 \\ U\succeq 0 \\ U_{ii}=1,\forall j}} \sum_{k=1}^{K}\sum_{j\in\chi}\left(Tr(\tilde{H}_{k_j}U) - b_j\right)^2 \tag{4.28}$$

where $\tilde{H}_{k_j} = H_{k_j} \cdot H_{k_j}^*$. Problem (4.28) can be also written as

$$\begin{aligned}\min_{U\in\mathbb{C}^{MP}\times\mathbb{C}^{MP}} &\sum_{k=1}^{K}\|\mathcal{H}_k(U) - b\|^2 + \mathbb{1}_{\{X\in\mathbb{C}^{MP}\times\mathbb{C}^{MP}/rank(X)\leq 1\}}(U) + \\ &\mathbb{1}_{\{X\in\mathbb{C}^{MP}\times\mathbb{C}^{MP}/X\succeq 0\}}(U) + \mathbb{1}_{\{X\in\mathbb{C}^{MP}\times\mathbb{C}^{MP}/X_{ii}=1\}}(U)\end{aligned} \tag{4.29}$$

This is a low-rank matrix optimization problem, also known as semi-definite problem (SDP), on which the non-convex constraint $|u_j| = 1$ is now linearized. We plan to use recent results on low-rank optimization obtained in [24]. In this work, the author proposes results on convexifica-

tion of low-rank matrix estimation problem, as well as numerical ways to compute the proximal operator of this term. Such results will be useful to solve the more complex problem (4.29).

4.6 Summary

In this chapter we provided a constrained formulation for the DIC phase estimation problem. We proposed a change of variable for the objective variable, transforming the search space from $\mathbb{R}^{MP}$ to $\mathbb{C}^{MP}$. We made use of the Wirtinger derivatives in order to implement the computation of the gradient for the iterative algorithms, maintaining the compact and fast calculation of it.

The change of variable obliged us to impose a module 1 constraint and with this we could introduce a projection operator which was implemented into the LMSD and Conjugate Gradient PR-PA algorithms already discussed in section 3.4. Because of the change of variable, most of the properties described in section 3.2 were lost. We could observe numerically that the methods behave slow and less accurate in retrieving the phase.

In order to overcome this drawback, we propose as future work to make use of more challenging methods like the *PhaseLift* algorithm which can deal better with the non-convexity of the optimization problem in the objective variable.

Chapter 5

Conclusions and Future Work

The goal of this dissertation was to provide efficient methods for the phase estimation problem in Differential Interference Contrast (DIC) microscopy. We made emphasis in three aspects: *1*, the definition of an image formation model having into account polychromatic light; *2*, phase retrieval algorithms based on regularized inversion that offer accuracy and stability in the estimation; *3*, a constrained approximation approach by changing the search space and imposing certain structure to the estimation. In the following we discuss the results we obtained, contributions and suggestions for future work.

5.1 The polychromatic image formation model

In chapter 2 a polychromatic image formation model was originated as an extension of the well known Rotational diversity model proposed by Preza et al in [72]. We had into account properties of partially coherent and polarized light that produce the inteference phenomena, which is the main optical principle that produces the images in a DIC microscope. We studied the characteristics of the image formation model in terms of the interaction of the RGB wavelengths and how they adjust the quality of resolution in addition to the numerical aperture of the microscope. For that we presented a detailed analysis of the different configurations of the point spread function (PSF), under the influence of parameters such as shear direction, shear angle and bias retardation.

5.2 Regularized inversion for phase reconstruction

In chapter 3, we focused first on the theoretical properties of the non-linear and non-convex inverse problem of DIC phase estimation. We stated and proved its periodicity, shift–invariance and analyticity, as well as the existence of minimum points when an edge–preserving regularizer is introduced. That allowed us to explore from the practical point of view, the use of efficient optimization methods such as LMSD (smoothed functional) and ILA (non-smoothed functional). We were able to compare their performance with state–of–the–art algorithms such as Conjugate Gradient with its variants of Fletcher-Reeves, Polak-Ribiere and Polynomial Approximation. We made special attention to the fast and compact computation of the gradient compared to the one that was previously reported on the literature. This work has been made in collaboration with colleagues at the University of Modena and Reggio Emilia in Italy; as a result, a paper is in second review at the Inverse Problems Journal.

5.3 Constrained approximation

In an attempt to manage differently the non-linearity and non-convexity of this inverse problem, in chapter 4 we proposed a different approach by including a non-convex constraint to the original problem. We transformed the optimization space from $\mathbb{R}^{\mathrm{MP}}$ to $\mathbb{C}^{\mathrm{MP}}$ which imposed a different structure to the problem. This also meant that some of the properties found in chapter 3 were not maintained under the new inverse problem. We followed again the regularized inversion approach adjusted for the new structure and we compared the performance of a gradient descent method versus a conjugate gradient method.

5.4 Future work

We think that an interesting alternative way to solve the DIC phase reconstruction problem is to build an algorithm able to compute the reformulated *PhaseLift* problem, as it was presented in (4.29). It is also recommended to use the results presented in [24], on convexification of low-rank matrix approximation, as well as numerical algorithms to solve the associated proximal operator.

It is important to make a validation of the methods we have proposed using experimental images. Along the development of this dissertation we did acquisitions in collaboration with the Laboratory of Microscopy at the Universidad Industrial de Santander (UIS) in Colombia. We used a Carl Zeiss Axio Imager z1 microscope, equipped with a technique called C-DIC (stands for Circular-DIC), which works under circularly polarized light and in reflection mode (not in transmission like the model we presented in Chapter 2). The main difficulty that this imposed in our approach was that the acquired images could not be represented accurately by the model we proposed. For this, we value to continue with a very close collaboration with the physicists at UIS, in order to reconsider the image formation model from a deeper optical point of view of the microscopy system.

Appendices

Appendix A

PSF for shear angle in $\{0, \pi/2\}$

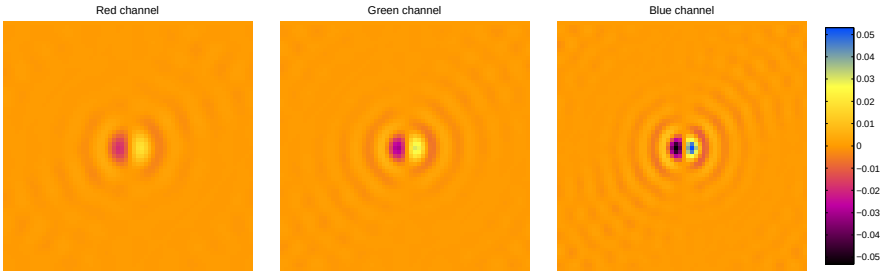

(a) Real$\{h_{1,\lambda_\ell}(x, y)\}$; $\tau_1 = 0$

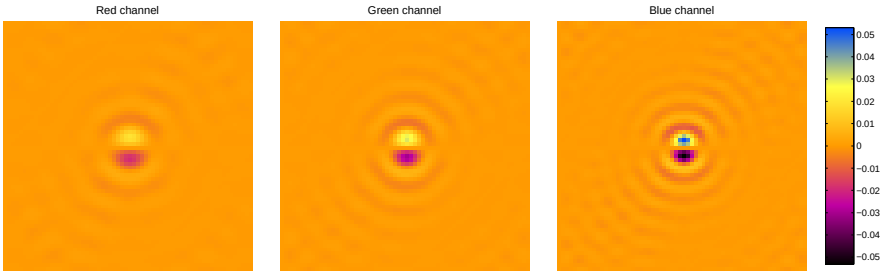

(b) Real$\{h_{2,\lambda_\ell}(x, y)\}$; $\tau_2 = \pi/2$

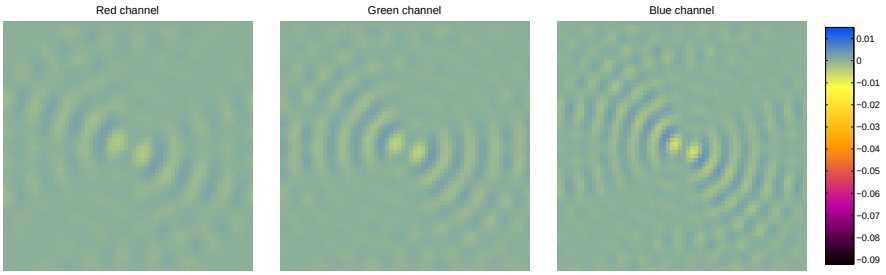

(c) Imag$\{h_{1,\lambda_\ell}(x, y)\}$; $\tau_1 = 0$

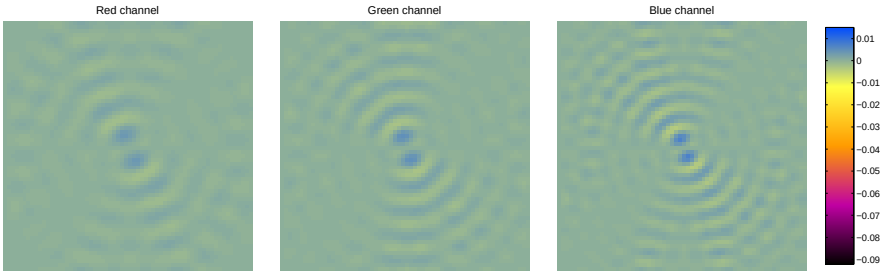

(d) Imag$\{h_{2,\lambda_\ell}(x, y)\}$; $\tau_2 = \pi/2$

Figure A.1: Effect of shear angle, bias retardation and wavelength values on polychromatic PSF. Case 1: $2\Delta\theta_1 = 0$

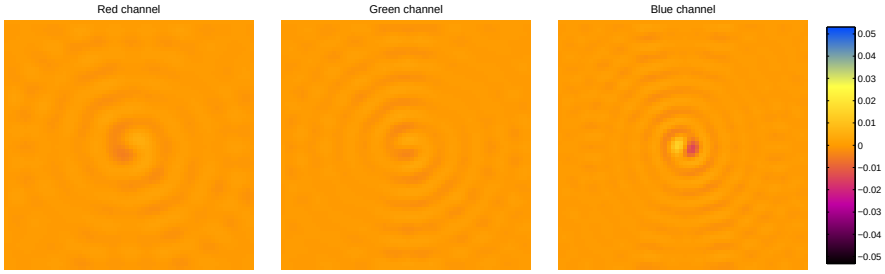

(a) Real$\{h_{1,\lambda_\ell}(x, y)\}$; $\tau_1 = 0$

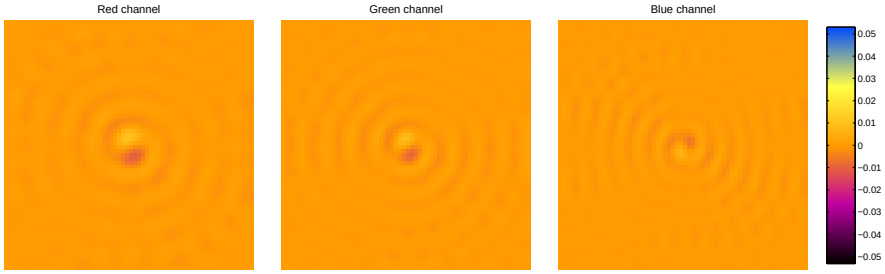

(b) Real$\{h_{2,\lambda_\ell}(x, y)\}$; $\tau_2 = \pi/2$

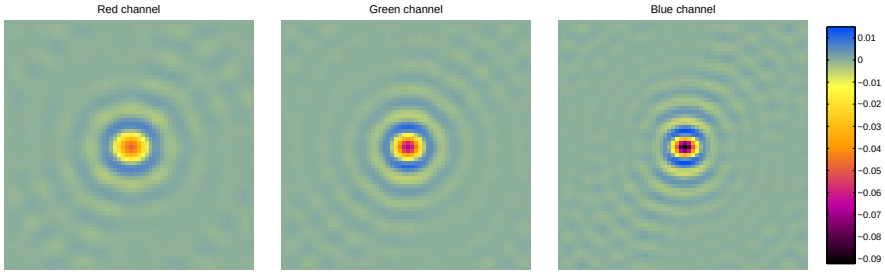

(c) Imag$\{h_{1,\lambda_\ell}(x, y)\}$; $\tau_1 = 0$

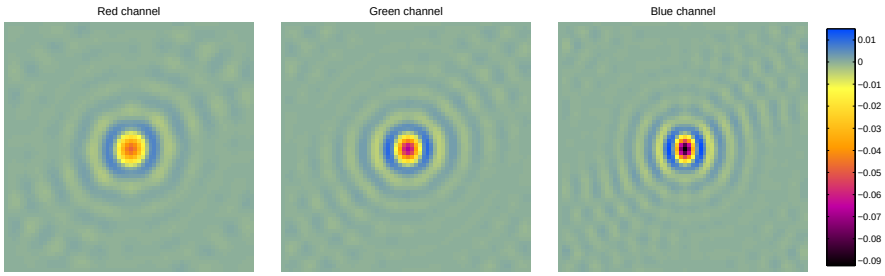

(d) Imag$\{h_{2,\lambda_\ell}(x, y)\}$; $\tau_2 = \pi/2$

Figure A.2: Effect of shear angle, bias retardation and wavelength values on polychromatic PSF. Case 1: $2\Delta\theta_2 = \pi/2$

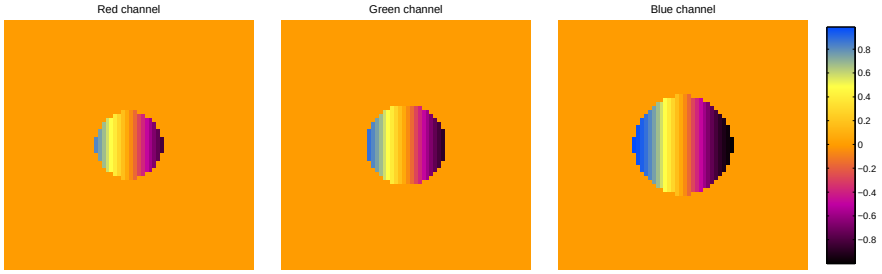

(a) Imag$\{H_{1,\lambda_\ell}(m,n)\}$; $\tau_1 = 0$

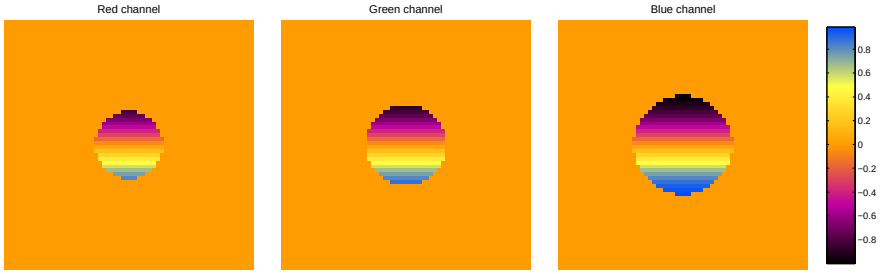

(b) Imag$\{H_{2,\lambda_\ell}(m,n)\}$; $\tau_2 = \pi/2$

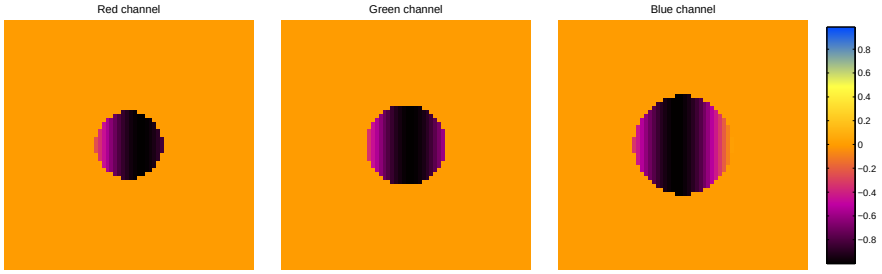

(c) Imag$\{H_{1,\lambda_\ell}(m,n)\}$; $\tau_1 = 0$

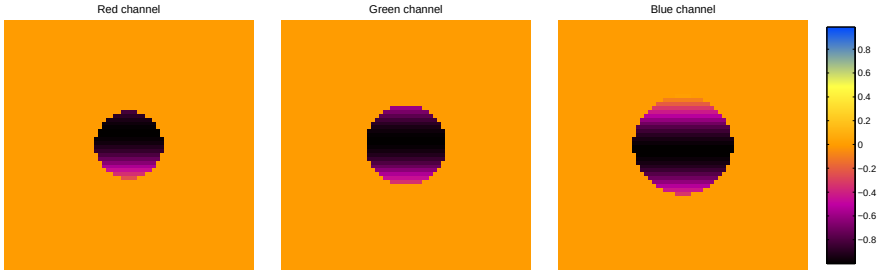

(d) Imag$\{H_{2,\lambda_\ell}(m,n)\}$; $\tau_2 = \pi/2$

Figure A.3: Frequency domain support of polychromatic PSF. (a)-(b) $2\Delta\theta_1 = 0$; (c)-(d) $2\Delta\theta_2 = \pi/2$

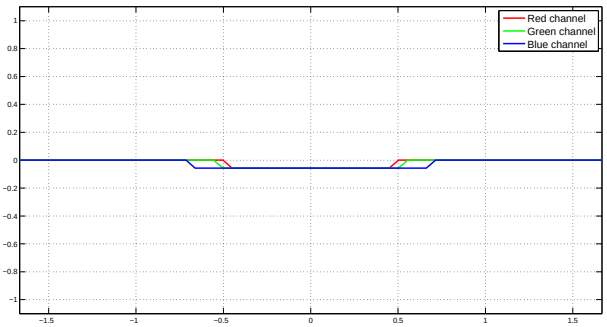

(a) Imag$\{H_{1,\lambda_\ell}(m,0)\}$; $\tau_1 = 0$

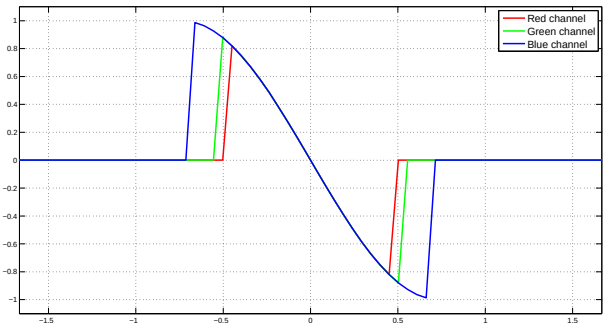

(b) Imag$\{H_{1,\lambda_\ell}(0,m)\}$; $\tau_1 = 0$

Figure A.4: Vertical and horizontal profiles of polychromatic PSF. $2\Delta\theta_1 = 0$

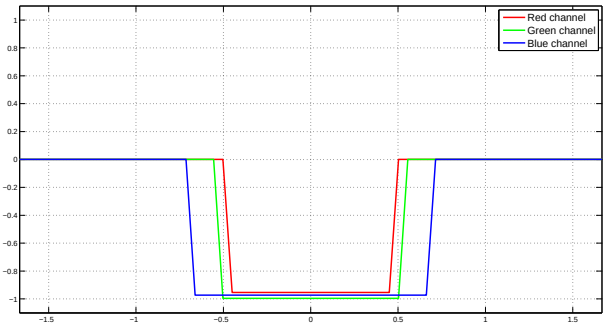

(a) Imag$\{H_{1,\lambda_\ell}(m,0)\}$; $\tau_1 = 0$

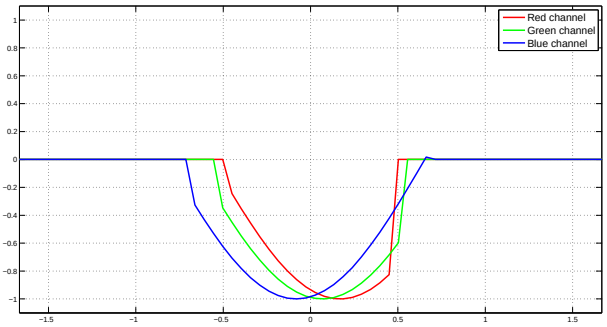

(b) Imag$\{H_{1,\lambda_\ell}(0,m)\}$; $\tau_1 = 0$

Figure A.5: Vertical and horizontal profiles of polychromatic PSF. $2\Delta\theta_2 = \pi/2$

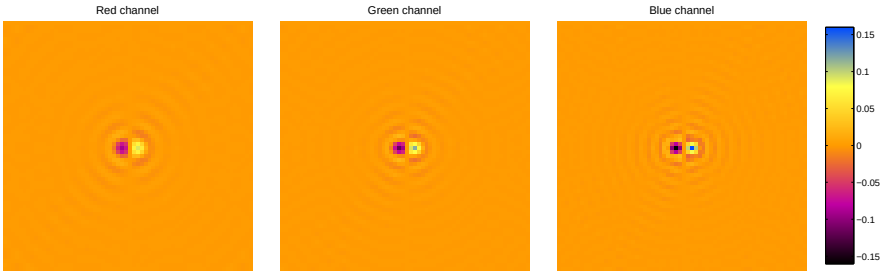

(a) Real$\{h_{1,\lambda_\ell}(x,y)\}$; $\tau_1 = 0$

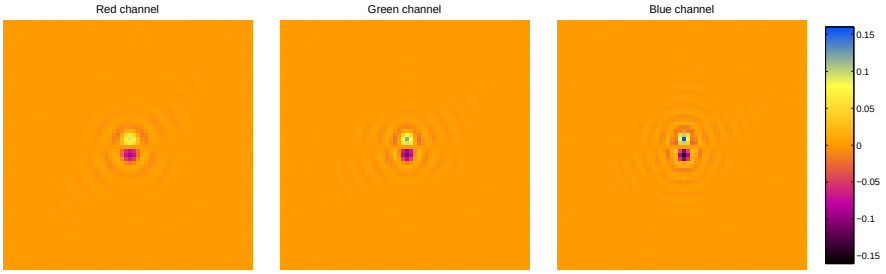

(b) Real$\{h_{2,\lambda_\ell}(x,y)\}$; $\tau_2 = \pi/24$

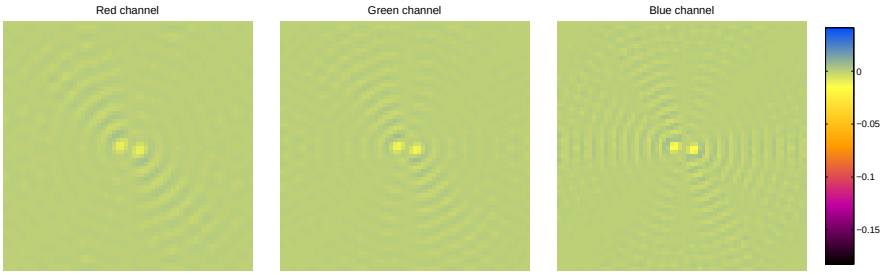

(c) Imag$\{h_{1,\lambda_\ell}(x,y)\}$; $\tau_1 = 0$

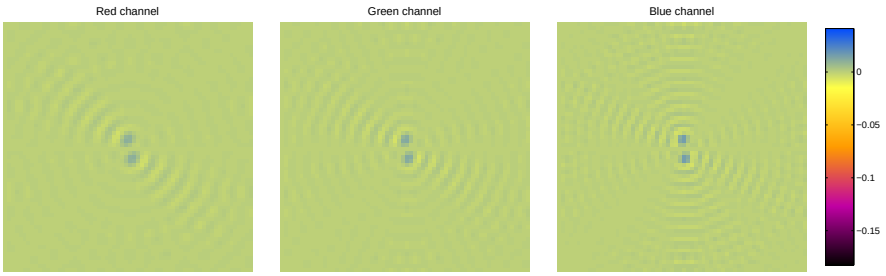

(d) Imag$\{h_{2,\lambda_\ell}(x,y)\}$; $\tau_2 = \pi/2$

Figure A.6: Effect of NA $= 0.9$ on polychromatic PSF. Case 1: $2\Delta\theta_1 = 0$

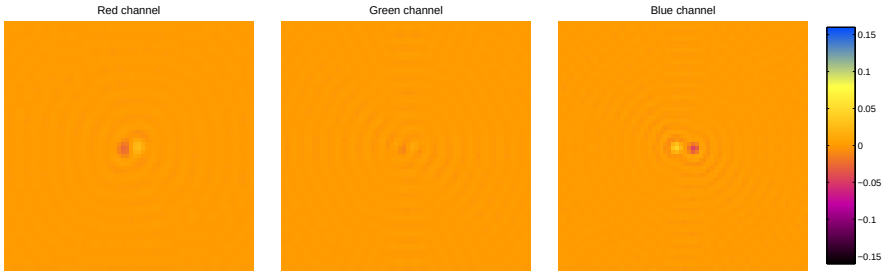

(a) Real$\{h_{1,\lambda_\ell}(x, y)\}$; $\tau_1 = 0$

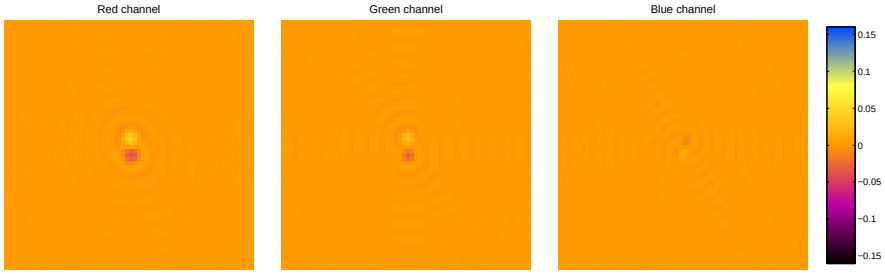

(b) Real$\{h_{2,\lambda_\ell}(x, y)\}$; $\tau_2 = \pi/2$

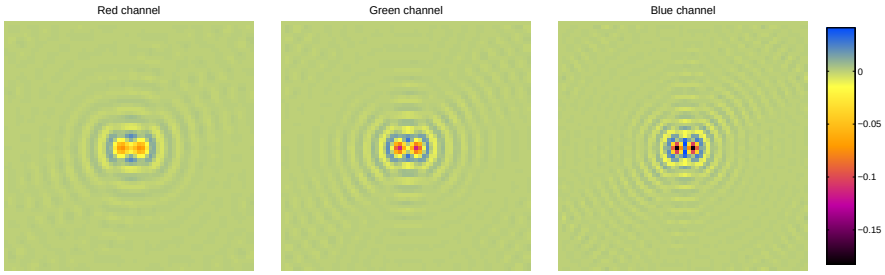

(c) Imag$\{h_{1,\lambda_\ell}(x, y)\}$; $\tau_1 = 0$

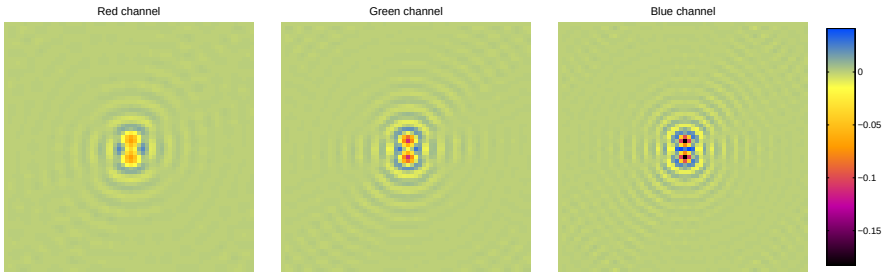

(d) Imag$\{h_{2,\lambda_\ell}(x, y)\}$; $\tau_2 = \pi/2$

Figure A.7: Effect of NA $= 0.9$ on polychromatic PSF. Case 1: $2\Delta\theta_2 = \pi/2$

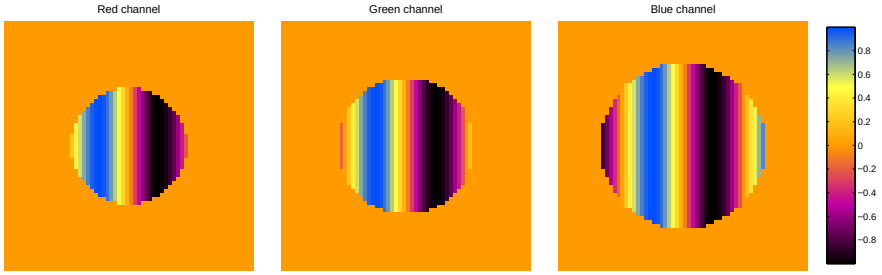

(a) Imag$\{H_{1,\lambda_\ell}(m,n)\}$; $\tau_1 = 0$

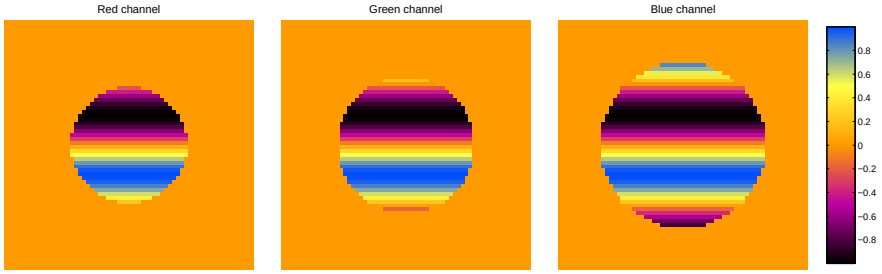

(b) Imag$\{H_{2,\lambda_\ell}(m,n)\}$; $\tau_2 = \pi/2$

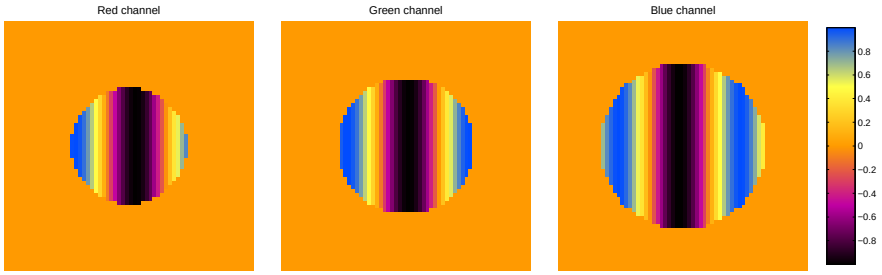

(c) Imag$\{H_{1,\lambda_\ell}(m,n)\}$; $\tau_1 = 0$

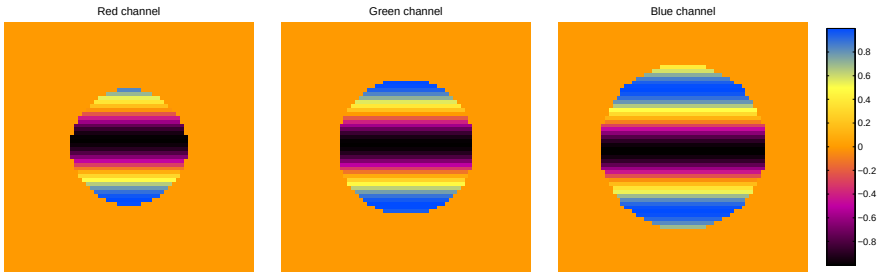

(d) Imag$\{H_{2,\lambda_\ell}(m,n)\}$; $\tau_2 = \pi/2$

Figure A.8: Frequency domain support of polychromatic PSF. (a)-(b) $2\Delta\theta_1 = 0$; (c)-(d) $2\Delta\theta_2 = \pi/2$

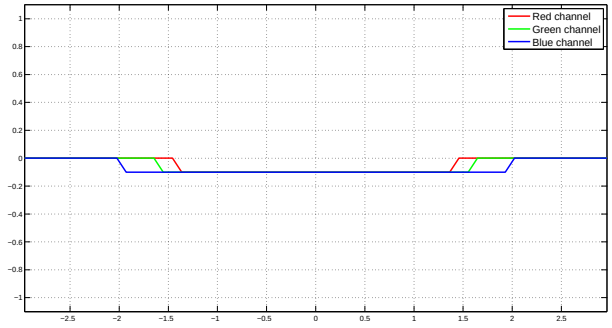

(a) Imag$\{H_{1,\lambda_\ell}(m,0)\}$; $\tau_1 = 0$

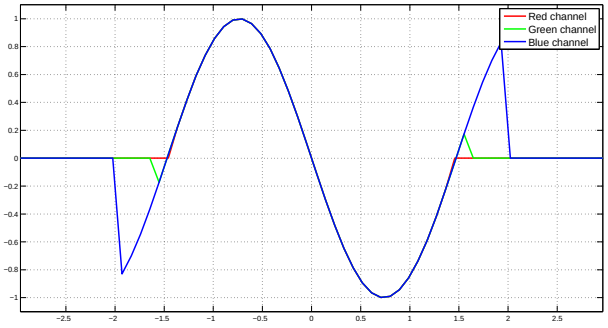

(b) Imag$\{H_{1,\lambda_\ell}(0,m)\}$; $\tau_1 = 0$

Figure A.9: Vertical and horizontal profiles of polychromatic PSF. $2\Delta\theta_1 = 0$

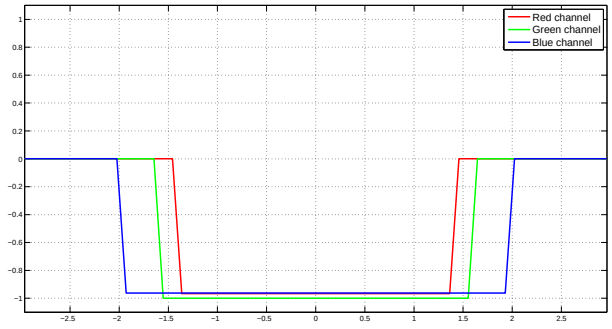

(a) Imag$\{H_{1,\lambda_\ell}(m,0)\}$; $\tau_1 = 0$

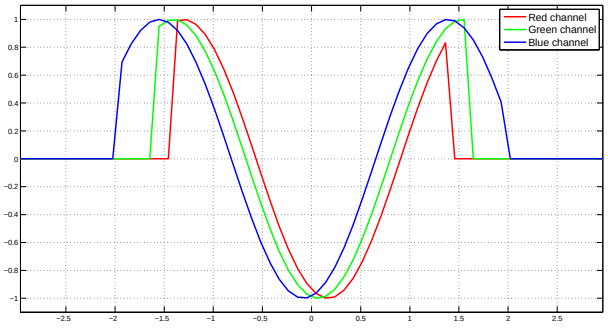

(b) Imag$\{H_{1,\lambda_\ell}(0,m)\}$; $\tau_1 = 0$

Figure A.10: Vertical and horizontal profiles of polychromatic PSF. $2\Delta\theta_2 = \pi/2$

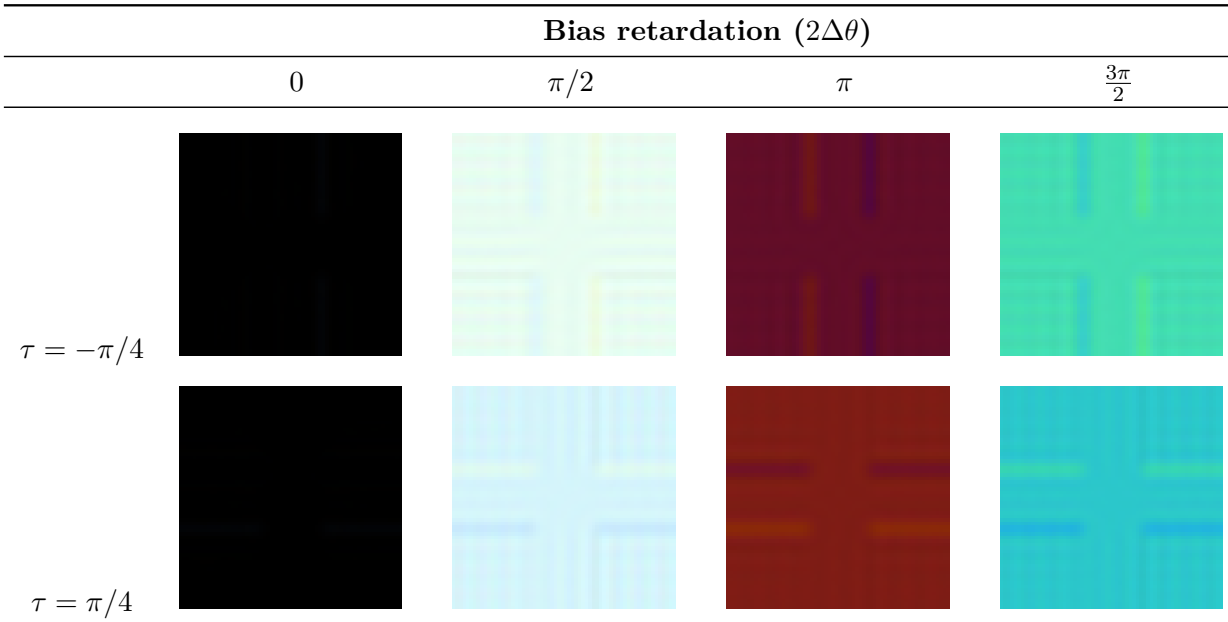

Figure A.11: Observed DIC images for different combinations of shear angle and bias retardation. NA = 0.3

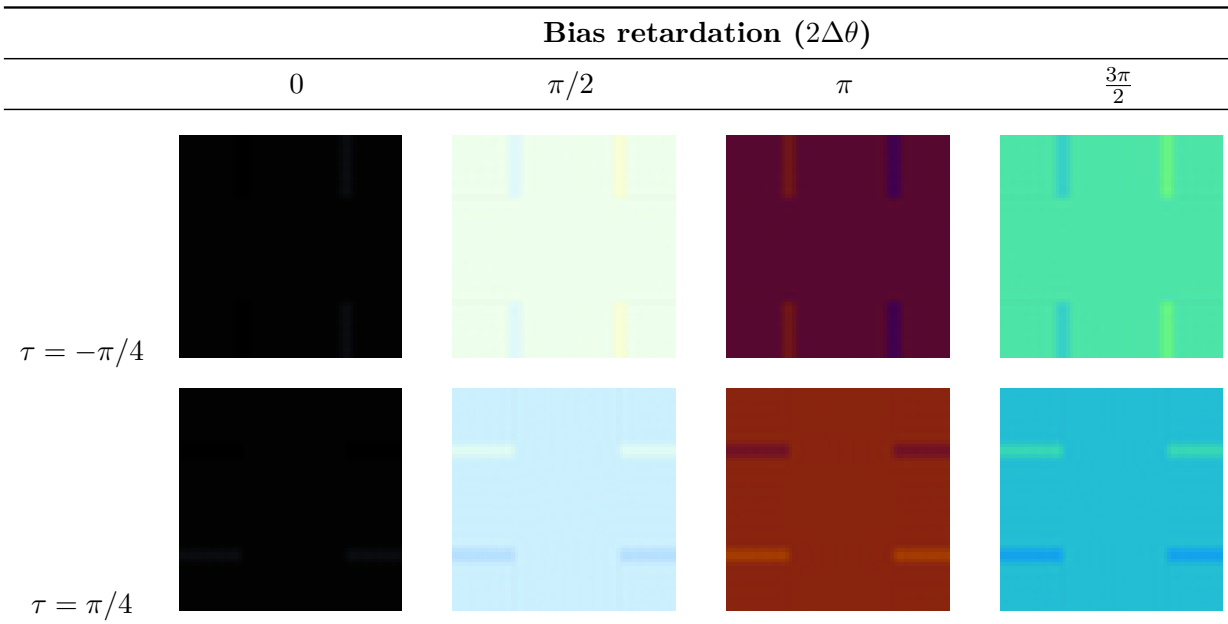

Figure A.12: Observed DIC images for different combinations of shear angle and bias retardation. NA = 0.9

Appendix B

Gradient and Hessian of $J_0(\phi)$

B.1 Gradient of $J_0(\phi)$

Here is the complete calculation of the gradient of functional (3.1) with respect to an element ϕ_s, for all $s \in \chi$.

$$J_0(\phi) = \sum_{\ell=1}^{3}\sum_{k=1}^{K}\sum_{j\in\chi}\left[(o_{k,\lambda_\ell})_j - \left|(h_{k,\lambda_\ell}\otimes e^{-i\phi/\lambda_\ell})_j\right|^2\right]^2$$

$$\frac{\partial J_0(\phi)}{\partial \phi_s} = \sum_{\ell=1}^{3}\sum_{k=1}^{K}\sum_{j\in\chi} 2\left[\left|(h_{k,\lambda_\ell}\otimes e^{-i\phi/\lambda_\ell})_j\right|^2 - (o_{k,\lambda_\ell})_j\right]\frac{\partial\left|(h_{k,\lambda_\ell}\otimes e^{-i\phi/\lambda_\ell})_j\right|^2}{\partial\phi_s}$$

$$\frac{\partial\left|(h_{k,\lambda_\ell}\otimes e^{-i\phi/\lambda_\ell})_j\right|^2}{\partial\phi_s} = 2\ \mathrm{Re}\left[\overline{(h_{k,\lambda_\ell}\otimes e^{-i\phi/\lambda_\ell})_j}\cdot\frac{\partial(h_{k,\lambda_\ell}\otimes e^{-i\phi/\lambda_\ell})_j}{\partial\phi_s}\right]$$

$$\frac{\partial(h_{k,\lambda_\ell}\otimes e^{-i\phi/\lambda_\ell})_j}{\partial\phi_s} = \frac{\partial}{\partial\phi_s}\left(\sum_{m\in\chi}(h_{k,\lambda_\ell})_{j-m}e^{-i\phi_m/\lambda_\ell}\right) = -\frac{i}{\lambda_\ell}e^{-i\phi_s/\lambda_\ell}(h_{k,\lambda_\ell})_{j-s}$$

$$\frac{\partial\left|(h_{k,\lambda_\ell}\otimes e^{-i\phi/\lambda_\ell})_j\right|^2}{\partial\phi_s} = \frac{2}{\lambda_\ell}\ \mathrm{Re}\left[(h_{k,\lambda_\ell}\otimes e^{-i\phi/\lambda_\ell})_j\cdot(h_{k,\lambda_\ell})_{j-s}\cdot(-i)e^{-i\phi_s/\lambda_\ell}\right]$$

$$= \frac{2}{\lambda_\ell}\ \mathrm{Im}\left[\overline{(h_{k,\lambda_\ell}\otimes e^{-i\phi/\lambda_\ell})_j}\cdot(h_{k,\lambda_\ell})_{j-s}\cdot e^{-i\phi_s/\lambda_\ell}\right]$$

$$\frac{\partial J_0(\phi)}{\partial\phi_s} = \sum_{\ell=1}^{3}\sum_{k=1}^{K}\sum_{j\in\chi} 2\left[\left|(h_{k,\lambda_\ell}\otimes e^{-i\phi/\lambda_\ell})_j\right|^2 - (o_{k,\lambda_\ell})_j\right]\cdot\frac{2}{\lambda_\ell}\ \mathrm{Im}\left[\overline{(h_{k,\lambda_\ell}\otimes e^{-i\phi/\lambda_\ell})_j}\cdot(h_{k,\lambda_\ell})_{j-s}\cdot e^{-i\phi_s/\lambda_\ell}\right]$$

$$= \sum_{\ell=1}^{3}\sum_{k=1}^{K}\sum_{j\in\chi}\frac{4}{\lambda_\ell}\left[\left|(h_{k,\lambda_\ell}\otimes e^{-i\phi/\lambda_\ell})_j\right|^2 - (o_{k,\lambda_\ell})_j\right]\cdot\mathrm{Im}\left[\overline{(h_{k,\lambda_\ell}\otimes e^{-i\phi/\lambda_\ell})_j}\cdot(h_{k,\lambda_\ell})_{j-s}\cdot e^{i\phi_s/\lambda_\ell}\right] \tag{B.1}$$

Equation (B.1) corresponds to Equation (3.8) in subsection 3.2.3. This can be rewritten as

$$\frac{\partial J_0(\phi)}{\partial\phi_s} = \sum_{\ell=1}^{3}\sum_{k=1}^{K}\frac{4}{\lambda_\ell}\mathrm{Im}\left\{\left((r_{k,\lambda_\ell}.*(\overline{h_{k,\lambda_\ell}}\otimes e^{i\phi/\lambda_\ell}))\otimes\tilde{h}_{k,\lambda_\ell}\right)_s e^{-i\phi_s/\lambda_\ell}\right\}, \tag{B.2}$$

where $r_{k,\lambda_\ell} = \left[\left|(h_{k,\lambda_\ell}\otimes e^{-i\phi/\lambda_\ell})\right|^2 - o_{k,\lambda_\ell}\right]$; $\mathrm{Im}(\cdot)$ denotes the imaginary part of a complex number; $h_1.*h_2$ denotes the componentwise product between two images h_1, h_2 and $(\tilde{h}_{k,\lambda_\ell})_j = (h_{k,\lambda_\ell})_{-j}$ for all $j \in \chi$.

Finally, Equation (B.2) corresponds to Equation (3.9) in subsection 3.2.3 and to Equation (3.19) in subsection 3.4.1.

B.2 Hessian of $J_0(\phi)$

Here we present the calculation of Equation (3.13) which is the second partial derivative of $J_0(\phi)$ with respect to elements ϕ_t and ϕ_s, for all $s, t \in \chi$.

$$\begin{aligned}\text{Set } (r_{k,\lambda_\ell})_j &= \left|(h_{k,\lambda_\ell} \otimes e^{-i\phi/\lambda_\ell})_j\right|^2 - (o_{k,\lambda_\ell})_j \\ &= \left|\sum_{m\in\chi} (h_{k,\lambda_\ell})_m e^{-i\phi/\lambda_\ell}\right|^2 - (o_{k,\lambda_\ell})_j \text{ for all } j \in \chi\end{aligned}$$

Let $\vartheta_s = \overline{(h_{k,\lambda_\ell} \otimes e^{-i\phi/\lambda_\ell})_j} \cdot (h_{k,\lambda_\ell})_{j-s} \cdot e^{-i\phi_s/\lambda_\ell}$ for all $s \in \chi$. From (B.1) we have

$$\frac{\partial J_0(\phi)}{\partial \phi_s} = \frac{4}{\lambda_\ell} \sum_{\ell=1}^{3}\sum_{k=1}^{K}\sum_{j\in\chi}\left[\left|(h_{k,\lambda_\ell} \otimes e^{-i\phi/\lambda_\ell})_j\right|^2 - (o_{k,\lambda_\ell})_j\right] \cdot \text{Im}\{\vartheta_s\}$$

$$\frac{\partial^2 J_0(\phi)}{\partial \phi_s \partial \phi_t} = \frac{4}{\lambda_\ell} \sum_{\ell=1}^{3}\sum_{k=1}^{K}\sum_{j\in\chi}\left\{\left[\frac{\partial (r_{k,\lambda_\ell})_j}{\partial t}\right] \text{Im}\{\vartheta_s\} + (r_{k,\lambda_\ell})_j \text{Im}\left\{\frac{\partial \vartheta_s}{\partial t}\right\}\right\}$$

$$\begin{aligned}\frac{\partial (r_{k,\lambda_\ell})_j}{\partial t} &= \frac{\partial}{\partial t}\left|(h_{k,\lambda_\ell} \otimes e^{-i\phi/\lambda_\ell})_j\right|^2 = \frac{\partial}{\partial t}\left[\overline{(h_{k,\lambda_\ell} \otimes e^{-i\phi/\lambda_\ell})_j}(h_{k,\lambda_\ell} \otimes e^{-i\phi/\lambda_\ell})_j\right] \\ &= \overline{(h_{k,\lambda_\ell} \otimes e^{-i\phi/\lambda_\ell})_j}\ \frac{\partial}{\partial t}\left(h_{k,\lambda_\ell} \otimes e^{-i\phi/\lambda_\ell}\right)_j + \overline{\overline{(h_{k,\lambda_\ell} \otimes e^{-i\phi/\lambda_\ell})_j}\ \frac{\partial}{\partial t}\left(h_{k,\lambda_\ell} \otimes e^{-i\phi/\lambda_\ell}\right)_j}\end{aligned}$$

Recall the fact that if $z = a + ib$ then $z + \bar{z} = 2a = 2\text{Re}\{z\}$

$$\begin{aligned}\frac{\partial (r_{k,\lambda_\ell})_j}{\partial t} &= 2\ \text{Re}\left\{\overline{(h_{k,\lambda_\ell} \otimes e^{-i\phi/\lambda_\ell})_j}\ \frac{\partial}{\partial t}\left(h_{k,\lambda_\ell} \otimes e^{-i\phi/\lambda_\ell}\right)_j\right\} \\ &= 2\ \text{Re}\left\{\overline{(h_{k,\lambda_\ell} \otimes e^{-i\phi/\lambda_\ell})_j} \cdot \left(-\frac{i}{\lambda_\ell}\right)(h_{k,\lambda_\ell})_{j-t} \cdot e^{-i\phi_t/\lambda_\ell}\right\} \\ &= \frac{2}{\lambda_\ell}\ \text{Re}\left\{(-i)\left[\overline{(h_{k,\lambda_\ell} \otimes e^{-i\phi/\lambda_\ell})_j}\ (h_{k,\lambda_\ell})_{j-t}\ e^{-i\phi_t/\lambda_\ell}\right]\right\}\end{aligned}$$

Recall that if $z = a + ib$ then $(-i)z = b - ia$. Therefore $\text{Re}\{(-i)z\} = b = \text{Im}\{z\}$

$$\begin{aligned}\frac{\partial (r_{k,\lambda_\ell})_j}{\partial t} &= \frac{2}{\lambda_\ell}\ \text{Im}\left\{\overline{(h_{k,\lambda_\ell} \otimes e^{-i\phi/\lambda_\ell})_j}\ (h_{k,\lambda_\ell})_{j-t}\ e^{-i\phi_t/\lambda_\ell}\right\} \\ &= \frac{2}{\lambda_\ell}\text{Im}\{\vartheta_t\}\end{aligned}$$

For calculating $\dfrac{\partial \vartheta_s}{\partial t}$ we can distinguish two cases:

1. Suppose $t \in \chi$; $t \neq s$. Then we have:

$$\begin{aligned}
\frac{\partial \vartheta_s}{\partial t} &= \frac{\partial}{\partial t}\left\{\overline{(h_{k,\lambda_\ell} \otimes e^{-i\phi/\lambda_\ell})}_j \ (h_{k,\lambda_\ell})_{j-s} \ e^{-i\phi_s/\lambda_\ell}\right\} \\
&= \frac{\partial}{\partial t}\left\{\overline{(h_{k,\lambda_\ell} \otimes e^{-i\phi/\lambda_\ell})}_j\right\} \ (h_{k,\lambda_\ell})_{j-s} \ e^{-i\phi_s/\lambda_\ell} \\
&= \left(\frac{i}{\lambda_\ell}\right) \overline{(h_{k,\lambda_\ell})}_{j-t} \ e^{i\phi_t/\lambda_\ell} \ (h_{k,\lambda_\ell})_{j-s} \ e^{-i\phi_s/\lambda_\ell} \\
&= \left(\frac{i}{\lambda_\ell}\right) \overline{(h_{k,\lambda_\ell})}_{j-t} \ (h_{k,\lambda_\ell})_{j-s} \ e^{i\frac{\phi_t-\phi_s}{\lambda_\ell}} \\
\mathrm{Im}\left\{\frac{\partial \vartheta_s}{\partial t}\right\} &= \mathrm{Im}\left\{\left(\frac{i}{\lambda_\ell}\right) \overline{(h_{k,\lambda_\ell})}_{j-t} \ (h_{k,\lambda_\ell})_{j-s} \ e^{i\frac{\phi_t-\phi_s}{\lambda_\ell}}\right\}
\end{aligned}$$

   Recall that if $z = a + ib$ then $iz = -b + ia$, therefore, $\mathrm{Im}(iz) = a = \mathrm{Re}(z)$

$$\mathrm{Im}\left\{\frac{\partial \vartheta_s}{\partial t}\right\} = \frac{1}{\lambda_\ell} \ \mathrm{Re}\left\{\overline{(h_{k,\lambda_\ell})}_{j-t} \ (h_{k,\lambda_\ell})_{j-s} \ e^{i\frac{\phi_t-\phi_s}{\lambda_\ell}}\right\}$$

2. Suppose $t = s$, then we have:

$$\begin{aligned}
\frac{\partial \vartheta_s}{\partial t} = \frac{\partial \vartheta_s}{\partial s} &= \frac{\partial}{\partial s}\left\{\overline{(h_{k,\lambda_\ell} \otimes e^{-i\phi/\lambda_\ell})}_j \ (h_{k,\lambda_\ell})_{j-s} \ e^{-i\phi_s/\lambda_\ell}\right\} \\
&= \frac{\partial}{\partial s}\left\{e^{-i\phi_s/\lambda_\ell}\overline{(h_{k,\lambda_\ell} \otimes e^{-i\phi/\lambda_\ell})}_j\right\} \ (h_{k,\lambda_\ell})_{j-s} \\
&= \left\{\left(\frac{-i}{\lambda_\ell}\right) e^{-i\phi_s/\lambda_\ell}\overline{(h_{k,\lambda_\ell} \otimes e^{-i\phi/\lambda_\ell})}_j + \left(\frac{i}{\lambda_\ell}\right) \overline{(h_{k,\lambda_\ell})}_{j-s}\right\} \ (h_{k,\lambda_\ell})_{j-s} \\
&= \left(\frac{i}{\lambda_\ell}\right)\left\{\overline{(h_{k,\lambda_\ell})}_{j-s} \ (h_{k,\lambda_\ell})_{j-s} - \underbrace{\overline{(h_{k,\lambda_\ell} \otimes e^{-i\phi/\lambda_\ell})}_j \ (h_{k,\lambda_\ell})_{j-s} \ e^{-i\phi_s/\lambda_\ell}}_{\vartheta_s}\right\} \\
&= \left(\frac{i}{\lambda_\ell}\right)\left\{\overline{(h_{k,\lambda_\ell})}_{j-s} \ (h_{k,\lambda_\ell})_{j-s} - \vartheta_s\right\}
\end{aligned}$$

$$\begin{aligned}
\mathrm{Im}\left\{\frac{\partial \vartheta_s}{\partial s}\right\} &= \mathrm{Im}\left\{\left(\frac{i}{\lambda_\ell}\right)\left[\overline{(h_{k,\lambda_\ell})}_{j-s} \ (h_{k,\lambda_\ell})_{j-s} - \vartheta_s\right]\right\} \\
&= \left(\frac{1}{\lambda_\ell}\right) \mathrm{Re}\left\{\overline{(h_{k,\lambda_\ell})}_{j-s} \ (h_{k,\lambda_\ell})_{j-s} - \vartheta_s\right\} \\
&= \left(\frac{1}{\lambda_\ell}\right) \mathrm{Re}\left\{\overline{(h_{k,\lambda_\ell})}_{j-s} \ (h_{k,\lambda_\ell})_{j-s} \ e^{-i\frac{\phi_s-\phi_s}{\lambda_\ell}} - \vartheta_s\right\}
\end{aligned}$$

Comparing the quantities $\mathrm{Im}\left\{\frac{\partial \vartheta_s}{\partial t}\right\}$ for $t \neq s$ and $\mathrm{Im}\left\{\frac{\partial \vartheta_s}{\partial s}\right\}$ for $t = s$, the difference is in the parameter ϑ_s in the second case. Then we can give a unique formula which include both expressions as follows:

For all $t \in \chi$, $\quad \mathrm{Im}\left\{\frac{\partial \vartheta_s}{\partial t}\right\} = \left(\frac{1}{\lambda_\ell}\right) \mathrm{Re}\left\{e^{i\frac{\phi_t-\phi_s}{\lambda_\ell}} \ (h_{k,\lambda_\ell})_{j-s} \ \overline{(h_{k,\lambda_\ell})}_{j-t} - \delta_{s,t}\vartheta_s\right\}$

where $\delta_{s,t} = \begin{cases} 1 & \text{if } t = s \\ 0 & \text{otherwise} \end{cases}$ is the Kronecker delta.

Finally we replace the formulas for $\dfrac{\partial (r_{k,\lambda_\ell})_j}{\partial t}$ and $\mathrm{Im}\left\{\dfrac{\partial \vartheta_s}{\partial t}\right\}$ inside the expression of $\dfrac{\partial^2 J_0(\phi)}{\partial s \partial t}$.

Appendix C

Detailed Wirtinger Derivatives

In this Appendix we present the most important facts about Wirtinger derivatives for both one-dimensional and n-dimensional cases.

C.1 One-dimensional Wirtinger derivatives

Let us start by defining three real-valued functions as follows

$$\begin{array}{rcl} f:\mathbb{C} & \longrightarrow & \mathbb{R} \\ z & \longmapsto & f(z) \end{array} \qquad \begin{array}{rcl} \tilde{f}:\mathbb{C}\times\mathbb{C} & \longrightarrow & \mathbb{R} \\ (z,\bar{z}) & \longmapsto & \tilde{f}(z,\bar{z}) \end{array} \qquad \begin{array}{rcl} \hat{f}:\mathbb{R}\times\mathbb{R} & \longrightarrow & \mathbb{R} \\ (z_r,z_i) & \longmapsto & \hat{f}(z_r,z_i) \end{array} \tag{C.1}$$

When optimizing f with respect to the complex variable $z = z_r + iz_i$, it is possible to work with the equivalent gradient of the function defined as the mapping $\hat{f}$. This means that

$$f(z) = \hat{f}(z_r, z_i)$$

When $f(z)$ is $\mathbb{C}$-valued, it is also possible to define it as

$$f(z) = \hat{f}(z_r, z_i) = v(z_r, z_i) + iw(z_r, z_i) \tag{C.2}$$

where $v(z_r, z_i)$ and $w(z_r, z_i)$ are real-valued functions related to each other by the Cauchy-Riemann equations

$$\frac{\partial v}{\partial z_r} = \frac{\partial w}{\partial z_i} \qquad \text{and} \qquad \frac{\partial w}{\partial z_r} = \frac{\partial v}{\partial z_i} \tag{C.3}$$

As it is expressed in [2] and [23], finding $f'(z)$ requires $f(z)$ to be $\mathbb{C}$-derivable. However, by exploiting the structure of $\mathbb{R}^2$ vector space, the partial derivatives with respect to the real components can be calculated.

Function $f(z)$ can also be written in terms of its complex and complex-conjugate components, that is,

$$f(z) = \tilde{f}(z, \bar{z}) = \hat{f}(z_r, z_i) = v(z_r, z_i) + iw(z_r, z_i) \tag{C.4}$$

where they are holomorphic in z for fixed $\bar{z}$ and holomorphic in $\bar{z}$ for fixed z.

The core of Wirtinger calculus is the definition of a new conjugate coordinate system, whose conjugate coordinates are defined as

$$\begin{bmatrix} z \\ \bar{z} \end{bmatrix} \in \mathbb{C}\times\mathbb{C};\ z = z_r + iz_i \text{ and } \bar{z} = z_r - iz_i$$

which lead to the derivatives

$$\frac{\partial f}{\partial z} := \frac{\partial f(z,\bar{z})}{\partial z}\Big|_{\bar{z}=constant} \qquad \frac{\partial f}{\partial \bar{z}} := \frac{\partial f(z,\bar{z})}{\partial \bar{z}}\Big|_{z=constant} \tag{C.5}$$

These generalized complex derivatives can be written in terms of the real $\left(z_r = \frac{z+\bar{z}}{2}\right)$ and imaginary $\left(z_i = \frac{z-\bar{z}}{2i}\right)$ parts of the complex variable z as follows

$$\frac{\partial f}{\partial z} \triangleq \frac{1}{2}\left(\frac{\partial f}{\partial z_r} - i\frac{\partial f}{\partial z_i}\right) \qquad \text{and} \qquad \frac{\partial f}{\partial \bar{z}} \triangleq \frac{1}{2}\left(\frac{\partial f}{\partial z_r} + i\frac{\partial f}{\partial z_i}\right) \tag{C.6}$$

The Cauchy-Riemann equations can simply be stated as $\frac{\partial f}{\partial \bar{z}} = 0$. This means, an analytic function cannot depend on $\bar{z}$. For real-valued $f(z)$, we have

$$\overline{\left(\frac{\partial f}{\partial z}\right)} = \frac{\partial f}{\partial \bar{z}} \tag{A}$$

i.e., the derivative and the conjugate derivative are complex conjugates of each other, then we only need to compute one or the other. As a consequence, a sufficient and necessary condition for real-valued f to have a stationary point is $\frac{\partial f}{\partial z} = 0$. An equivalent necessary and sufficient condition is $\frac{\partial f}{\partial \bar{z}} = 0$. With all this, the complex gradient is defined as

$$\nabla f = \overline{\left[\frac{\partial f}{\partial z}, \frac{\partial f}{\partial \bar{z}}\right]} \tag{C.7}$$

Example. Let us consider $f(z) = |z|^2 = z_r^2 + z_i^2 = z \cdot \bar{z}$. If we derive with respect to the real and imaginary components we have

$$\frac{\partial f(z)}{\partial z_r} = 2z_r \qquad \text{and} \qquad \frac{\partial f(z)}{\partial z_i} = 2z_i$$

which takes two computations, while if we use (C.5) we have

$$\frac{\partial f}{\partial \bar{z}} := \frac{\partial f(z,\bar{z})}{\partial \bar{z}}\Big|_{z=constant} = z$$

which only needs one computation.

C.2 n-dimensional Wirtinger derivatives

In this section we retake the general ideas presented in subsection 4.1.1 and present them in more detail to understand the development in n dimensions.

Define the n-dimensional column vector $\mathbf{z}$ by $\mathbf{z} = (z_1, \ldots, z_n)^T \in \mathbb{C}^n$, where $z_\ell = z_{r_\ell} + iz_{i_\ell}$ for $\ell = 1, \ldots, n$, or equivalently $\mathbf{z} = \mathbf{z}_r + i\mathbf{z}_i$ with $\mathbf{z}_r = (z_{r_1}, \ldots, z_{r_n})$ and $\mathbf{z}_i = (z_{i_1}, \ldots, z_{i_n})$. The corresponding conjugate vector of $\mathbf{z}$ is $\bar{\mathbf{z}} = (\bar{z}_1, \ldots, \bar{z}_n)^T \in \mathbb{C}^n$. This allow us to define the

following three real-valued functions

$$\begin{array}{rcl} f:\mathbb{C}^n & \longrightarrow & \mathbb{R} \\ \mathbf{z} & \longmapsto & f(\mathbf{z}) \end{array} \qquad \begin{array}{rcl} \tilde{f}:\mathbb{C}^n\times\mathbb{C}^n & \longrightarrow & \mathbb{R} \\ (\mathbf{z},\bar{\mathbf{z}}) & \longmapsto & \tilde{f}(\mathbf{z},\bar{\mathbf{z}}) \end{array} \qquad \begin{array}{rcl} \hat{f}:\mathbb{R}^n\times\mathbb{R}^n & \longrightarrow & \mathbb{R} \\ (\mathbf{z}_r,\mathbf{z}_i) & \longmapsto & \hat{f}(\mathbf{z}_r,\mathbf{z}_i) \end{array} \tag{C.8}$$

Following the same reasoning to obtain relations (C.2) and (C.4), we can obtain the same equivalence in the n-dimensional case:

$$f(\mathbf{z}) = \tilde{f}(\mathbf{z},\bar{\mathbf{z}}) = \hat{f}(\mathbf{z}_r,\mathbf{z}_i) = v(\mathbf{z}_r,\mathbf{z}_i) + iw(\mathbf{z}_r,\mathbf{z}_i) \tag{C.9}$$

The complex conjugate coordinates are then defined as $\begin{bmatrix}\mathbf{z}\\ \bar{\mathbf{z}}\end{bmatrix} \in \mathbb{C}^n\times\mathbb{C}^n$.

In the same way we can describe the generalized complex derivatives

$$\begin{aligned} \frac{\partial f}{\partial \mathbf{z}} &:= \frac{\partial f(\mathbf{z},\bar{\mathbf{z}})}{\partial \mathbf{z}} = \left(\frac{\partial f}{\partial z_1},\ldots,\frac{\partial f}{\partial z_n}\right)\Big|_{\bar{\mathbf{z}}=constant} \\ \frac{\partial f}{\partial \bar{\mathbf{z}}} &:= \frac{\partial f(\mathbf{z},\bar{\mathbf{z}})}{\partial \bar{\mathbf{z}}} = \left(\frac{\partial f}{\partial \bar{z}_1},\ldots,\frac{\partial f}{\partial \bar{z}_n}\right)\Big|_{\mathbf{z}=constant} \end{aligned} \tag{C.10}$$

where

$$\frac{\partial f}{\partial z_\ell} = \frac{1}{2}\left(\frac{\partial f}{\partial z_{r_\ell}} - i\frac{\partial f}{\partial z_{i_\ell}}\right) \qquad \text{and} \qquad \frac{\partial f}{\partial \bar{z}_\ell} = \frac{1}{2}\left(\frac{\partial f}{\partial z_{r_\ell}} + i\frac{\partial f}{\partial z_{i_\ell}}\right) \qquad \text{for } \ell = 1,\ldots,n \tag{C.11}$$

The n-dimensional case also holds the Cauchy-Riemann condition with respect to the complex conjugate variable, that is, $\dfrac{\partial f}{\partial \bar{\mathbf{z}}} = 0$, as well as the conditions for a stationary point at $\mathbf{z}_0$ which are: $\dfrac{\partial f(\mathbf{z}_0,\bar{\mathbf{z}_0})}{\partial \mathbf{z}} = 0$ and $\dfrac{\partial f(\mathbf{z}_0,\bar{\mathbf{z}_0})}{\partial \bar{\mathbf{z}}} = 0$.

Finally, the gradient vector is defined as

$$\nabla f(\mathbf{z}) \triangleq \left(\frac{\partial \tilde{f}(\mathbf{z},\bar{\mathbf{z}})}{\partial \mathbf{z}}\right)^* = \left(\frac{\partial f(\mathbf{z})}{\partial \mathbf{z}}\right)^* \triangleq \frac{1}{2}\left(\frac{\partial f(\mathbf{z})}{\partial \mathbf{z}_r} + i\frac{\partial f(\mathbf{z})}{\partial \mathbf{z}_i}\right) \tag{C.12}$$

where $*$ represents the conjugate transpose.

In conclusion, Wirtinger derivatives provide us with a compact notation in order to obtain the gradient of our non-holomorphic optimization problem. In the following section we present the development of the gradient following that notation.

Appendix D

Continuation numerical tests Chapter 4

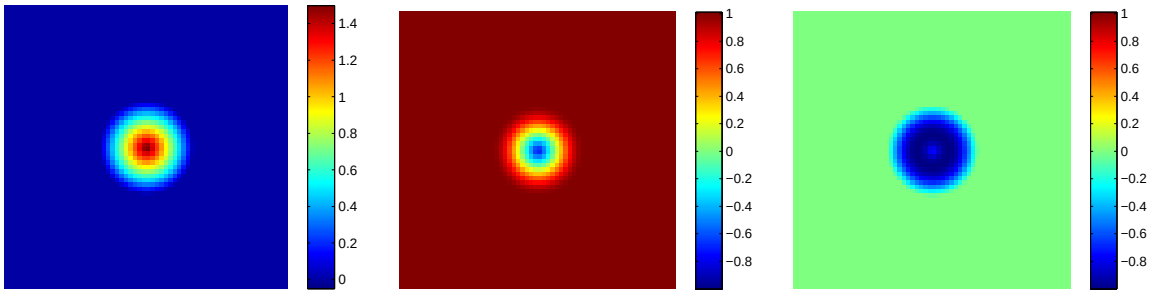

(a) (b) (c)

Figure D.1: Cone object. True values for phase and specimen functions (a) Phase function $\check{\phi}$, (b) $\mathrm{Re}\{\check{u}\}$, (c) $\mathrm{Im}\{\check{u}\}$

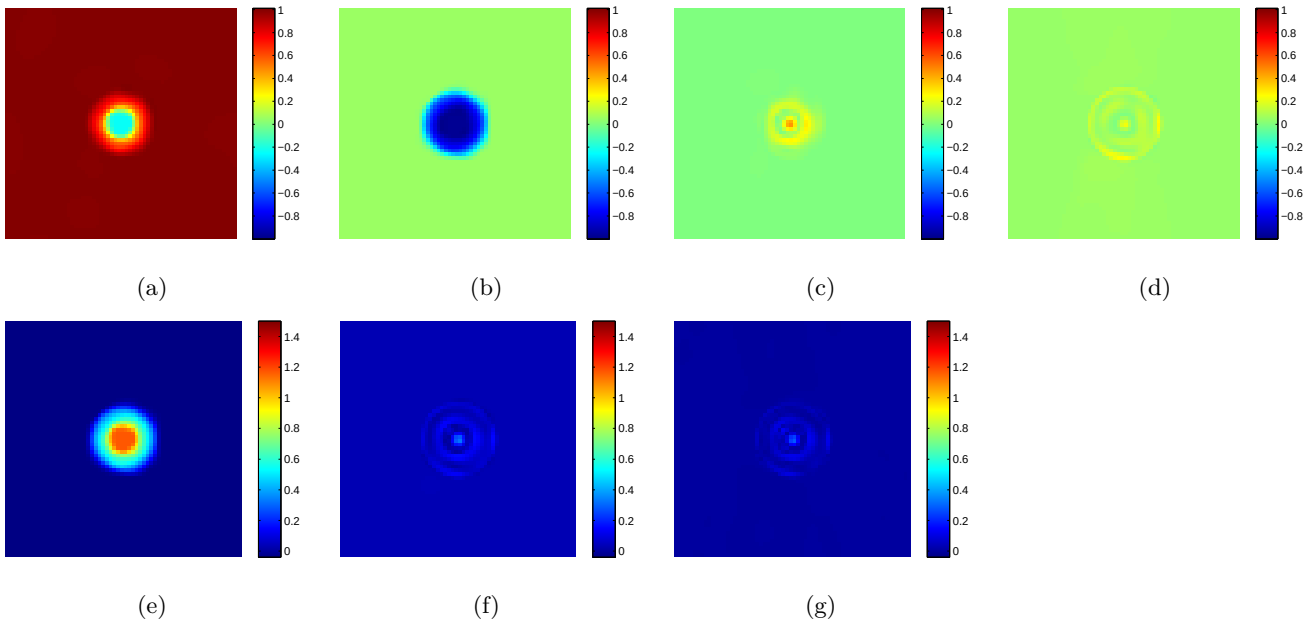

(a) (b) (c) (d)

(e) (f) (g)

Figure D.2: Estimation of Conjugate Gradient PR-PA method without projection, initial guess $u_{01} = (1, i0)$. (a) $\mathrm{Re}\{\hat{u}\}$, (b) $\mathrm{Im}\{\hat{u}\}$, (c) $\mathrm{Re}\{|\hat{u} - \check{u}|\}$, (d) $\mathrm{Im}\{|\hat{u} - \check{u}|\}$, (e) $\hat{\phi}$, (f) $\left|\hat{\phi} - \check{\phi}\right|$, (g) $\left|\check{\phi}_j - \hat{\phi}_j - \overline{\check{\phi} - \hat{\phi}}\right|$

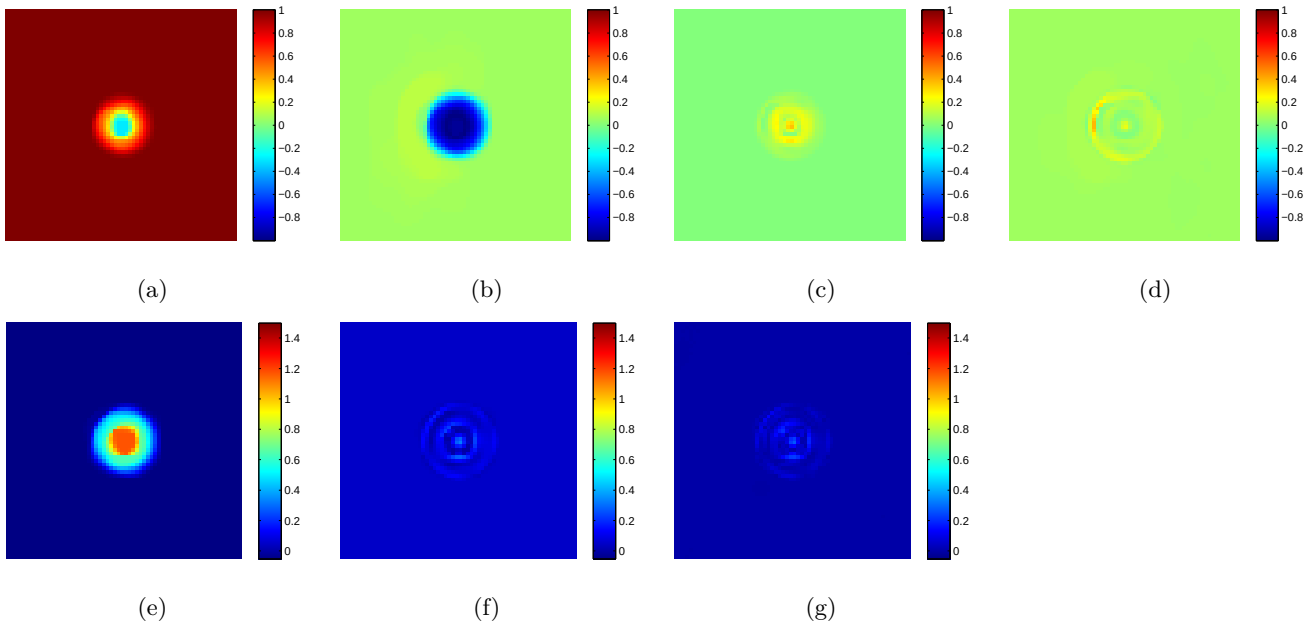

(a) (b) (c) (d)

(e) (f) (g)

Figure D.3: Estimation of Conjugate Gradient PR-PA method with projection, initial guess $u_{01} = (1, i0)$. (a) $\mathrm{Re}\{\hat{u}\}$, (b) $\mathrm{Im}\{\hat{u}\}$, (c) $\mathrm{Re}\{|\hat{u} - \check{u}|\}$, (d) $\mathrm{Im}\{|\hat{u} - \check{u}|\}$, (e) $\hat{\phi}$, (f) $\left|\hat{\phi} - \check{\phi}\right|$, (g) $\left|\check{\phi}_j - \hat{\phi}_j - \overline{\check{\phi} - \hat{\phi}}\right|$

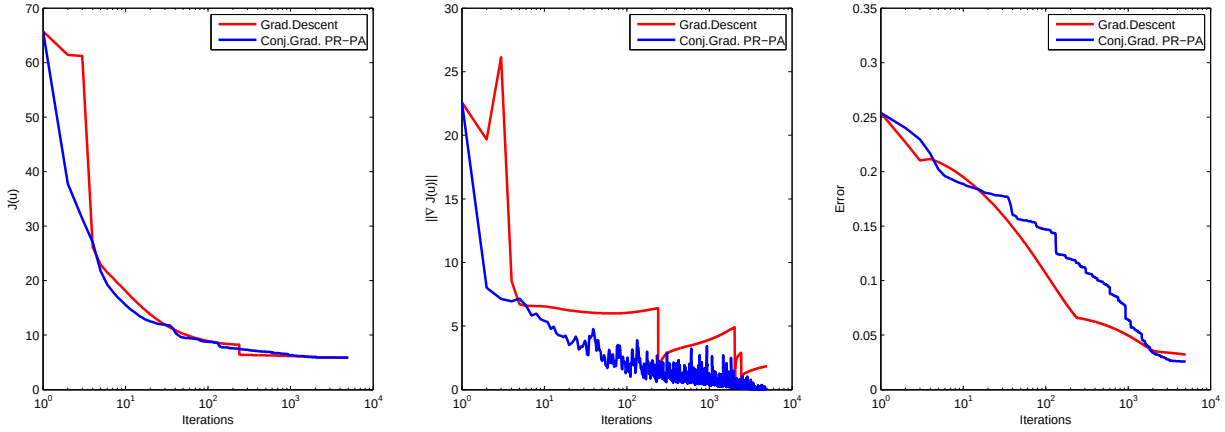

(a) (b) (c)

Figure D.4: Methods comparison without projection, initial guess $u_{01} = (1, i0)$. (a) Convergence, (b) Norm of gradient, (c) Error

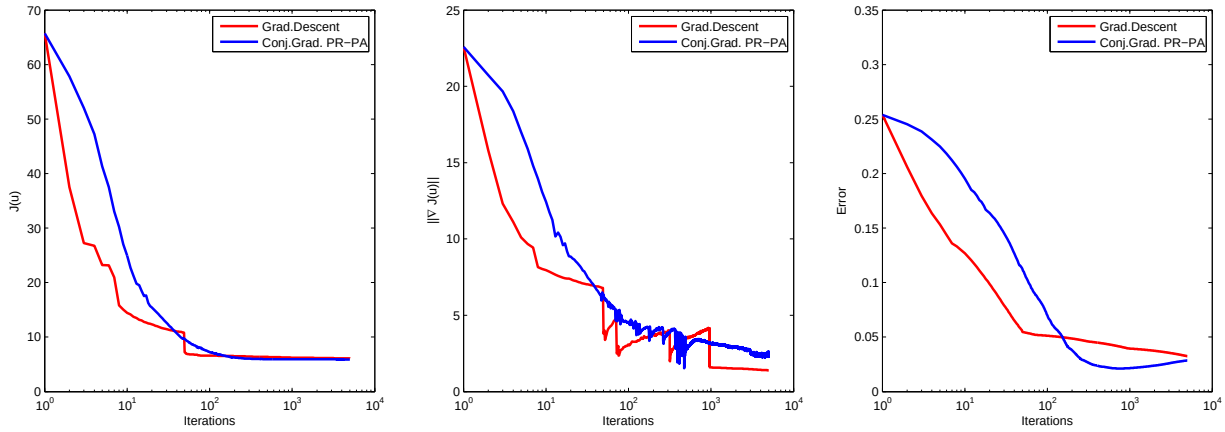

(a) (b) (c)

Figure D.5: Methods comparison with projection, initial guess $u_{01} = (1, i0)$. (a) Convergence, (b) Norm of gradient, (c) Error

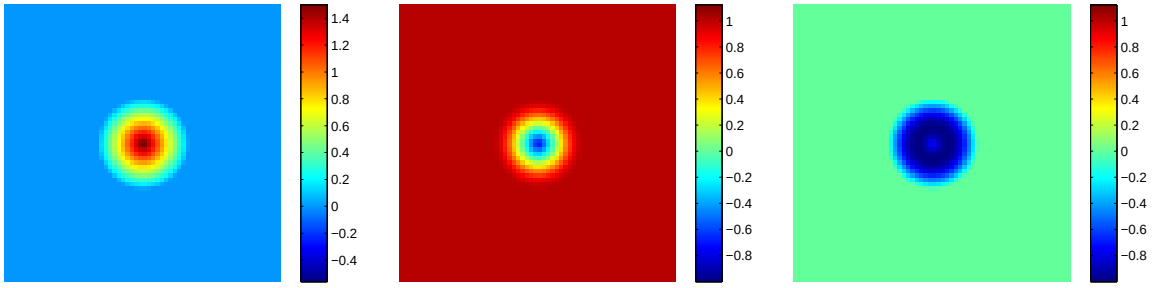

(a) (b) (c)

Figure D.6: Cone object. True values for phase and specimen functions (a) Phase function $\check{\phi}$, (b) $\mathrm{Re}\{\check{u}\}$, (c) $\mathrm{Im}\{\check{u}\}$

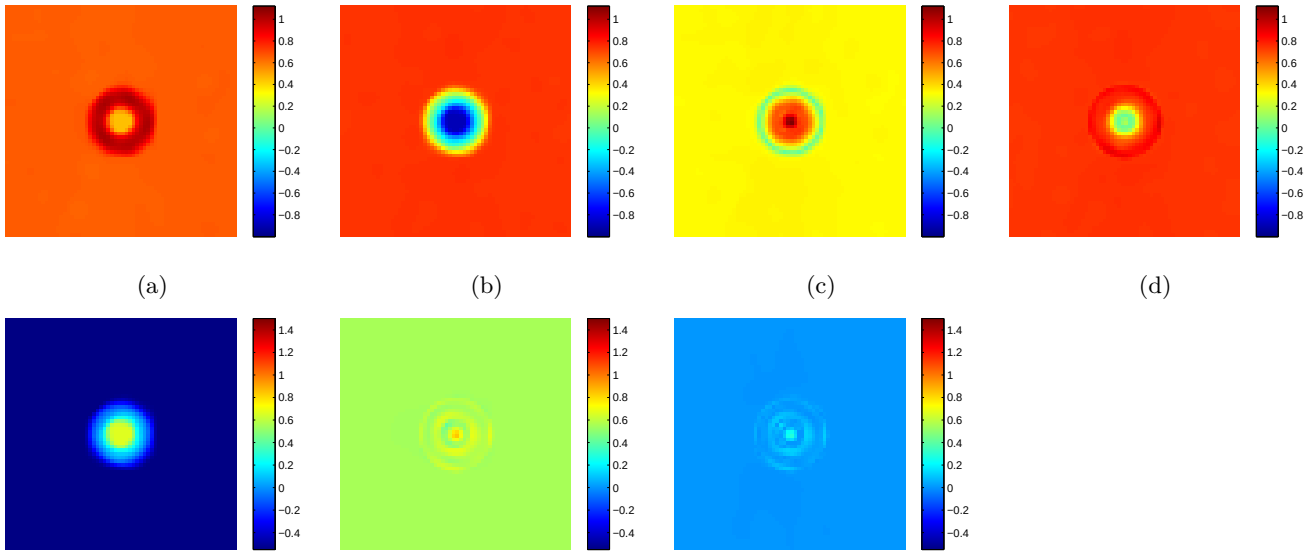

(a) (b) (c) (d)

(e) (f) (g)

Figure D.7: Estimation of Conjugate Gradient PR-PA method without projection, initial guess $u_{02} = \left(\frac{1}{\sqrt{2}}, i\frac{1}{\sqrt{2}}\right)$. (a) $\mathrm{Re}\{\hat{u}\}$, (b) $\mathrm{Im}\{\hat{u}\}$, (c) $\mathrm{Re}\{|\hat{u} - \check{u}|\}$, (d) $\mathrm{Im}\{|\hat{u} - \check{u}|\}$, (e) $\hat{\phi}$, (f) $\left|\hat{\phi} - \check{\phi}\right|$, (g) $\left|\check{\phi}_j - \hat{\phi}_j - \overline{\check{\phi} - \hat{\phi}}\right|$

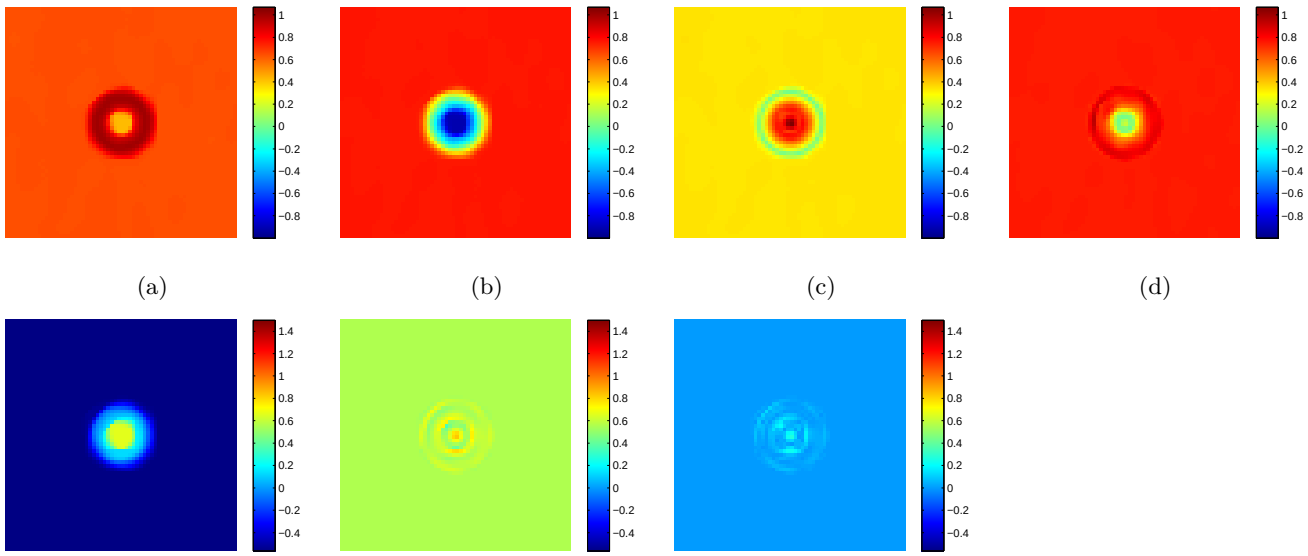

(a) (b) (c) (d)

(e) (f) (g)

Figure D.8: Estimation of Conjugate Gradient PR-PA method with projection, initial guess $u_{02} = \left(\frac{1}{\sqrt{2}}, i\frac{1}{\sqrt{2}}\right)$. (a) $\mathrm{Re}\{\hat{u}\}$, (b) $\mathrm{Im}\{\hat{u}\}$, (c) $\mathrm{Re}\{|\hat{u} - \check{u}|\}$, (d) $\mathrm{Im}\{|\hat{u} - \check{u}|\}$, (e) $\hat{\phi}$, (f) $\left|\hat{\phi} - \check{\phi}\right|$, (g) $\left|\check{\phi}_j - \hat{\phi}_j - \overline{\check{\phi} - \hat{\phi}}\right|$

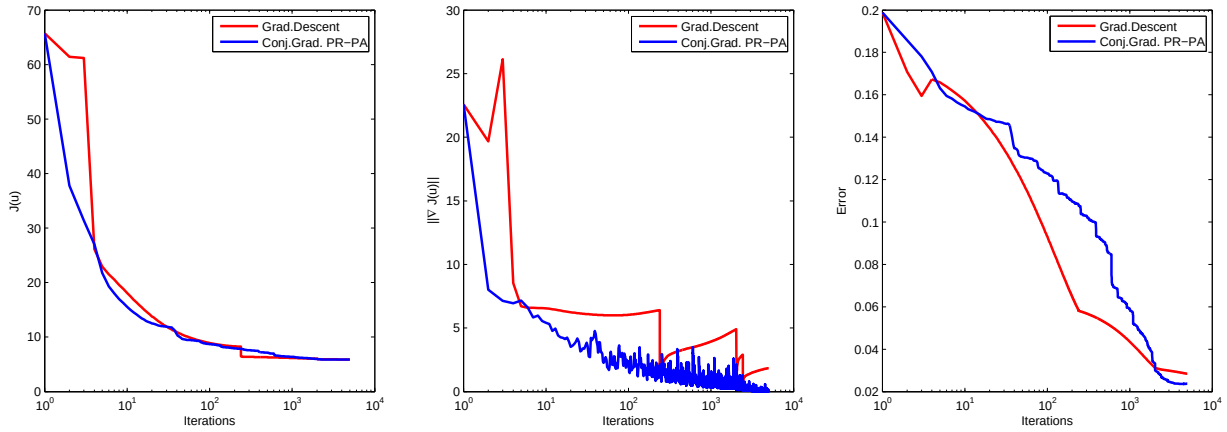

(a) (b) (c)

Figure D.9: Methods comparison without projection, initial guess $u_{02} = \left(\frac{1}{\sqrt{2}}, i\frac{1}{\sqrt{2}}\right)$. (a) Convergence, (b) Norm of gradient, (c) Error

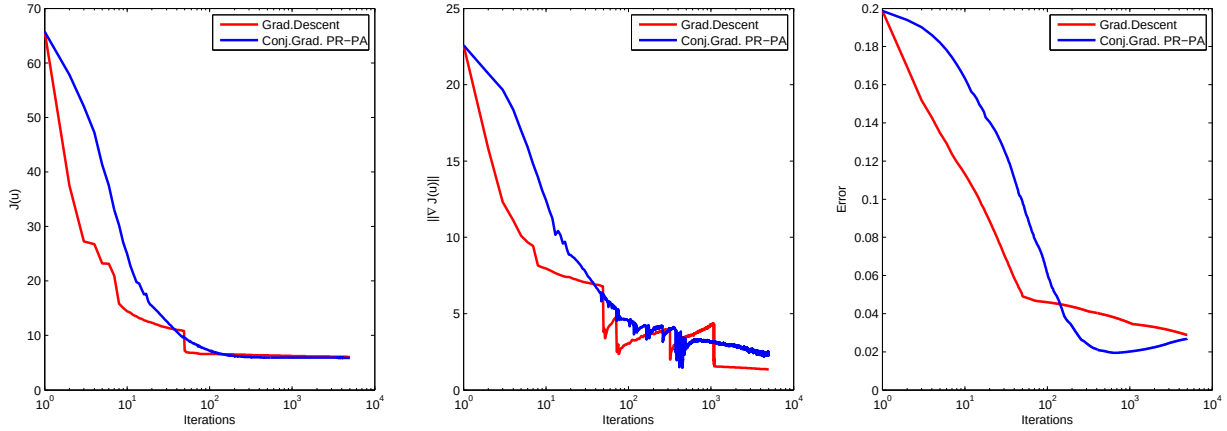

(a) (b) (c)

Figure D.10: Methods comparison with projection, initial guess $u_{02} = \left(\frac{1}{\sqrt{2}}, i\frac{1}{\sqrt{2}}\right)$. (a) Convergence, (b) Norm of gradient, (c) Error

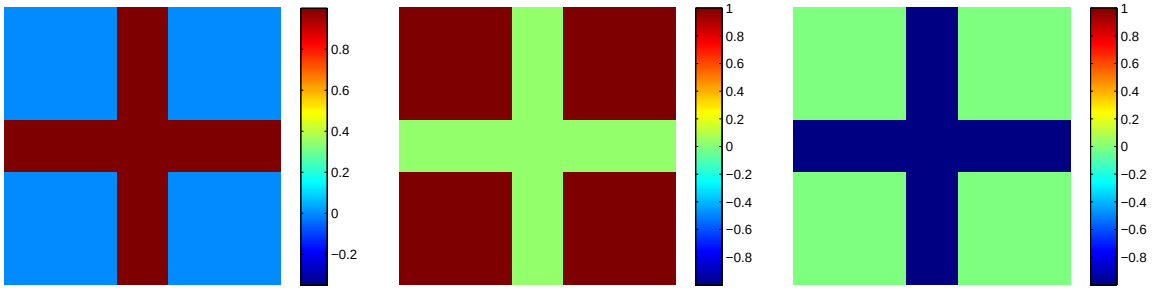

(a) (b) (c)

Figure D.11: Cross object. True values for phase and specimen functions (a) Phase function $\check{\phi}$, (b) $\mathbb{R}e\{\check{u}\}$, (c) $\mathrm{Im}\{\check{u}\}$

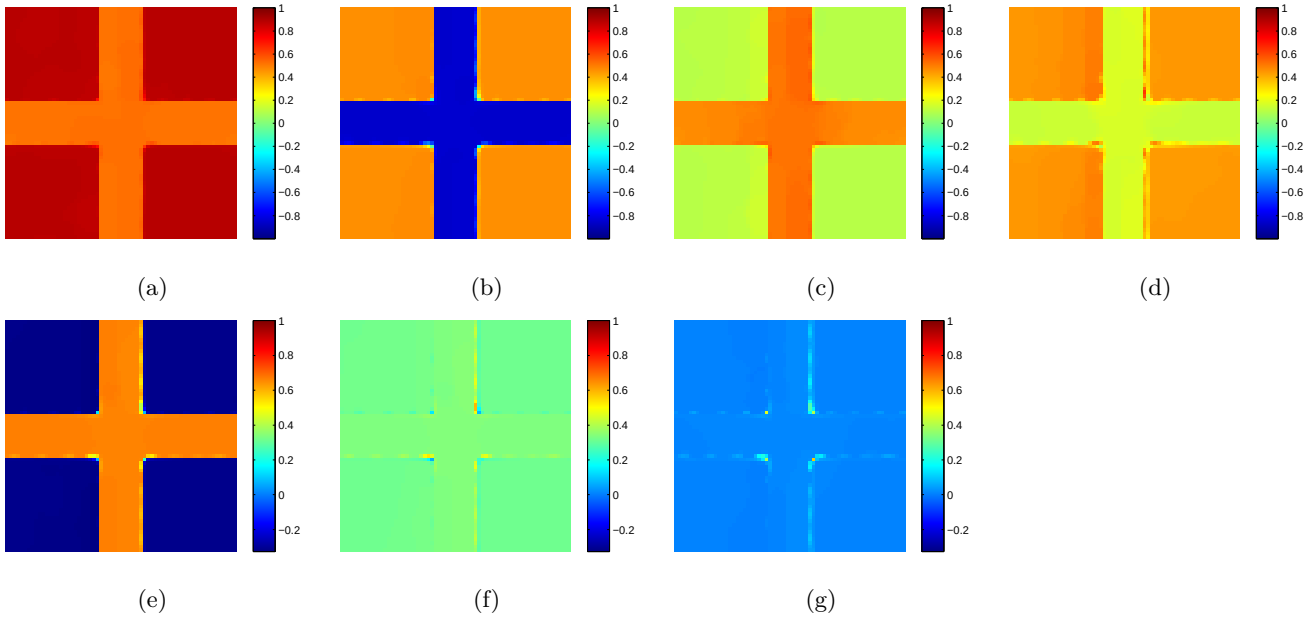

Figure D.12: Estimation of Conjugate Gradient PR-PA method without projection, initial guess $u_{01} = (1, i0)$. (a) $\mathrm{Re}\{\hat{u}\}$, (b) $\mathrm{Im}\{\hat{u}\}$, (c) $\mathrm{Re}\{|\hat{u} - \check{u}|\}$, (d) $\mathrm{Im}\{|\hat{u} - \check{u}|\}$, (e) $\hat{\phi}$, (f) $\left|\hat{\phi} - \check{\phi}\right|$, (g) $\left|\check{\phi}_j - \hat{\phi}_j - \overline{\check{\phi} - \hat{\phi}}\right|$

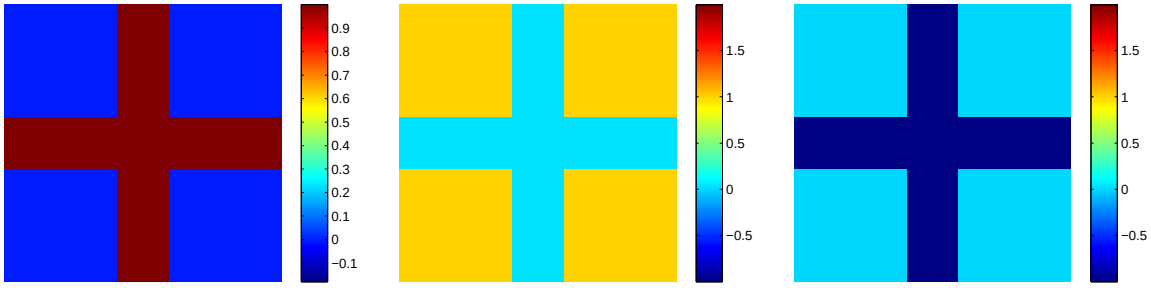

Figure D.13: Cross object. True values for phase and specimen functions (a) Phase function $\check{\phi}$, (b) $\mathbb{R}e\{\check{u}\}$, (c) $\mathrm{Im}\{\check{u}\}$

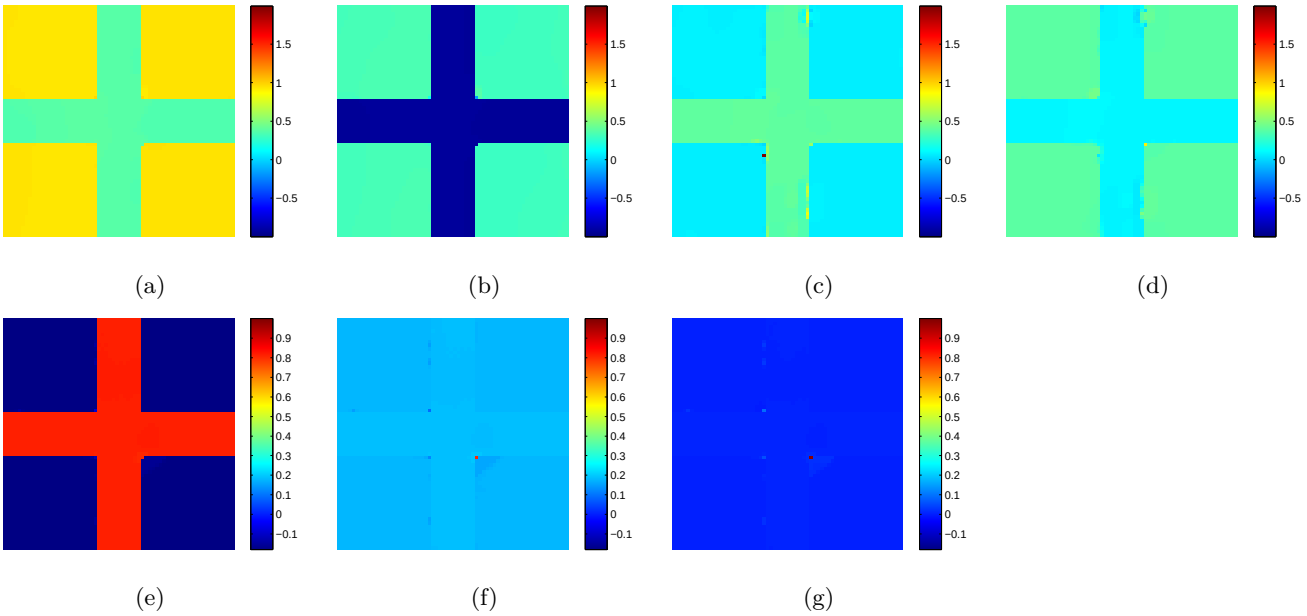

(a) (b) (c) (d)

(e) (f) (g)

Figure D.14: Estimation of Conjugate Gradient PR-PA method with projection, initial guess $u_{01} = (1, i0)$. (a) $\mathrm{Re}\{\hat{u}\}$, (b) $\mathrm{Im}\{\hat{u}\}$, (c) $\mathrm{Re}\{|\hat{u} - \check{u}|\}$, (d) $\mathrm{Im}\{|\hat{u} - \check{u}|\}$, (e) $\hat{\phi}$, (f) $\left|\hat{\phi} - \check{\phi}\right|$, (g) $\left|\check{\phi}_j - \hat{\phi}_j - \overline{\check{\phi} - \hat{\phi}}\right|$

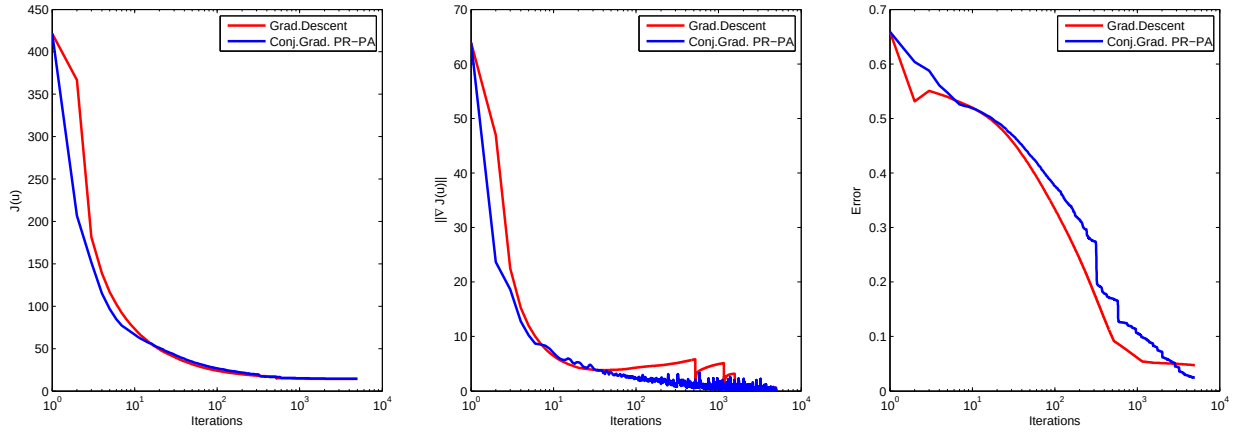

(a) (b) (c)

Figure D.15: Methods comparison without projection, initial guess $u_{01} = (1, i0)$. (a) Convergence, (b) Norm of gradient, (c) Error

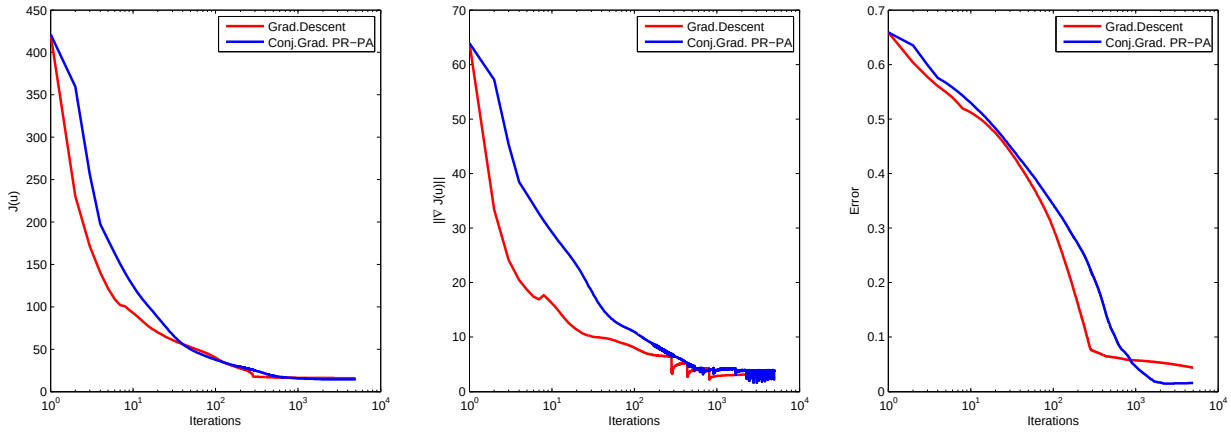

(a) (b) (c)

Figure D.16: Methods comparison with projection, initial guess $u_{01} = (1, i0)$. (a) Convergence, (b) Norm of gradient, (c) Error

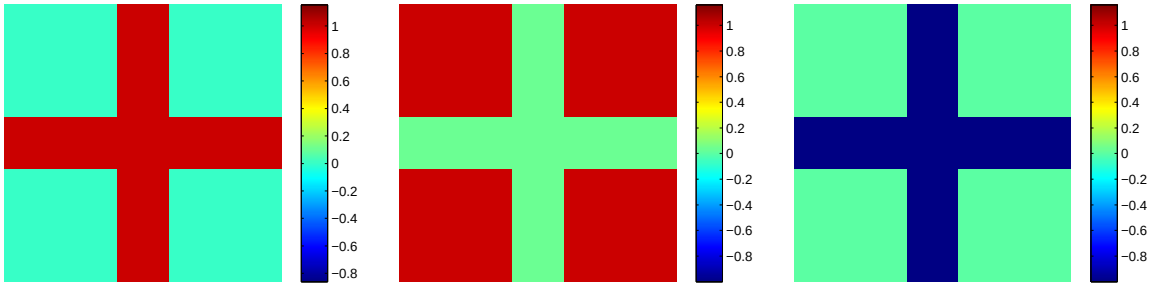

(a) (b) (c)

Figure D.17: Cross object. True values for phase and specimen functions (a) Phase function $\check{\phi}$, (b) $\mathbb{R}e\{\check{u}\}$, (c) $\mathrm{Im}\{\check{u}\}$

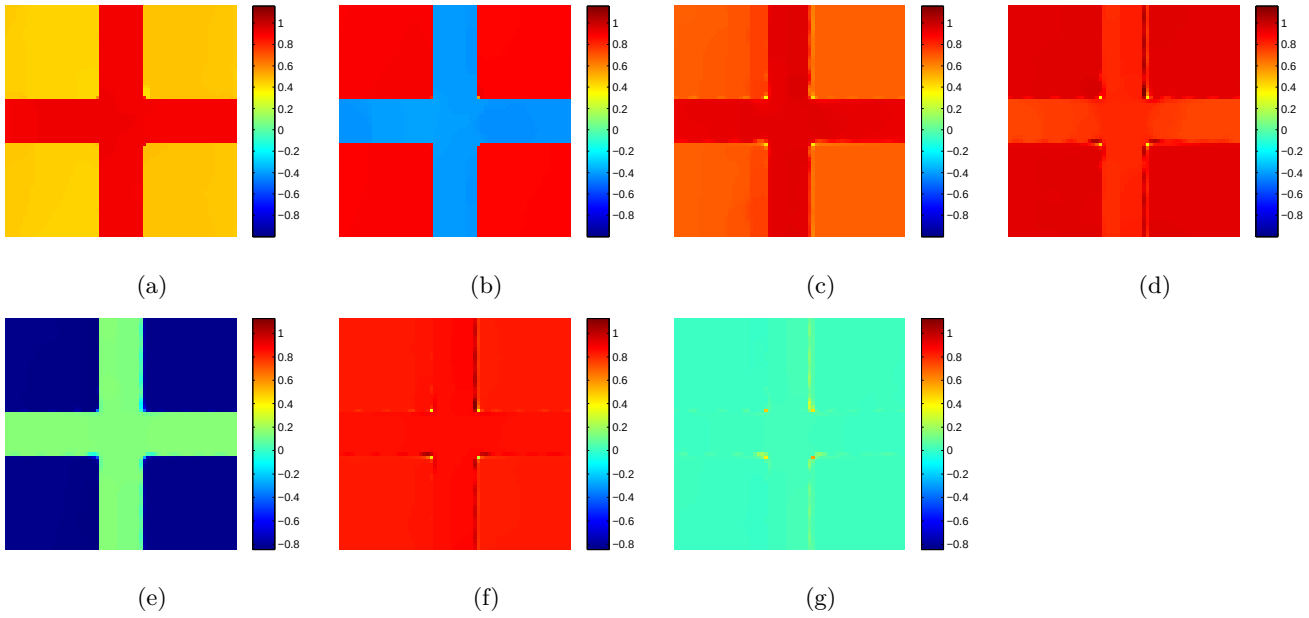

Figure D.18: Estimation of Conjugate Gradient PR-PA method without projection, initial guess $u_{02} = (\frac{1}{\sqrt{2}}, i\frac{1}{\sqrt{2}})$. (a) $\mathrm{Re}\{\hat{u}\}$, (b) $\mathrm{Im}\{\hat{u}\}$, (c) $\mathrm{Re}\{|\hat{u} - \check{u}|\}$, (d) $\mathrm{Im}\{|\hat{u} - \check{u}|\}$, (e) $\hat{\phi}$, (f) $\left|\hat{\phi} - \check{\phi}\right|$, (g) $\left|\check{\phi}_j - \hat{\phi}_j - \overline{\check{\phi} - \hat{\phi}}\right|$

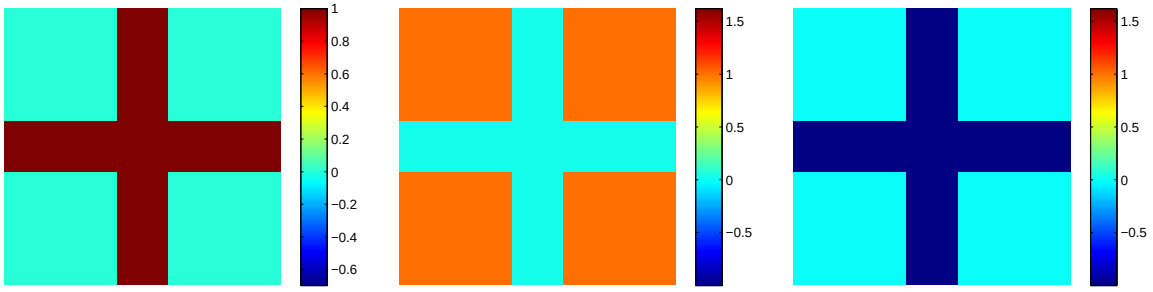

Figure D.19: Cross object. True values for phase and specimen functions (a) Phase function $\check{\phi}$, (b) $\mathbb{R}e\{\check{u}\}$, (c) $\mathrm{Im}\{\check{u}\}$

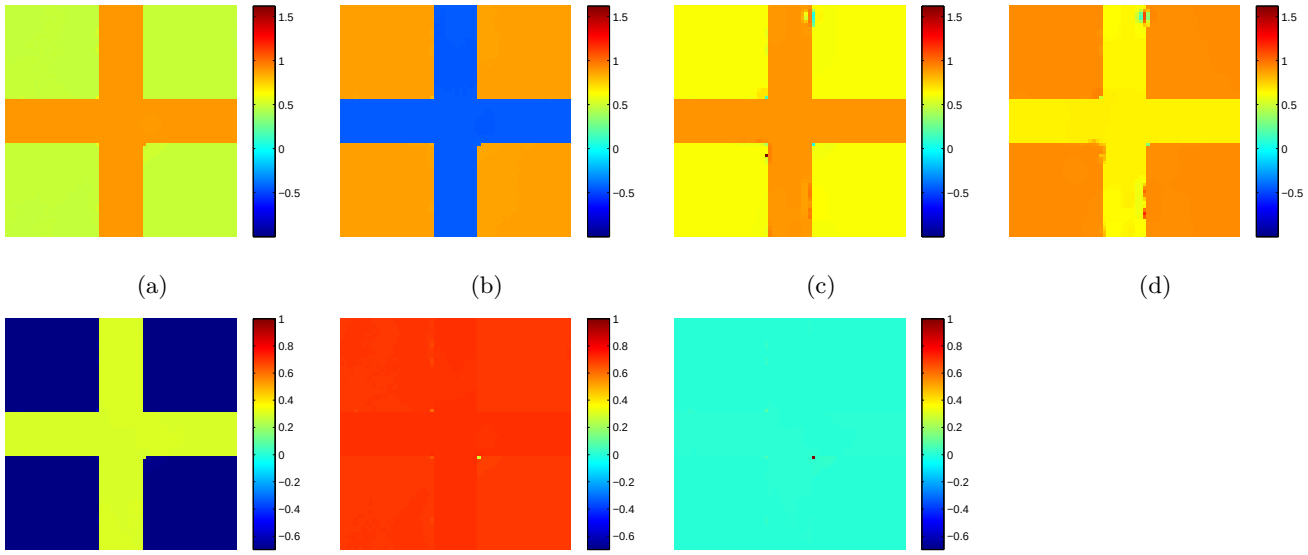

(a) (b) (c) (d)

(e) (f) (g)

Figure D.20: Estimation of Conjugate Gradient PR-PA method with projection, initial guess $u_{02} = (\frac{1}{\sqrt{2}}, i\frac{1}{\sqrt{2}})$. (a) $\mathrm{Re}\{\hat{u}\}$, (b) $\mathrm{Im}\{\hat{u}\}$, (c) $\mathrm{Re}\{|\hat{u} - \check{u}|\}$, (d) $\mathrm{Im}\{|\hat{u} - \check{u}|\}$, (e) $\hat{\phi}$, (f) $\left|\hat{\phi} - \check{\phi}\right|$, (g) $\left|\check{\phi}_j - \hat{\phi}_j - \overline{\check{\phi} - \hat{\phi}}\right|$

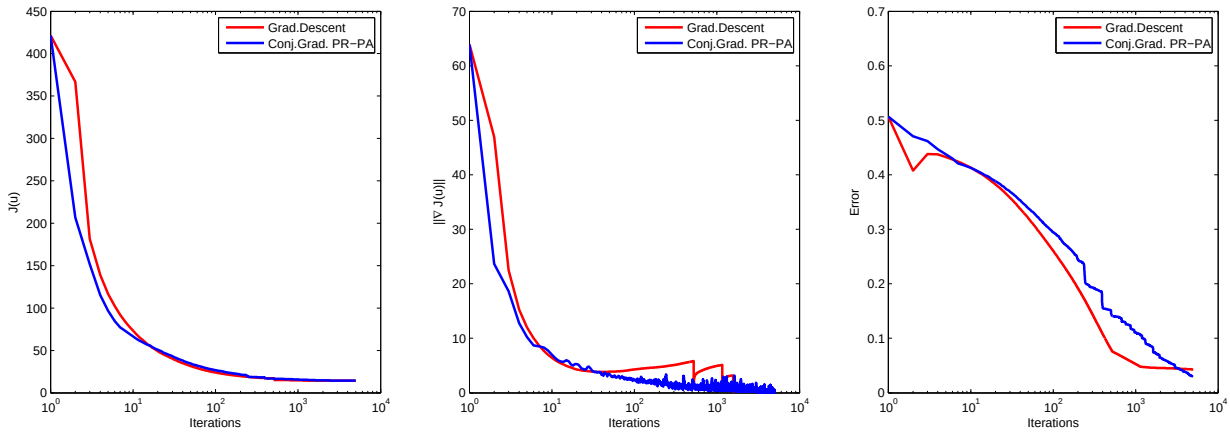

(a) (b) (c)

Figure D.21: Methods comparison without projection. (a) Convergence, (b) Norm of gradient, (c) Error

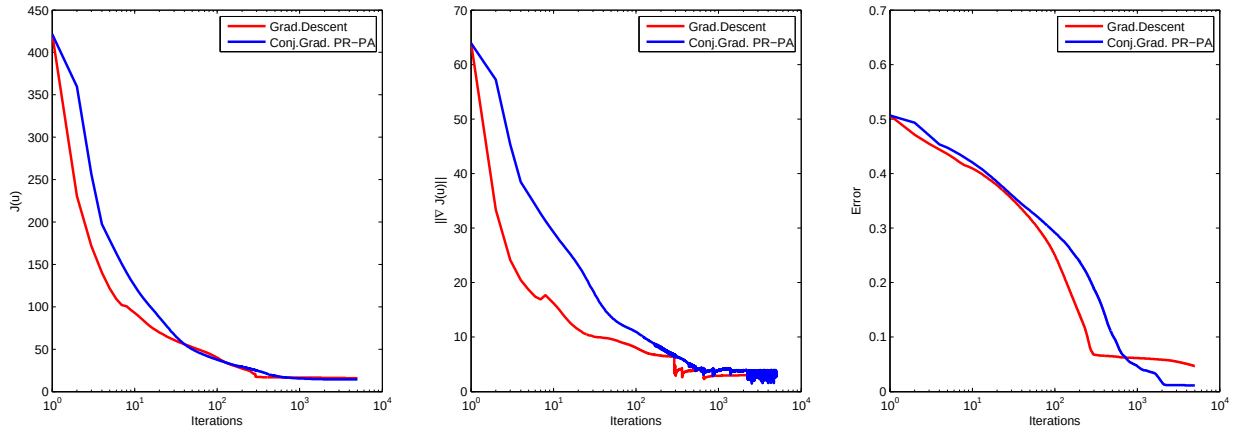

(a) (b) (c)

Figure D.22: Methods comparison with projection. (a) Convergence, (b) Norm of gradient, (c) Error

Bibliography

[1] R. Acar and C. R. Vogel. "Analysis of bounded variation penalty methods for ill-posed problems". In: *Inverse Probl.* 10.6 (June 1994), pp. 1217–1229.

[2] T. Adali, P. Schreier, and L. Scharf. "Complex-valued signal processing: The proper way to deal with Impropriety". In: *IEEE Transactions on Signal Processing* 59.1 (2011), pp. 5101–5125.

[3] L. G. Alexopoulos, G. R. Erickson, and F. Guilak. "A method for quantifying cell size from differential interference contrast images: validation and application to osmotically stressed chondrocytes". In: *Journal of Microscopy* 205.2 (Feb. 2002), 125–135.

[4] R. D. Allen, G. B. David, and G. Nomarski. "The Zeiss-Nomarski differential interference equipment for transmitted-light microscopy". In: *Zeitschrift Fur Wissenschaftliche Mikroskopie Und Mikroskopische Technik* 69.4 (1969), pp. 193–221.

[5] H. Attouch, J. Bolte, and B. F. Svaiter. "Convergence of descent methods for semi-algebraic and tame problems: proximal algorithms, forward-backward splitting, and regularized Gauss-Seidel methods". In: *Math. Program.* 137.1–2 (Feb. 2013), pp. 91–129.

[6] M. N. Avadhanulu and P. G. Kshirsagar. *A Textbook of Engineering Physics*. India: S. Chand and Company PVT. LTD., 2008, pp. 94–236.

[7] D. H. Ballard and C. M. Brown. *Computer Vision*. Prentice Hall, 1982.

[8] J. Barzilai and J. M. Borwein. "Two-Point Step Size Gradient Methods". In: *IMA J. Numer. Anal.* 8.1 (Jan. 1988), pp. 141–148.

[9] L. Bautista, S. Rebegoldi, L. Blanc-Féraud, M. Prato, L. Zanni, and A. Plata. "Phase estimation in differential-interference-contrast (DIC) microscopy". In: *2016 IEEE 13th International Symposium on Biomedical Imaging (ISBI)*. 2016, pp. 136–139.

[10] A. Beck and M. Teboulle. "A fast iterative shrinkage-thresholding algorithm for linear inverse problems". In: *SIAM J. Imaging Sci.* 2.1 (2009), pp. 183–202.

[11] M. Bertero, P. Boccacci, G. Talenti, R. Zanella, and L. Zanni. "A discrepancy principle for Poisson data". In: *Inverse Probl.* 26.10, 105004 (Oct. 2010).

[12] M. C. Bertilson, O. von Hofsten, M. Lindblom, T. Wilhein, H. M. Hertz, and U. Vogt. "Compact high-resolution differential interference contrast soft x-ray microscopy". In: *Applied Physics Letters* 92.064104 (2008), pp. 064104–1–064104–3.

[13] S. Bonettini, A. Chiuso, and M. Prato. "A scaled gradient projection method for Bayesian learning in dynamical systems". In: *SIAM J. Sci. Comput.* 37.3 (2015), A1297–A1318.

[14] S. Bonettini, R. Zanella, and L. Zanni. "A scaled gradient projection method for constrained image deblurring". In: *Inverse Probl.* 25.1, 015002 (Jan. 2009).

[15] S. Bonettini, I. Loris, F. Porta, M. Prato, and S. Rebegoldi. “On the convergence of variable metric line–search based proximal-gradient method under the Kurdyka– Lojasiewicz inequality”. In: (submitted).

[16] S. Bonettini, G. Landi, E. Loli Piccolomini, and L. Zanni. “Scaling techniques for gradient projection-type methods in astronomical image deblurring”. In: *Int. J. Comput. Math.* 90.1 (Jan. 2013), pp. 9–29.

[17] S. Bonettini, I. Loris, F. Porta, and M. Prato. “Variable metric inexact line–search based methods for nonsmooth optimization”. In: *SIAM J. Optim.* 26.2 (2016), pp. 891–921.

[18] M. J. Booth. “Adaptive optical microscopy, the ongoing quest for a perfect image”. In: *Light, Science and Applications* 3 (2014), pp. 1–7.

[19] E. Bostan, E. Froustey, B. Rappaz, E. Shaffer, D. Sage, and M. Unser. “Phase retrieval by using transport-of-intensity equation and differential interference contrast microscopy”. In: *Proc. 21th IEEE International Conference on Image Processing*. 2014, pp. 3939–3943.

[20] D. Brandon and W. Kaplan. *Microstructural Characterization of Materials*. England: John Wiley and Sons, Ltd., 2008.

[21] E. Candès, X. Li, and M. Soltanolkotabi. “Phase Retrieval via Wirtinger Flow: Theory and Algorithms”. In: *IEEE Transactions on Information Theory* 61.4 (2015), pp. 1985–2008.

[22] E. Candès and B. Recht. “Exact Matrix Completion via Convex Optimization”. In: *Foundations of Computational Mathematics* 9 (2009), pp. 717–772.

[23] E. Candès, T. Strohmer, and V. Voroniski. “PhaseLift: Exact and Stable Signal Recovery from Magnitude Measurements via Convex Programming”. In: *Communications on Pure and Applied Mathematics* 66.8 (2012), 1241—1274.

[24] M. Carlsson. “On convexification/optimization of functionals including an l2-misfit term”. In: *Submitted to Elsevier* (2016).

[25] P. Charbonnier, L. Blanc-Féraud, G. Aubert, and M. Barlaud. “Deterministic edge-preserving regularization in computed imaging”. In: *IEEE Trans. Image Process.* 6.2 (Feb. 1997), pp. 298–311.

[26] X. Chen, B. Zheng, and H. Liu. “Optical and digital microscopic imaging techniques and applications in pathology”. In: *Analytical Cellular Pathology* 34 (2011), pp. 5–18.

[27] S. H. Cody, S. D. Xiang, M. J. Layton, E. Handman, M. H. C. Lam, J. E. Layton, E. C. Nice, and J. K. Heath. “A simple method allowing DIC imaging in conjunction with confocal microscopy”. In: *Journal of Microscopy* 217.3 (2005), pp. 265–274.

[28] C.J. Cogswell, N.I. Smith, K.G. Larkin, and P. Hariharan. “Quantitative DIC microscopy using a geometric phase shifter”. In: *Proc. SPIE 2984, Three-Dimensional Microscopy: Image Acquisition and Processing IV*. 1997, pp. 72–81.

[29] E. J. Cogswell and E. J. R. Sheppard. “Confocal differential interference contrast (DIC) microscopy: including a theoretical analysis of conventional and confocal DIC imaging”. In: *Journal of Microscopy* 165.1 (1992), pp. 81–101.

[30] A. Cornelio, F. Porta, and M. Prato. "A convergent least-squares regularized blind deconvolution approach". In: *Appl. Math. Comput.* 259.12 (May 2015), pp. 173–186.

[31] K. Creath. "Phase-measurement Interferometry Techniques". In: *Progress in Optics* 26 (1988), pp. 349–393.

[32] Y. H. Dai and Y. X. Yuan. "Alternate minimization gradient method". In: *IMA J. Numer. Anal.* 23.3 (July 2003), pp. 377–393.

[33] R. De Asmundis, D. di Serafino, F. Riccio, and G. Toraldo. "On spectral properties of steepest descent methods". In: *IMA J. Numer. Anal.* 33.4 (Oct. 2013), pp. 1416–1435.

[34] T. Evgeniou, M. Pontil, and T. Poggio. "Phase retrieval algorithms: a comparison". In: *Applied Optics* 21.15 (Apr. 1982), pp. 2758–2769.

[35] R. Fletcher. "A limited memory steepest descent method". In: *Math. Program.* 135.1–2 (Oct. 2012), pp. 413–436.

[36] R. Fletcher. *Practical methods of optimization*. 2nd. New York: John Wiley and Sons, 2000.

[37] P. Frankel, G. Garrigos, and J. Peypouquet. "Splitting methods with variable metric for Kurdyka–Łojasiewicz functions and general convergence rates". In: *J. Optim. Theory Appl.* 165.3 (June 2015), pp. 874–900.

[38] M. M. Frigault, J. Lacoste, J. L. Swift, and C. M. Brown. "Livecell microscopy, tips and tools". In: *Journal of Cell Science* 122 (2009), pp. 753–767.

[39] W. Galbraith and G. B. David. "An aid to understanding differential interference contrast microscopy : computer simulation". In: *Journal of Microscopy* 108.2 (Mar. 1976), pp. 147–176.

[40] R. W. Gerchberg and W. O. Saxton. "A practical algorithm for the determination of phase from image and diffraction plane pictures". In: *Optik* 35.2 (Mar. 1972), pp. 237–246.

[41] J. C. Gilbert and J. Nocedal. "Global convergence properties of conjugate gradient methods for optimization". In: *SIAM J. Optim.* 2.1 (1992), pp. 21–42.

[42] D. Goldstein. *Polarized Light*. 3rd. Newark: CRC Press, 2011.

[43] J. W. Goodman. *Statistical Optics*. New York: Wiley, 1984.

[44] T. J. Holmes. "Signal-processing characteristics of differential-interference-contrast microscopy. 2: Noise considerations". In: *Applied Optics* 27.7 (1988), pp. 1302–1308.

[45] T. J. Holmes and W. J. Levy. "Signal-processing characteristics of differential-interference-contrast microscopy". In: *Applied Optics* 26.18 (Sept. 1987), pp. 3929–3939.

[46] A. B. Johnson and L. J. Lewis. *Molecular Biology of the Cell*. 4th. New York: Garland Science, 2002. URL: `http://www.ncbi.nlm.nih.gov/books/NBK26880/`.

[47] F. Kagalwala and T. Kanade. "Computational Model of Image Formation Process in DIC Microscopy". In: vol. 3261. 1998, pp. 193–207.

[48] Z. Kam. "Microscopic differential interference contrast image processing by line integration (LID) and deconvolution". In: *Bioimaging* 6.4 (1998), pp. 166–176.

[49] H. Kamiokaa, T. Honjoa, and T. Takano-Yamamoto. “A three-dimensional distribution of osteocyte processes revealed by the combination of confocal laser scanning microscopy and differential interference contrast microscopy”. In: *Bone* 28.2 (Feb. 2001), pp. 145–149.

[50] C.W. Keevil. “Rapid detection of biofilms and adherent pathogens using scanning confocal laser microscopy and episcopic differential interference contrast microscopy”. In: *Water, Science and Technology* 47.5 (2003), pp. 105–116.

[51] C.T. Kelley. *Iterative Methods for Optimization.* Philadelphia: SIAM, 1999, pp. 43–44.

[52] S. S. Kou, L. Waller, G. Barbastathis, and C. J. R. Sheppard. “Transport-of-Intensity approach to differential interference contrast (TI-DIC) microscopy for quantitative phase imaging”. In: *Optics Letters* 35.3 (2010), pp. 447–449.

[53] S. Krantz and H. R. Parks. *A primer of Real Analytic Functions.* Birkhäuser, 2002.

[54] K. Kurdyka. “On gradients of functions definable in o-minimal structures”. In: *Ann. Inst. Fourier* 48.3 (1998), pp. 769–783.

[55] W. Lang. “Nomarski differential interference contrast microscopy II. Formation of the interference image”. In: *Zeiss Inf.* 17 (1969), pp. 12–16.

[56] H. Lantéri, M. Roche, and C. Aime. “Penalized maximum likelihood image restoration with positivity constraints: multiplicative algorithms”. In: *Inverse Probl.* 18.5 (Oct. 2002), pp. 1397–1419.

[57] S. Łojasiewicz. “Une propriété topologique des sous-ensembles analytiques réels”. In: *Les Équations aux Dérivées Partielles.* Paris: Éditions du Centre National de la Recherche Scientifique, 1963, pp. 87–89.

[58] C . J. R. Sheppard N. I. Smith M. R. Arnison K. G. Larkin and C . J. Cogswell. “Linear phase imaging using differential interference contrast microscopy”. In: *Journal of Microscopy* 214.1 (2004), pp. 7–12.

[59] N.I. Smith P.W. Fekete M. R. Arnison C.J. Cogswell and K.G. Larkin. “Using the Hilbert transform for 3D visualization ofdifferential interference contrast microscope images”. In: *Journal of Microscopy* 199.1 (2000), pp. 79–84.

[60] D. Malacara. “Phase shifting interferometry”. In: *Revista Mexicana de Física* 1.36 (1990), pp. 6–22.

[61] S. B. Mehta and R. Oldenbourg. “Image simulation for biological microscopy: microlith”. In: *Biomedial Optics Express* 5.6 (2014), pp. 1822–1838.

[62] S. B. Mehta and C. J. R. Sheppard. “Partially coherent image formation in differential interference contrast (DIC) microscope”. In: *Optics Express* 16.24 (Nov. 2008), pp. 19462–19479.

[63] S. B. Mehta and C. J. R. Sheppard. “Sample-less calibration of the differential interference contrast microscope”. In: *Applied Optics* 49.15 (May 2010), pp. 2954–2968.

[64] E. B. van Munster, L. J. van Vliet, and J. A. Aten. “Reconstruction of optical pathlength distributions from images obtained by a wide-field differential interference contrast microscope”. In: *Journal of Microscopy* 188.2 (1997), pp. 149–157.

[65] D. B. Murphy. *Fundamentals of Light Microscopy and Electronic Imaging*. New York: Wiley-Liss, 2001.

[66] J. Nocedal and S. J. Wright. *Numerical optimization*. 2nd. New York: Springer, 2006.

[67] T. Ono, R. Okamoto, and S. Takeuchi. "An entanglement-enhanced microscope". In: *Nature Communications* 4 (2013), pp. 1–7.

[68] *Optical axis*. URL: `https://en.wikipedia.org/wiki/Optical_axis`.

[69] F. J. Pedrotti and L. S. Pedrotti. *Introduction to Optics*. Prentice Hall, 1992.

[70] L. S. Pedrotti. "Basic Physical Optics". In: *Fundamentals of Photonics*. Ed. by Ch. Roychoudhuri. SPIE, 2008, pp. 117–167.

[71] M. Prato, R. Cavicchioli, L. Zanni, P. Boccacci, and M. Bertero. "Efficient deconvolution methods for astronomical imaging: algorithms and IDL-GPU codes". In: *Astron. Astrophys.* 539 (Mar. 2012), A133.

[72] C. Preza. "Rotational-diversity phase estimation from differential interference contrast microscopy images". In: *J. Opt. Soc. Am. A* 17.3 (2000), pp. 415–424.

[73] C. Preza, S. V. King, and C. J. Cogswell. "Algorithms for extracting true phase from rotationally-diverse and phase-shifted DIC images". In: *Three-Dimensional and Multidimensional Microscopy: Image Acquisition and Processing XIII*. Ed. by J.-A. Conchello, C. J. Cogswell, and T. Wilson. Vol. 6090. Proc. SPIE. 2006.

[74] C. Preza, D. L. Snyder, and J.-A. Conchello. "Image reconstruction for three-dimensional transmitted-light DIC microscopy". In: *Three-Dimensional Microscopy: Image Acquisition and Processing IV*. Ed. by J.-A. Conchello, C. J. Cogswell, and T. Wilson. Vol. 2984. Proc. SPIE. 1997.

[75] C. Preza, D. L. Snyder, and J.-A. Conchello. "Theoretical development and experimental evaluation of imaging models for differential interference contrast microscopy". In: *J. Opt. Soc. Am. A* 16.9 (1999), pp. 2185–2199.

[76] L. I. Rudin, S. Osher, and E. Fatemi. "Nonlinear total variation based noise removal algorithms". In: *J. Phys. D.* 60.1–4 (1992), pp. 259–268.

[77] U. Schnars, C. Falldorf, J. Watson, and W. Jüptner. *Digital Holography and Wavefront Sensing: Principles, Techniques and Applications*. Germany: Springer, 2015.

[78] Y. Shechtman, Y. C. Eldar, O. Cohen, H. N. Chapman, J. Miao, and M. Segev. "Phase Retrieval with Application to Optical Imaging". In: *IEEE Signal Processing Magazine* 32.3 (2015), pp. 87–109.

[79] M. Shribak and S. Inoué. "Orientation-independent differential interference contrast microscopy". In: *Applied Optics* 45.3 (2006), pp. 460–469.

[80] S. P. Singh and B. S. Tomar. *Cell Biology*. India: Rastogi Publications, 2007.

[81] W. Sun, N. Fang, and B. G. Trewyn et al. "Endocytosis of a single mesoporous silica nanoparticle into a human lung cancer cell observed by differential interference contrast microscopy". In: *Anal Bioanal Chem* 391 (2008), p. 2119.

[82] G. Wang, W. Sun, Y. Luo, and N. Fang. “Resolving Rotational Motions of Nano-objects in Engineered Environments and Live Cells with Gold Nanorods and Differential Interference Contrast Microscopy”. In: *J. Am. Chem. Soc.* 132.46 (Nov. 2010), 16417–16422.

[83] L. Wang and H. Wu. *Biomedical Optics: Principles and Imaging*. Hoboken, New Jersey: John Wiley and Sons, Inc, 2007.

[84] R. Wayne. *Light and Video Microscopy*. San Diego, USA: Academic Press, 2014.

[85] S. M. Wilson and A. Bacic. “Preparation of plant cells for transmission electron microscopy to optimize immunogold labeling of carbohydrate and protein epitopes”. In: *Nature Protocols* 7 (2012), 1716—1727.

[86] Y. Xu and W. Yin. “A block coordinate descent method for regularized multiconvex optimization with applications to nonnegative tensor factorization and completion”. In: *SIAM J. Imaging Sci.* 6.3 (2013), pp. 1758–1789.

[87] B. Zhou, L. Gao, and Y. H. Dai. “Gradient Methods with Adaptive Step-Sizes”. In: *Comput. Optim. Appl.* 35.1 (Sept. 2006), pp. 69–86.

Phase Estimation for Differential Interference Microscopy

Abstract: In this dissertation we address the problem of estimating the phase from color images acquired with differential–interference–contrast (DIC) microscopy. This technique has been widely recognized for producing high contrast images at high lateral resolution. One of its disadvantages is that the observed images cannot be easily used for topographical and morphological interpretation, because the changes in phase of the light, produced by variations in the refractive index of the object, are hidden in the intensity image. We present an image formation model for polychromatic light, along with a detailed description of the point spread function (PSF). As for the phase recovery problem, we followed the inverse problem approach by means of minimizing a non-linear least–squares (LS)–like discrepancy term with an edge–preserving regularizing term, given by either the hypersurface (HS) potential or the total variation (TV) one. We investigate the analytical properties of the resulting objective non-convex functions, prove the existence of minimizers and propose a compact formulation of the gradient allowing fast computations. Then we use recent effective optimization tools able to obtain in both the smooth and the non-smooth cases accurate reconstructions with a reduced computational demand. We performed different numerical tests on synthetic realistic images and we compared the proposed methods with both the original conjugate gradient method proposed in the literature, exploiting a gradient–free linesearch for the computation of the steplength parameter, and other standard conjugate gradient approaches. The results we obtained in this approach show that the performances of the limited memory gradient method used for minimizing the LS+HS functional are much better than those of the CG approaches in terms of number of function/gradient evaluations and, therefore, computational time. Then we also consider another formulation of the phase retrieval problem by means of minimization with respect to a complex variable under constraint of modulus one. However, standard projected gradient descent algorithms appear to be inefficient and sensitive to initialization. We conclude by proposing in this case a reformulation by optimization on low-rank matrices.

Keywords: DIC microscopy, phase estimation, nonlinear optimization methods